HOAN BRIDGE FORENSIC INVESTIGATION
FAILURE ANALYSIS FINAL REPORT

By

John W. Fisher
Eric J. Kaufmann

ATLSS Center
Lehigh University

William Wright
Zuhan Xi
Hernando Tjiang

Turner-Fairbank
FHWA

Bala Sivakumar
William Edberg

Lichtenstein Cons.
Engineers

For

Wisconsin Department of Transportation
and the
Federal Highway Administration

June 2001

TABLE OF CONTENTS

1. Introduction

2. Material Property Test Results
   2.1 Properties of Web Plates
      2.1.1 Chemical Composition
      2.1.2 Strength of Web Plates
      2.1.3 Charpy Vee Notch Tests (CVN)
      2.1.4 Fracture Toughness of Web Plates
      2.1.5 Summary – Properties of Web Plates
   2.2 Properties of Bottom Flange Plates
      2.2.1 Chemical Composition of Bottom Flange Plates
      2.2.2 Strength of Bottom Flange Plates
      2.2.3 Charpy Vee Notch Tests of Bottom Flange Plates
      2.2.4 Fracture Toughness of Bottom Flange Plates
      2.2.5 Summary – Properties of Bottom Flange Plates

3. Structural Models and Field Measurements
   3.1 Global Structural Analysis
      3.1.1 Load Cases
      3.1.2 Results
      3.1.3 Dead Load
      3.1.4 Live Load: AASHTO HS20-44 Lane Loading
      3.1.5 Live Load: 4-Axle Truck
      3.1.6 Wind Load
      3.1.7 Uniform Temperature Change
      3.1.8 Temperature Gradient
      3.1.9 Bracing Removal
      3.1.10 Summary-Global Structural Analysis
   3.2 Finite Element Model of Joint E-28
      3.2.1 Model Description
      3.2.2 Applied Load
      3.2.3 Stress Concentration Due to Shelf Plate Detail
      3.2.4 Effect of Fabrication Tolerance
      3.2.5 Effect of Shelf Plate Hole
      3.2.6 Effect of Lateral Bracing Forces
      3.2.7 Calculation of Triaxiality
      3.2.8 Summary – Local Stress Analysis
   3.3 Load Testing
      3.3.1 Strain Gage Details
      3.3.2 Test Truck Load Cases
      3.3.3 Gage Results
   3.4 Weigh-In-Motion
      3.4.1 Summary of WIM Study Findings

4. Fractographic and Metallographic Examination
   4.1 Fracture Samples
   4.2 Fractographic Examination
      4.2.1 Girder E P.P. 28 – Fracture Origin
      4.2.2 Girder D P.P. 28 – Fracture Origin
      4.2.3 Girder F P.P. 28 – Fracture Origin
      4.2.4 Girder D P.P. 9 and Girder B P.P. 26 – Fracture Origin
      4.2.5 Girder D P.P. 28 – Bottom Flange Crack Arrest
      4.2.6 Girder E P.P. 28 – Bottom Flange Fracture
      4.2.7 Girder E P.P. 28 - Web Fracture Bifurcation
      4.2.8 Girder E P.P. 28 – Shelf Plate Fracture at Hole Repair
      4.2.9 Girder E P.P. 28 – Transverse Brace Fracture
   4.3 Summary - Fractographic and Metallographic Examination

5. Fracture Analysis
   5.1 Prediction of Web Crack Initiation
   5.2 Crack Arrest at Bottom Flange
   5.3 Summary – Fracture Analysis

6. Summary and Conclusions

7. References

LIST OF TABLES

Table 2.1 Composition of Web Material at Fracture Locations

Table 2.2 Statistical Variability of Web Plate Chemistry at 18 Different Locations

Table 2.3 Average Tension Test Results for Web Plates at Fracture Location

Table 2.4 Statistical Composition of 18 Tension Test Samples from Cores (Rate: ASTME-8)

Table 2.5 Estimated Fracture Toughness of Web Plates at Bridge Loading Rates

Table 2.6 Composition of Bottom Flange Material at Fracture Locations

Table 2.7 Average Tension Tests of Flange Plates at Room Temperature

Table 2.8 Compact Tension Test C(T) Matrix for Flange Plates

Table 2.9 Toughness Results from C(T) Tests

Table 2.10 Estimated Fracture Toughness of Bottom Flange Plates at Bridge Loading Rates

Table 2.11 Estimated Fracture Toughness of Bottom Flange Plates at Dynamic Loading Rates

Table 3.1 Calculated Dead Load Forces and Stress

Table 3.2 Load Case 7 Lane Loading in All Three Lanes

Table 3.3 Comparison of Measured and Calculated Stresses

Table 3.4 Estimated Live Load Forces at Failure

Table 3.5 Calculated Forces and Stress Due to Temperature Change

Table 3.6 Calculated Forces and Stress Due to Temperature Gradient

Table 3.7 Effect of Bracing Removal on Flange Stress

Table 3.8 Effect of Fabrication Tolerance on Principal Stress in the Web Gap

Table 3.9 Effect of 2 in. Shelf Plate Hole on Principal Stress in the Web Gap

Table 3.10 Change in Elastic Stress State Due to Forces in the Lateral Bracing

Table 3.11 Maximum Truck Load Stresses from All Passes and Lanes

Table 3.12 Summary of Maximum Measured Stresses

Table 3.13 Strip Gage Strains (Stresses)

Table 3.14 Truck Traffic for Different Time Periods

LIST OF FIGURES

Figure 1: South Approach Unit S2A Showing Location of Fractured Span

Figure 2: Typical Cross-Section

Figure 3: Framing Plan and Elevation of Fractured Span

Figure 4: Visible Fractures of Center Girder E-28 and East Girder F-28

Figure 5: Cracked Web of Girder D-28

Figure 6: Typical Stress-Strain Curve for the Girder E Web (A36 Steel)

Figure 7: CVN Transition Curve for the Web Plate at D-28

Figure 8: CVN Transition Curve for the Web Plate at E-28

Figure 9: CVN Transition Curve for the Web Plate at F-28

Figure 10: Histograms of CVN Tests From All Web Locations @ +10E F and +40E F

Figure 11: K_{IC} Transition Curves for the Web Plate at D-28 Based on CVN Tests

Figure 12: K_{IC} Transition Curves for the Web Plate at E-28 Based on CVN Tests

Figure 13: K_{IC} Transition Curves for the Web Plate at F-28 Based on CVN Tests

Figure 14: Typical Stress-Strain Curves for the 2-1/4 in. Flange Plate at F-28 (A588 Steel)

Figure 15: CVN Transition Curve for the Bottom Flange Plate at D-28

Figure 16: CVN Transition Curve for the Bottom Flange at E-28

Figure 17: CVN Transition Curve for the Bottom Flange at F-28

Figure 18: C(T) Test Data for the Bottom Flange at D-28

Figure 19: C(T) Test Data for the Bottom Flange at E-28

Figure 20: K_{IC} Transition Curves for the Bottom Flange Plate at D-28

Figure 21: K_{IC} Transition Curves for the Bottom Flange Plate at E-28

Figure 22: K_{IC} Transition Curves for the Bottom Flange Plate at F-28

Figure 23: Typical Cross-Section of Global Model

Figure 24: Test Truck and WIM Loading

Figure 25: Web Element at E-28 (shown with 4 axle truck loading)

Figure 26: Bracing Members and Bottom Flange Members at Panel Point 28 (girder not shown)

Figure 27: Cross-Section View of Load Case 7

Figure 28: Plan View of Lane Loading for Load Case 7

Figure 29: Transverse Position of Loads for Two 4 Axle Vehicles to Maximize Center Girder Web Stress

Figure 30: Longitudinal Position of Loads for 4 Axle Vehicles

Figure 31: Wind Load Forces in Bracing Members and Girder Bottom Flanges Before Failure

Figure 32: Temperature Gradient Deflections in Unit S2A

Figure 33: Deflected Shape of the Cross-Section at Panel Point 28

Figure 34: 3-D Solid Finite Element Model with Hole in Shelf Plate

Figure 35: Section Through the Finite Element Model Showing the Mesh Density

Figure 36: Total Load (DL + LL) Applied for Stress Analysis

Figure 37: Variation in Bending Stress (σ_x) in the Web Along the Length of the Shelf Plate

Figure 38: Variation in Principal Stress Through the Web Thickness with a Centered Shelf Plate

Figure 39: Variation in Principal Stress Through the Web Thickness with the Offset Shelf Plate

Figure 40: Variation in Principal Stress Through the Web Thickness with a 2 in. Hole in the West Shelf Plate

Figure 41: Change in Elastic Bending Stress in the Web Due to Lateral Bracing Forces

Figure 42: Strain Gage Plan for Panel Point 28

Figure 43: Photo's of Strain Gage Installation

Figure 44: Typical Truck Traffic

Figure 45: Gross Vehicle Weight Distribution for All Trucks

Figure 46: Gross Vehicle Weight Distribution, 6 Axle Trucks

Figure 47: Axle Weight Distribution and Frequency Histogram, All Trucks

Figure 48: Shelf Plate with Web Fracture Origin at the Weld Termination (Girder E, P.P. 28)

Figure 49: Opposing Web Crack Surface at Fracture Origin Attached to the Vertical Connection Plate (Girder E. P.P. 28)

Figure 50: Opposing Crack Surfaces Showing the Web Fractures (Girder E, P.P. 28)

Figure 51: SEM Micrographs Obtained From Opposing Sides of Fracture Showing Cleavage at the Fracture Origin (Girder E, P.P. 28)

Figure 52: Section of Girder D, P.P. 28 Containing the Crack Origin Area and Arrested Crack in the Bottom Flange

Figure 53: Opposing Crack Surfaces at the Shelf Plate Weld Termination Fracture Origin

Figure 54: SEM Micrographs of the Fracture Origin Areas Showing Cleavage Fracture (Girder D, P.P. 28)

Figure 55: Section of Girder F, P.P. 28 Containing the Shelf Plate Weld Fracture Origin

Figure 56: SEM Micrographs of the fracture Origin Area Showing Cleavage Fracture (Girder F, P.P. 28)

Figure 57: Web Crack Removed from Girder D at P.P. 9 at the Shelf Plate Connection

Figure 58: Fracture Origin in the Web Showing Cleavage Fracture (Girder D, P.P. 9)

Figure 59: Web Crack Removed from Girder B at P.P. 26 at the Shelf Plate Connection

Figure 60: Fracture Origin Showing Blackened Thumbnail and Cleavage Initiation Areas (Girder B, P.P. 26)

Figure 61: SEM Micrographs Showing the Oxide Layer Covering the Thumbnail Defect and Cleavage and Mixed Mode Fracture Near the Fracture Origin (Girder B, P.P. 26)

Figure 62: Etched Cross-Section Through Thumbnail Defect at Fracture Origin (Girder B, P. P. 26)

Figure 63: Exposed Fracture Surface from Girder D, P.P. 28 Showing Crack Arrest in the Bottom Flange. Note the weld fusion line location

Figure 64: SEM Micrographs of the Crack Arrest Boundary Showing Cleavage and Ductile Fracture. Dashed Lines Denote Crack Arrest Boundary (Girder D, P.P. 280)

Figure 65: Cleavage Fracture in the Web-Flange Area of the Bottom Flange of Girder E, P.P. 28

Figure 66: Crack Bifurcation in the Web of Girder E, P.P. 28, Near the Fracture Origin

Figure 67: Etched Cross-Section Through the Web and the Crack Bifurcation Location

Figure 68: Girder E, P.P. 28 Shelf Plate Showing the Hole Repair and Crack Surface Adjacent to the Hole

Figure 69: SEM Micrographs Obtained Near the Shelf Plate Hole Showing Fatigue Striations Near the Hole Edge and Ductile Shear Fracture Beyond (Girder E, P.P. 28)

Figure 70: Transverse Brace Fracture at Girder E, P.P. 28. Cleavage Fracture Initiated in the Radius of the Flame Cut Cope at the Corner. Cleavage was Observed next to the Abraded Crack Surface at the Corner

Figure 71: Geometric Condition Providing a Crack-Like Plane When Shelf Plate is Touching Transverse Connection Plate

Figure 72: Idealized Circular 3D Crack Model at Shelf Plate – Transverse Connection Plate Intersection

Figure 73: Idealized Circular 3D Crack Arrested in Web-Flange Zone

1. INTRODUCTION

The Hoan Bridge (also know as the Milwaukee Harbor Bridge), opened to traffic in 1977, is located on interstate highway I-794 over the Milwaukee River in the city of Milwaukee, Wisconsin. I-794 is a major commuter route carrying 6 lanes of traffic to and from the city. Eighteen of the bridge spans are steel plate girder spans; the main unit is a three span tied arch crossing the river.

On December 13, 2000, cracks were detected in the steel girders supporting one of the southern approach spans. Two of the three girders had full depth fractures, leaving the span near collapse. The entire roadway, both northbound and southbound, was immediately closed to traffic. On December 28, the most critically damaged section of the northbound roadway was removed by explosive demolition. The southbound roadway was re-opened to two way traffic on February 17, 2001, with weight and speed restrictions on bridge traffic.

Lichtenstein Consulting Engineers, in conjunction with the Center for Advanced Technology for Large Structural Systems at Lehigh University and the Turner-Fairbank Research Center of the Federal Highway Administration, performed analytic and forensic tasks associated with the failed and remaining spans of the Hoan Bridge for the Wisconsin Department of Transportation.

Work included the following tasks:

- Task I –identify existing defects in steel members and details of the southbound spans through visual inspection and non-destructive testing methods. Hole drilling was performed at selected locations and other short-term repairs to ensure the safety of the southbound bridge (until long-term fatigue and fracture retrofit measures can be implemented) so that southbound lanes could be opened to traffic at the earliest possible date. The work has been completed and the Southbound bridge was opened to restricted traffic (4 ton weight limit) on February 17, 2001.

- Task II – conduct a failure analysis on the failed unit to ascertain the causes and modes of failure and make recommendations for future action (retrofit or replacement) for all similar spans on the bridge.

Detailed documentation of the fractures that were discovered in the southern approach span shown in Figure 1 is provided in Reference 1 for the conditions that existed prior to demolition of the structure.

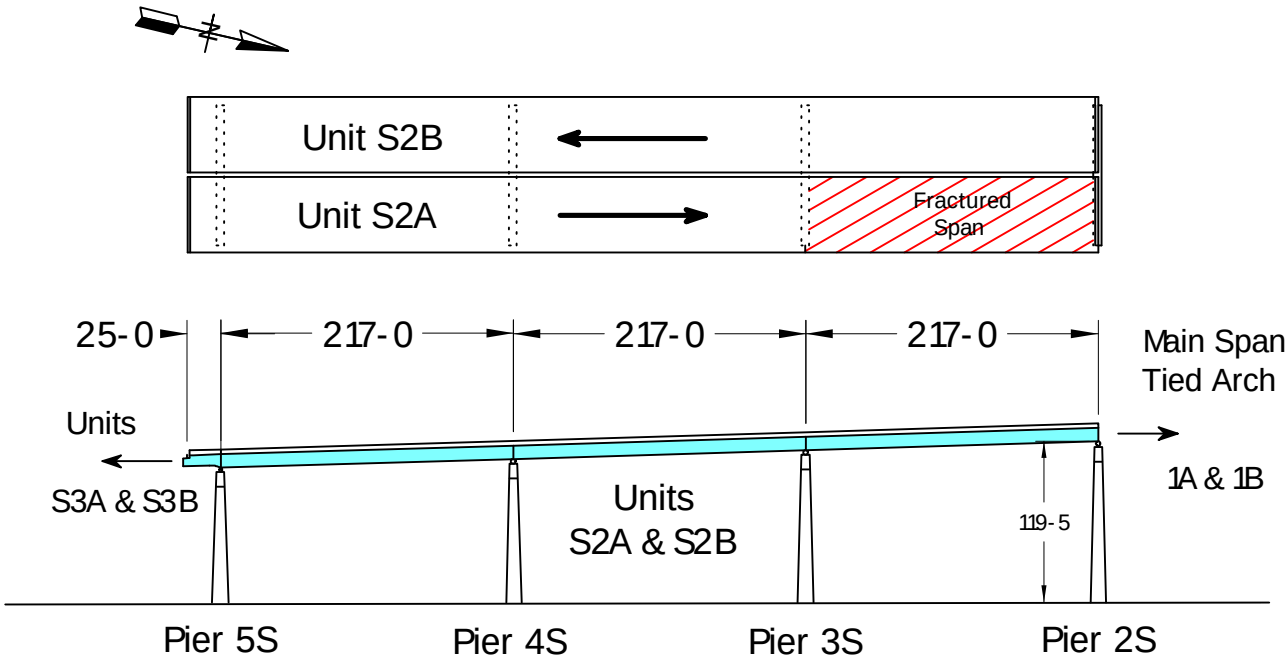

Figure 1: South Approach Unit 52A Showing Location of Fractured Span

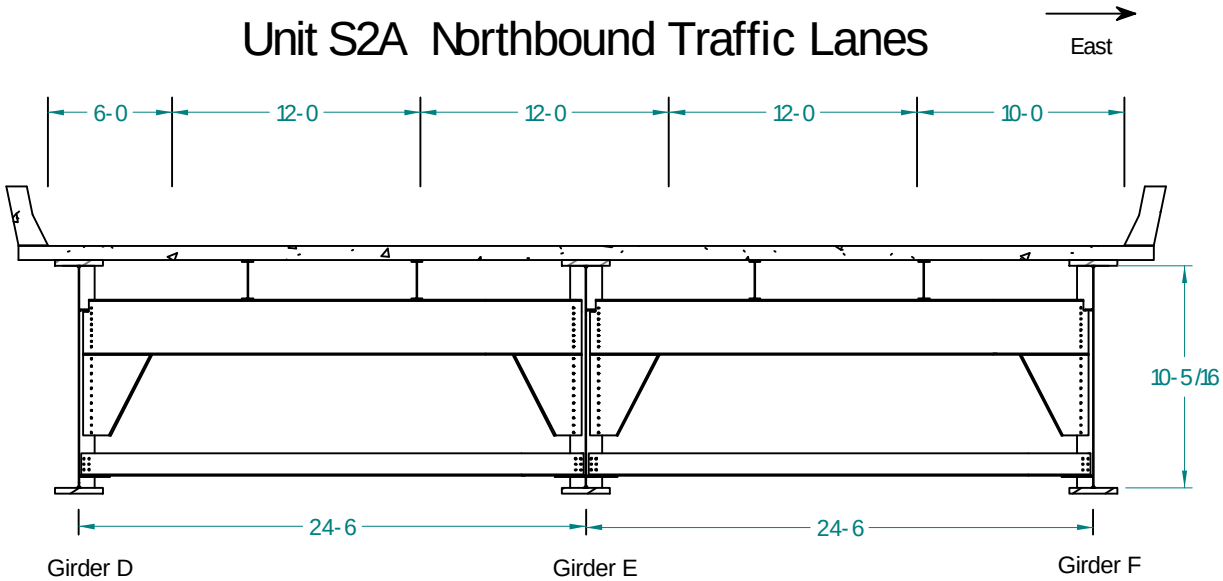

Figure 2: Typical Cross-Section

The cross-section of the three-girder structure is shown in Figure 2. The framing plan and the elevations for the northern end span of Unit S2A is given in Figure 3 which also identifies the cracked girder locations at Panel Point 28.

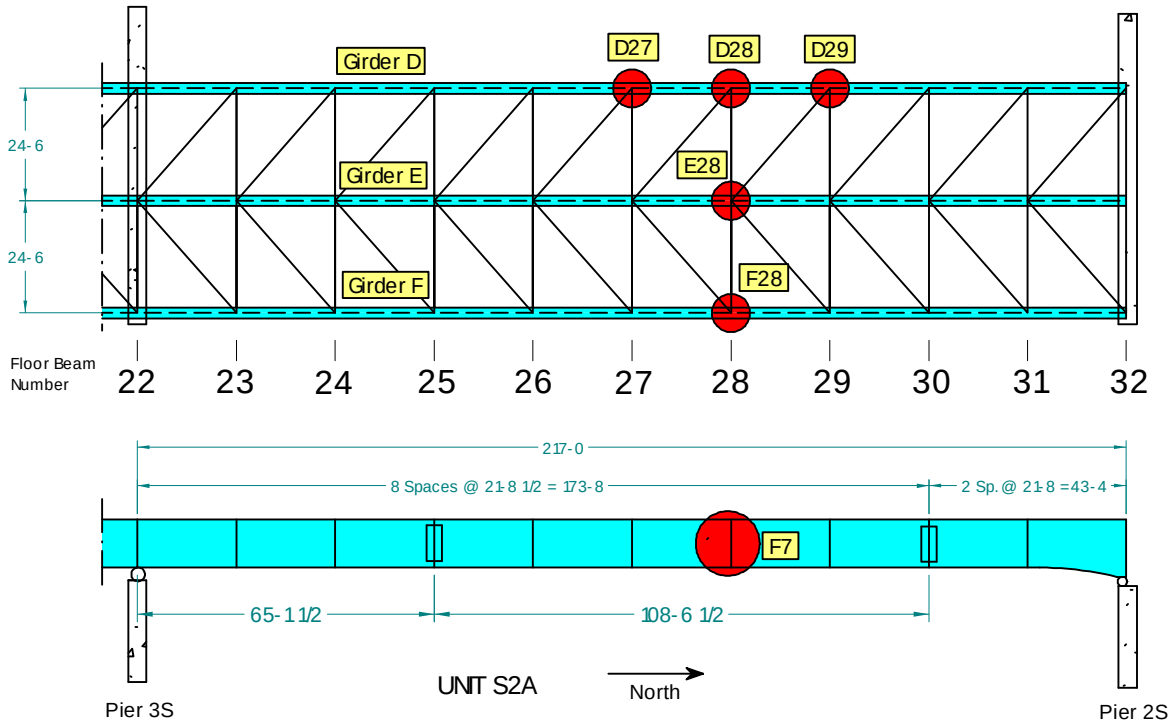

Figure 3 Framing Plan and Elevation of Fractured Span

Figure 4 shows the fractures that developed in Center Girder E and outside Girder F prior to the demolition.

Figure 4: Visible Fractures of Center Girder E-28 and East Girder F-28

The west exterior girder D did not experience a flange fracture although a 3 ft. web crack had formed in the girder web, as illustrated in Figure 5.

Figure 5: Cracked Web of Girder D-28

This report summarizes the results of the failure analysis and forensic investigation that was carried out on the three cracked girders from the Hoan Bridge. Valuable insight was also provided by examining cracked surfaces from two other cracked girder webs in the Hoan Bridge Structure. One was from northbound Unit S2A at Panel Point 9 of Girder D. The second was removed from southbound unit S2B at Panel Point 26 of Girder B. These latter crack surfaces were removed during the inspection and retrofit of southbound unit S2B and northbound unit S2A.

The Hoan Bridge failure section laboratory test samples were all initially removed from the wreckage and shipped to the FHWA Turner-Fairbank Highway Research Center (TFHRC) in McLean, Virginia. W. Wright supervised the removal of segments of the crack surfaces at the shelf plate region and the girder flanges of Girders D, E and F at Panel Point 28. These components were delivered to the ATLSS Laboratories of Lehigh University. Detailed fractographic and metallographic examinations were carried out in the ATLSS Laboratories and are discussed in Section 4.

Boundary forces for this model were provided from a global 3D analysis of Hoan Bridge Unit S2A by Lichtenstein Consulting Engineers. Details are provided in Section 3.1 of this report.

In order to confirm the global model and verify the structural behavior, a diagnostic load test was carried out by Northwestern University and evaluated by Lichtenstein Engineers. The measurement program was carried out on Unit N2A which was similar to Unit S2A. The instrument was installed at Panel Point 5 which was comparable to Panel Point 28. Details are provided in Section 3.3.

At TFHRC the web and flange materials from all three fractured girders were evaluated by extensive testing to determine their mechanical properties of strength and toughness and their chemical composition. A summary is provided in Section 2 and greater detail is given in Ref. 2.

Under the supervision of W. A. Wright, a detailed 3D analytical finite element model was also developed for the local failure region of Interior Girder E at Panel Point 28. This included the web, flange, shelf plates and transverse connection plates. A summary is provided in Section 3.2 and greater detail in Ref. 3.

A weight-in-motion study of trucks (primarily loaded trucks which moved salt from the salt yards) was carried out on the East Lincoln Avenue Viaduct in February 2001. This study was carried out by the University of Michigan. A summary of their findings is provided in Section 3.4.

2. MATERIAL PROPERTY TEST RESULTS

Material property tests were performed to determine the chemical composition, strength, and toughness of steel in the 3 girder approach spans. Testing of the web and flange plates at the fracture locations were performed at the Turner-Fairbank Highway Research Center (TFHRC) in McLean, VA.[2] The samples were cut from sections of the cracked girders shipped to the laboratory. Additional testing was performed on core samples removed from the web plates at multiple locations during the retrofit operation.[4] Mill report information was obtained from Wisconsin DOT records as reported in a prior FHWA report. [1]

2.1 PROPERTIES OF WEB PLATES

2.l.l Chemical Composition of Web Plates

Table 2.1 lists the chemical composition of the web plates from the fracture locations. All of the results meet the current AASHTO M270 Specifications for Grade 36 steel (ASTM A-36)[5]. The test results are more conservative with respect to the specification limits than the mill report results. The statistical summary of results from the eighteen core samples at various locations is reported in table 2.2. The 95% confidence limit calculated to be 2 standard deviations below the mean for carbon and manganese, and 2 standard deviations above the mean for phosphorous, sulfur, and silicon. Again, all individual samples met the M-270 specification.

Table 2.1 Composition of web material at fracture locations

Location and Source		Element (%) Composition									
		C	Mn	P	S	Si	Cu	Ni	Cr	Mo	V
D - 28	Test	.228	.85	.003	.007	.055	.007	.019	.017	.005	<.002
	Mill	.22	.79	.009	.015	.06	---	---	---	---	---
E - 28	Test	.240	.84	<.002	.008	.053	.007	.018	.016	.005	<.002
	Mill	.22	.79	.009	.015	.06	---	---	---	---	---
F - 28	Test	.214	.85	<.002	.006	.053	.007	.018	.017	.005	<.002
	Mill	.22	.79	.009	.015	.06	---	---	---	---	---
ASTM A-36		.25	---	.04 max	.05 max	.40 max	---	---	---	---	---

It can be noted that the % composition of phosphorous, sulfur, and silicon are all well below the maximum allowable value in the specifications. It can also be noted that the composition is very uniform over a number of plates and sample locations.

Table 2.2 Statistical Variability of Web Plate Chemistry at 18 Different Locations

Element	Mean Composition (%)	Standard Deviation (%)	95% Confidence Limit (%)
Carbon	0.226	0.012	0.202 (min)
Manganese	0.808	0.060	0.688 (min)
Phosphorous	0.010	0.005	0.020 (max)
Sulfur	0.017	0.005	0.027 (max)
Silicon	0.044	0.008	0.060 (max)

2.1.2 Strength of Web Plates

Table 2.3 summarizes the tension test results for the web plates near the locations where the fractures occurred. The average results from two standard tests are reported for locations E-28 and F-28, but only one test is reported for girder D. Standard 8 in. flat plate specimens were cut from the web plate parallel to the rolling direction and tested at full thickness. The tests were all conducted according to the ASTM E-8 Test Specifications, except the test speed of 12 ksi/min is slightly slower than the lower bound allowed by the standard.

Figure 6 shows a typical stress-strain curve recorded during testing. The upper yield point reported in table 2.3 corresponds to the peak of the rise at the beginning of the yield plateau. This is typically higher than the 0.2% offset yield strength and the magnitude is highly dependent on the test load rate. The elastic modulus is calculated from linear regression on the elastic portion of the stress-strain curve.

Table 2.3 also compares the test results to the values reported on the mill report and the requirements of the A-36 Specification. All tests at the fracture locations easily met the requirements for yield and ultimate strength in the A-36 specification. The 0.2% offset yield strength reported on the mill test certificate uniformly exceeded the test results by about 16%. About 5% of this difference can be attributed to differences in test rate. Mill tests are usually conducted at the high end of the ASTM allowable rate (100 ksi/min), compared to 12 ksi/min for the FHWA tests.

Table 2.3 Average Tension Test Results for Web Plates at the Fracture Location

Plate	Source	F_y 0.2% offset (ksi)	F_y Upper Yield (ksi)	F_u (ksi)	E (ksi)	% Elong. (8")
E-28 web	2 Tests	39.34	40.94	66.08	29,091	24.4
	Mill	47.7	---	67.0	---	27
F-28 web	2 Tests	38.57	39.60	65.44	29,184	27.7
	Mill	45.8	---	71.4	---	30
D-28 web	1 Test	39.34	41.10	67.16	26,574	26
	Mill	45.8	---	71.4	---	30
ASTM A-36		36 (min)	---	58 to 80	---	20 (min)

Eighteen additional tension tests were performed by another laboratory on the core samples from different locations to assess variability of the plates from other sections of the approach spans.[(4)] One tension test was performed on each of the cores that were removed from various locations in the structure during the retrofit procedure. The tests were performed on round specimens with a 2 in. gage length and reduced diameter. Table 2.4 shows the statistical results from all of the eighteen core tests.

The yield and tensile strength values from the core tests run slightly higher than the FHWA tests, but again, this can be attributed to differences in test rate. Note that the percent elongation cannot be directly compared between the FHWA tests and the core tests because different gage length specimens are used. All individual tests exceeded the A-36 specifications for strength and elongation. Statistically, there is at least a 95% confidence that all web plate in areas tested will exceed the specification requirements for strength and ductility.

.

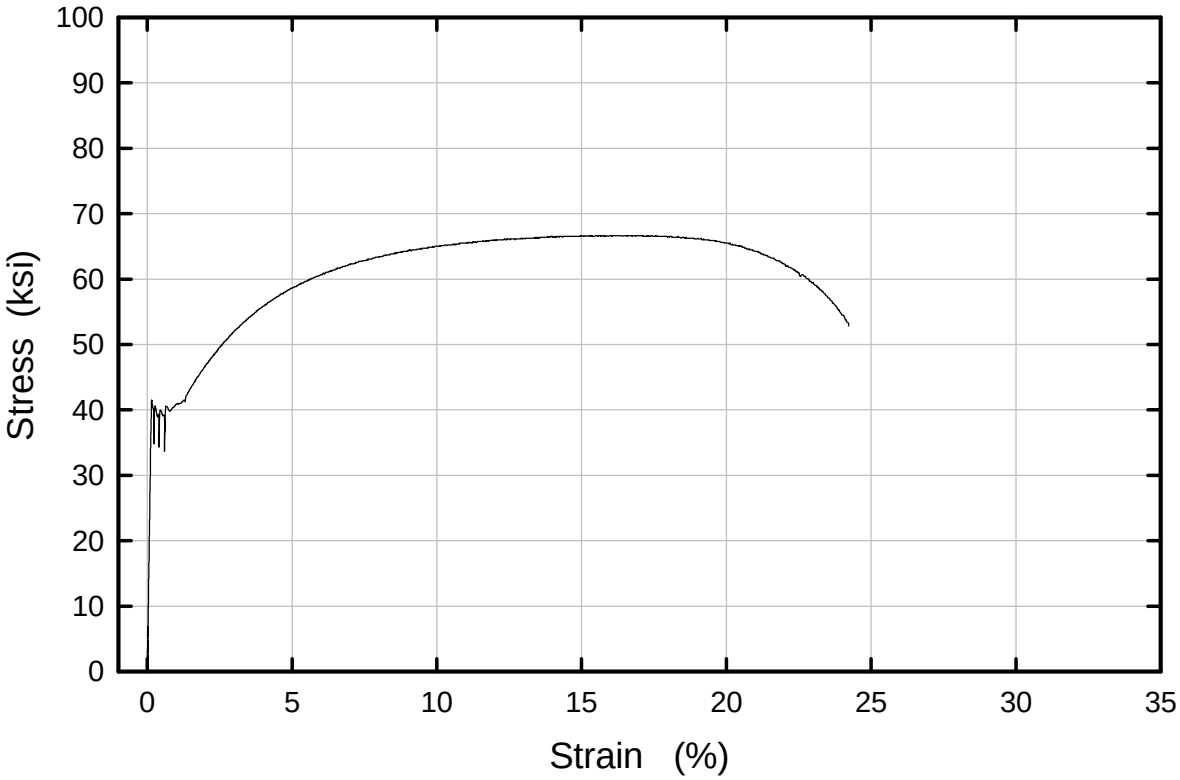

Figure 6: Typical Stress Versus Strain Curve for the Girder E Web (A-36 Steel)

Table 2.4 Statistical Composition of 18 Tension Test Samples from Cores (ASTM E-8 Testing Rate)

Property	Mean Value	Standard Deviation	95% Confidence Limit
F_y - 0.2% offset (ksi)	40.43	2.09	36.3
F_u (ksi)	70.19	2.07	66.1
Elongation @ 2 in. (%)	34.9	1.73	31.4

2.1.3 Charpy Vee Notch Tests on Web Plates

Tests were performed on the web plates from each of the girders at the fracture location at the TFHRC Structures Laboratory. A full CVN transition curve was developed at each location to define the variation in material toughness with temperature. Testing 24 individual specimens at eight different test temperatures develops each curve. All specimens were machined parallel to the rolling direction of the plate with the standard L-T orientation for the notch.

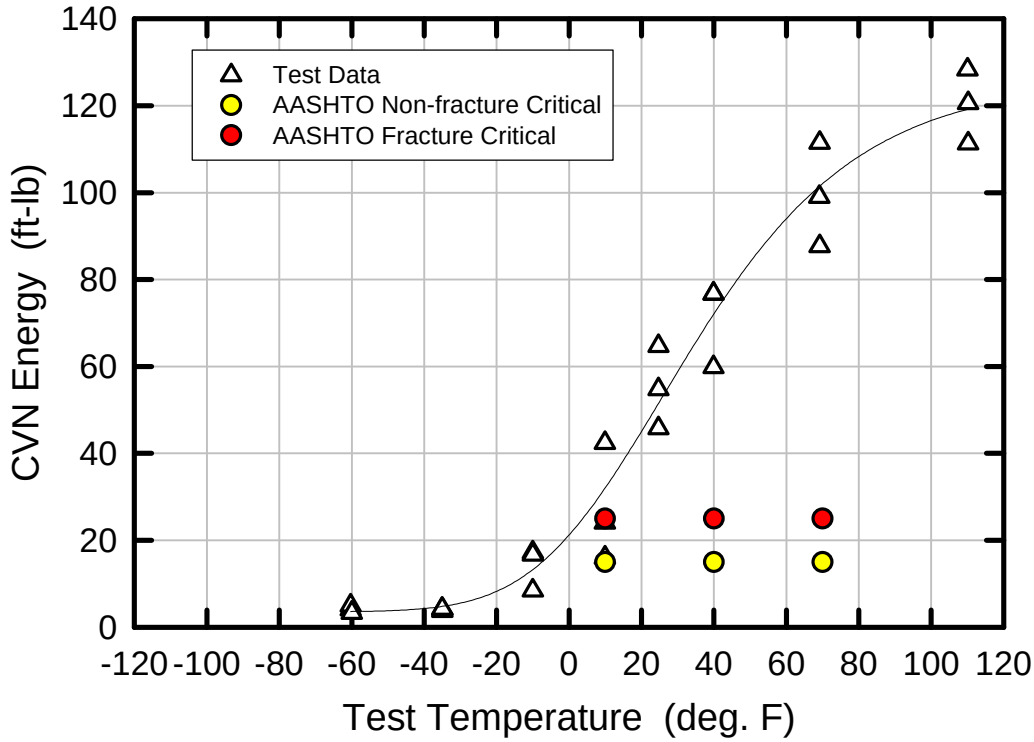

Figure 7: CVN Transition Curve for the Web Plate at D-28

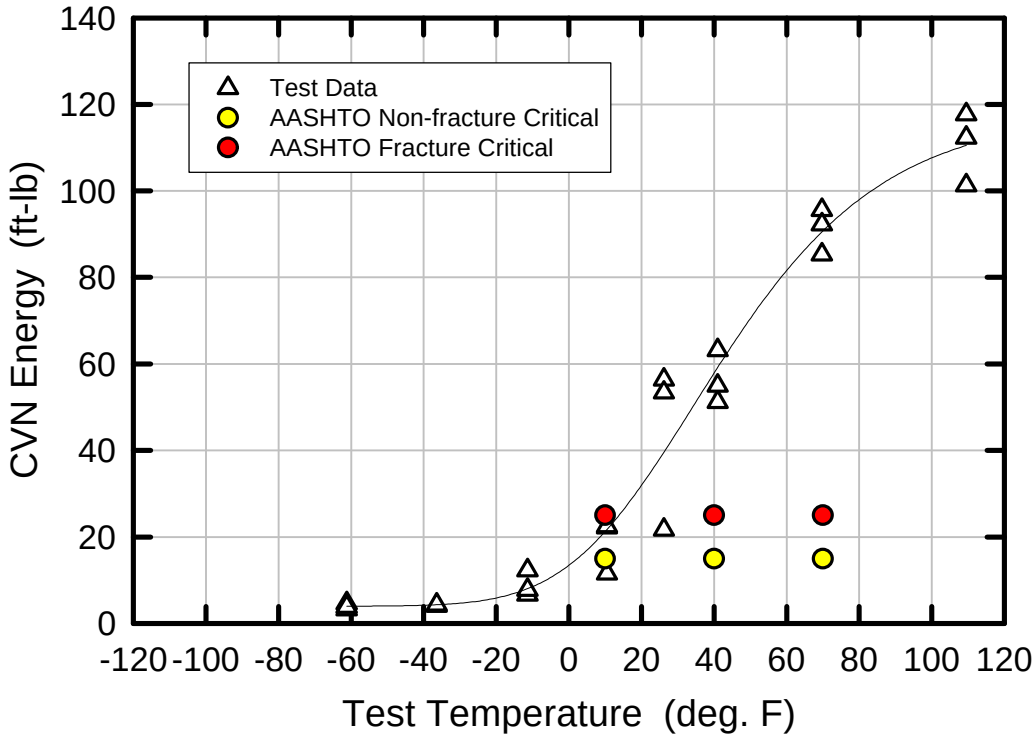

Figure 8: CVN Transition Curve for the Web Plate at E-28

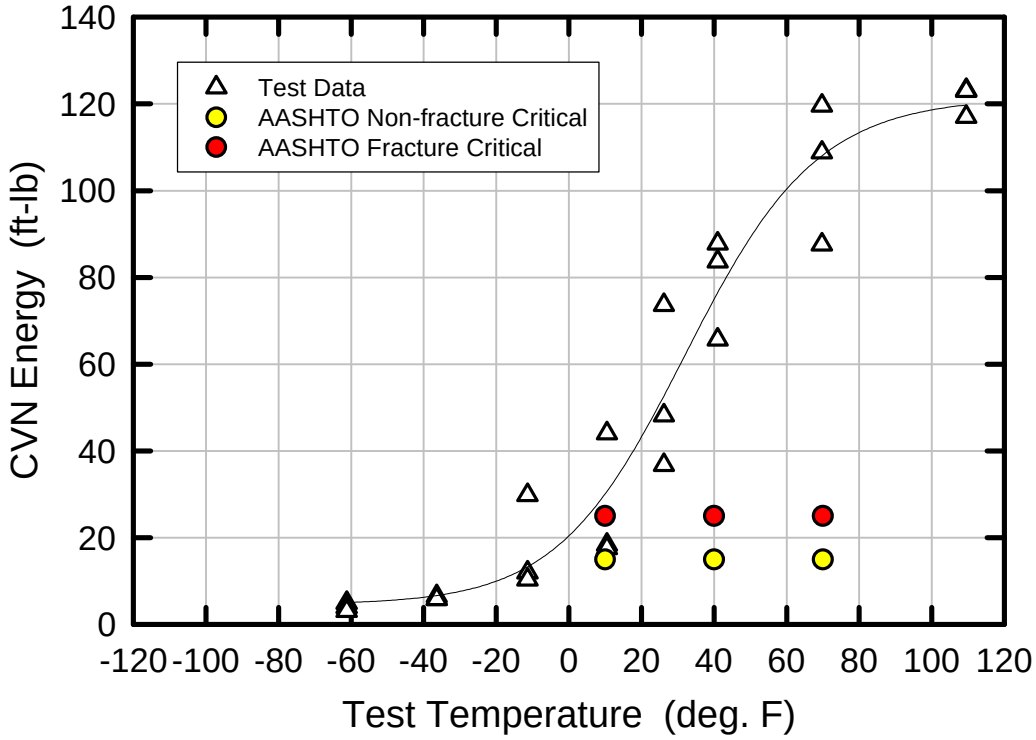

Figure 9: CVN Transition Curve for the Web Plate at F-28

Figures 7, 8, and 9 show the transition curves for the fracture locations on girders D-28, E-28, and F-28. All three locations have similar toughness and can be considered typical of data reported in the literature[12]. The AASHTO 1998 Specification requirements are plotted on the figures for reference. To meet the specification requirement, the average of three test results must exceed the specified minimum energy requirement and no individual test can fall below 2/3 of the requirement. The yellow circles show the requirements for non-fracture critical applications and the red circles show the higher toughness required for fracture critical applications. The test temperatures vary for each of the AASHTO temperature service zones. For A36 Steel, the test temperatures are +70, +40, and +10 ºF for service zones 1, 2, and 3, respectively. The Hoan Bridge falls in temperature service zone 2 where the lowest anticipated service temperature is –30 °F. The modern specification requirements are presented for reference only, there were no such specifications in 1969 when the bridge was designed.

It can be concluded that the web in all three locations would be suitable for use in zone 2, fracture critical applications. For service in zone 3, the material would be marginal for non-fracture critical applications and it would not pass the fracture critical requirement. If built today, the Hoan Bridge would be classified as zone 2, non-fracture critical, therefore it can be concluded that the toughness of the web material would have met modern toughness requirements.

One hundred eleven tests were performed on core samples from varied locations to study the toughness variability of all plate used in the three girder approach spans. Tests (3 specimens each) were compared from 37 different locations at two different temperatures. A histogram of results is shown in figure 10.

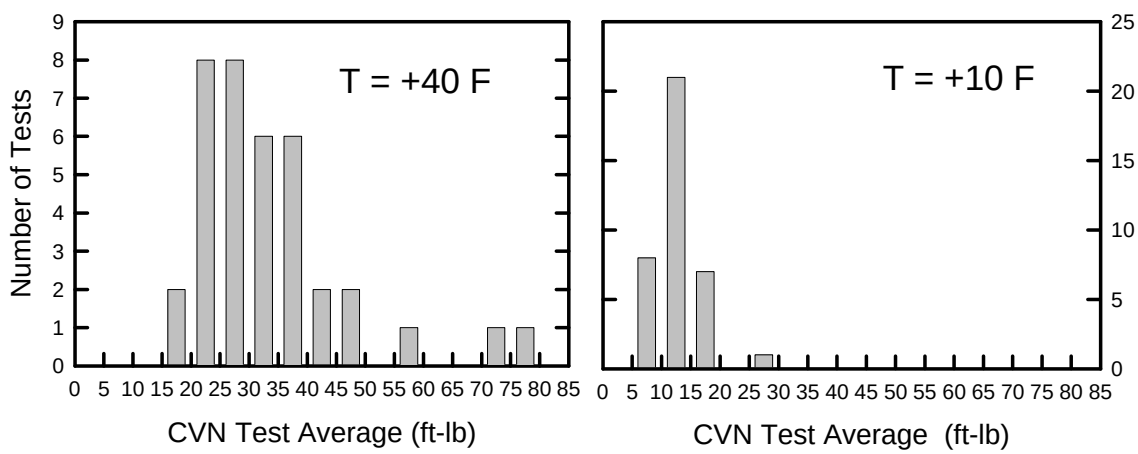

Figure 10: Histogram of CVN Tests From All Web Locations @ +10 ºF and +40 ºF

Compared to the 1998 AASHTO Specifications, All of the tests met the requirements for zone 2, non-fracture critical use. Seventy three percent of the tests met the zone 2 fracture critical requirement. For zone 3, only 27% of the tests met the non-fracture critical requirement. Again, it can be concluded that the web plate meets modern toughness requirements for zone 2, non-fracture critical use. The large number of sample locations gives a strong indication that the web plate properties are consistent throughout all of the three girder approach spans.

2.1.4 Fracture Toughness of Web Plates

The CVN test is used to measure steel toughness for quality control purposes, but the results cannot directly be used to predict fracture in structures. The theory of linear elastic fracture mechanics defines the critical stress intensity factor, K_{Ic}, as the standard measure of brittle fracture resistance. Like the CVN energy, K_{Ic} also depends on loading rate and temperature. Higher load rates and lower temperatures reduce material toughness. The most accurate way of determining K_{Ic} is to test compact tension C(T) specimens at load rates, temperatures, and plate thickness that match the service conditions of interest. However, measurement of K_{Ic} can only be measured under conditions where the material performs in a brittle manner. Any significant amount of ductility will invalidate the test result. Valid test results can only be obtained for thick plates and/or very low test temperatures for grade 36 material. Because the web plate is only ½ in. thick, C(T) tests will give little information that can be used to predict brittle fracture and toughness must be estimated from the CVN test results.

A correlation has been developed to estimate K_{Ic} in the lower transition region and lower shelf based on results of the CVN test.[6] The correlation involves a 2 step process to account for the effect of loading rate. In step 1, the dynamic fracture toughness, K_{Id} is calculated using the following equation:

$$K_{Id} = \sqrt{5(CVN)E} \qquad (1)$$

Where:	K_{Id} is the dynamic fracture toughness	(psi-in$^{1/2}$)
	CVN is the Charpy energy	(ft-lb)
	E is the elastic modulus	(psi)

In step 2, a temperature shift is applied to the CVN test temperature to account for the slower loading rate encountered under actual service conditions. Equation 2 gives the temperature shift for the 1 second loading rate that is commonly observed in bridges due to truck loading.

$$T_{shift} = 0.75\left(215 - 1.5\, s_{ys}\right) \qquad (2)$$

Where:	T_{shift} is the temperature shift	(°F)
	σ_{ys} is the nominal yield strength	(ksi)

Figures 11, 12, and 13 show the K_{Ic} and K_{Id} transition curves calculated from the CVN curves shown in the preceding section. The K_{Ic} curve is used to predict crack initiation under bridge live load rates, and the K_{Id} curve is used to predict the resistance to a dynamic crack that has initiated and is traveling at very high speed. Both curves predict toughness at the actual service temperature for the structure. Table 2.5 shows the lower bound fracture toughness that would be expected in the web plates at the indicated temperature.

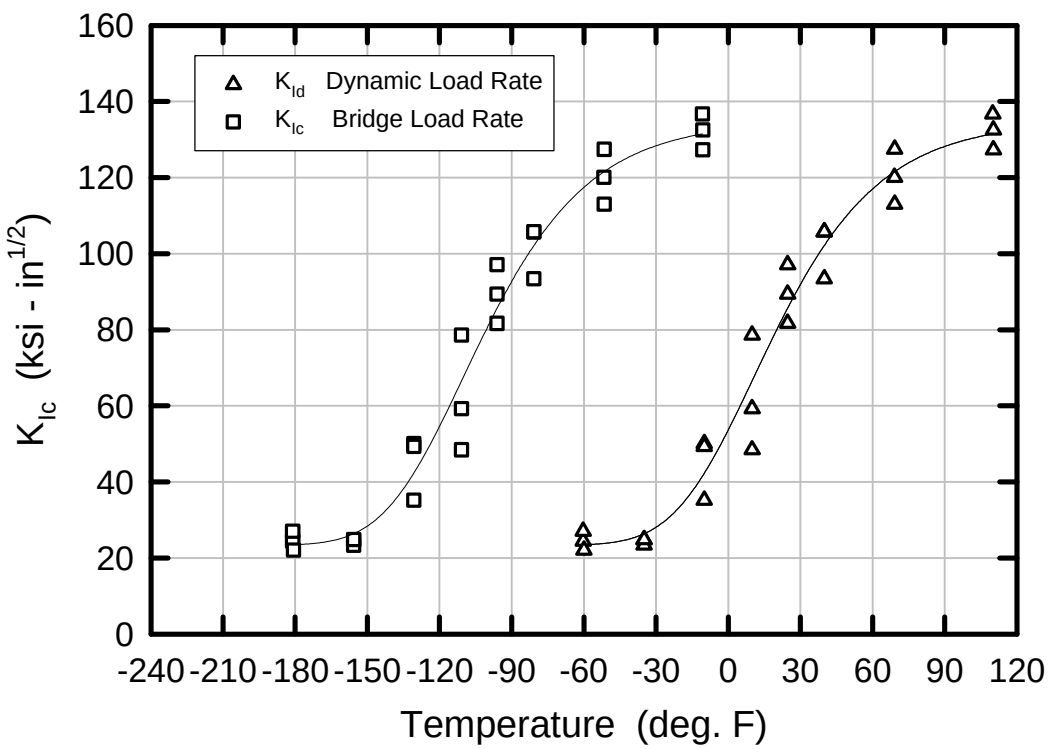

Figure 11: K_{Ic} Transition Curve for the Web at D- 28 Based on CVN Tests

Results show that the crack initiation resistance would be on the upper shelf at service temperatures encountered in the Hoan Bridge. The CVN correlation is technically not valid for upper shelf behavior, but the numbers give a relative indication of resistance to brittle fracture. The dynamic toughness is in the lower transition region, providing limited resistance to dynamic crack propagation.

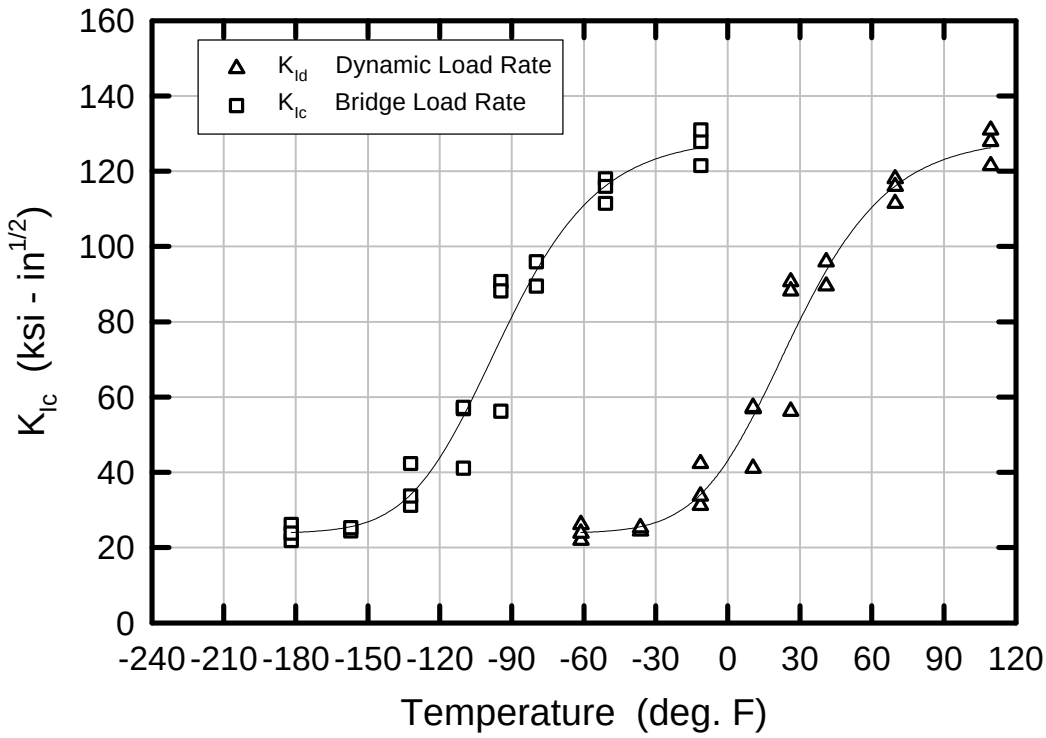

Figure 12: K_{Ic} Transition Curve for the Web Plate at E-28 Based on CVN Tests

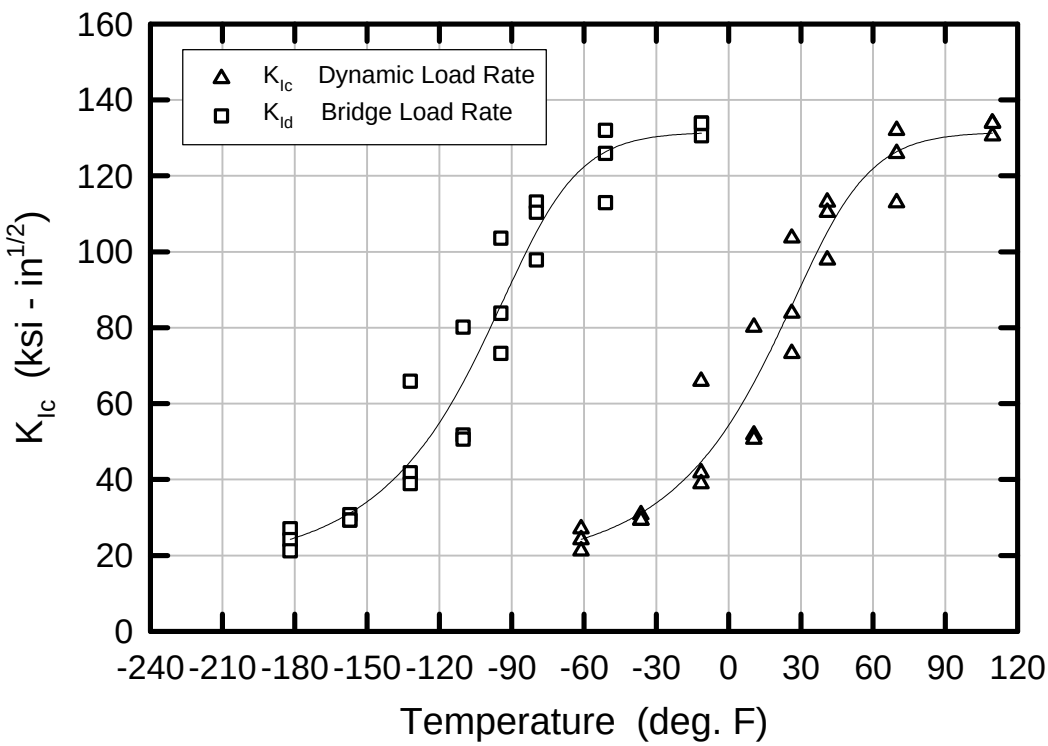

Figure 13: K_{Ic} Transition Curve for the Web Plate at F-28 Based on CVN Tests

Table 2.5 Estimated Fracture Toughness of Web Plates at Bridge Loading Rates

Plate Location	Probable Failure Temperature T = -10°F		Lowest Anticipated Service Temperature, Zone 2 T = -30°F	
	K_{Ic} (ksi-in$^{1/2}$)	Behavior	K_{Ic} (ksi-in$^{1/2}$)	Behavior
D-28	125	Upper Shelf	125	Upper Shelf
E-28	120	Upper Shelf	120	Upper Shelf
F-28	130	Upper Shelf	130	Upper Shelf

2.l.5 Summary - Properties of Web Plates

- The chemistry of all of the web plates tested is very uniform and exceeds the requirements of the A-36 specification.
- Sulfur, phosphorous, and silicon levels were uniformly low. High presence of these elements can reduce toughness, but there is no indication of this occurring for the 21 locations tested.
- All web plates meet the minimum strength requirements of the A-36 specification.
- The CVN toughness indicates that the material meets 1998 Specifications for use in zone II, non-fracture critical applications.
- There was a low variability of strength and toughness between different plates at different locations.
- The transition curves indicate that there is a low scatter in the data in the transition region indicating good material uniformity.
- The crack initiation toughness at bridge loading rates is on the upper shelf over the entire service temperature range for AASHTO zone 2. Temperature has little effect on the crack initiation toughness of the web plates.

2.2 PROPERTIES OF BOTTOM FLANGE PLATES

2.2.1 Chemical Composition of Bottom Flange Plates

Table 2.6 lists the chemical composition of the flange plates from the failure locations. All of the results meet the current AASHTO M270 Specifications for grade 50W steel (ASTM A-588)[5]. The percent composition of phosphorous and sulfur were well below the maximum allowed by the specification. There was also a close correlation between test results and the mill report values for each of the three flanges. Note that the mill report composition is the same for the D-28 and F-28 locations. The shop records indicate that they were stripped from the same plate.

Table 2.6 Composition of Bottom Flange Material at Fracture Locations

Location and Source		Element (%) Composition									
		C	Mn	P	S	Si	Cu	Ni	Cr	Mo	V
D - 28	Test	.149	1.04	.008	.011	.25	.29	.15	.52	.004	.044
	Mill	.16	1.13	.010	.021	.26	.30	---	.54	---	.05
E - 28	Test	.168	1.13	.007	.012	.25	.27	.16	.54	.005	.045
	Mill	.16	1.12	.010	.019	.24	.26	---	.55	---	.05
F - 28	Test	.149	1.10	.003	.011	.25	.30	.16	.55	.004	.047
	Mill	.16	1.13	.010	.021	.26	.30	---	.54	---	.05
ASTM A-588		.19 max	.80 to 1.25	.04 max	.05 max	.30 to .65	.25 to .40	.40 max	.40 to .65	---	.02 to .10

2.2.2 Strength of Bottom Flange Plates

Table 2.7 shows the test results for samples taken from the bottom flange plates near the failure locations. All tests utilized the standard 0.505 in. round specimen with a 2 in. gage length cut from the flange plates at the ¼-thickness location, except one test was performed on the girder D flange at mid-thickness to check thickness uniformity. All specimens were oriented parallel to the rolling direction of the plate. The table shows an average of the results for the number of tests indicated. The test rate was about 30 ksi/min, at the slow end of allowable test speeds in the ASTM E-8 specification.

Table 2.7 Average Tension Tests of Flange Plates at Room Temperature

Plate	Source	F_y 0.2% offset (ksi)	F_y Upper Yield (ksi)	F_u (ksi)	E (ksi)	% Elong. (2")
E-28 Flange	2 Tests	51.1	52.2	81.8	31,281	27.4
	Mill	57.2	C	83.3	C	33
F-28 Flange	2 Tests	52.5	54.7	78.1	28,936	30.6
	Mill	59.9	---	83.9	---	27.7
D-28 Flange	3 Tests	46.6	50.3	74.5	29,263	29.6
	1Test[(a)]	42.5	47.4	70.4	28,887	32.3
	Mill	59.9	---	83.9	---	27.7
ASTM A-588		50 (min)	---	70 (min)	---	21 (min)

(a) Test specimen cut from the mid-thickness location.

The E and F flanges both met the minimum requirement for 0.2% offset yield strength, but the D-28 location fell below specification by about 7%. After the first two tests showed this result, two additional tests were performed from a sample location about 24 in. away from the first sample location. The two additional tests confirmed the result. The additional test sampled from the mid-thickness location gave results that were about 15% below the specified yield. It is usual, however, for tests to give lower strength at the mid-thickness location for thicker plates. The reason for this

low strength in the flange plate from D-28 is not known. The F-28 and D-28 flanges are reported to have been cut from the same plate according to the fabrication records.

The tensile strength of the D-28 flange is also somewhat lower than the F-28 flange, however both met the Specification requirements. The 3 in. thick plate at E-28 also met all specification limits for strength. All plates well exceeded the minimum percent elongation, indicating good ductility.

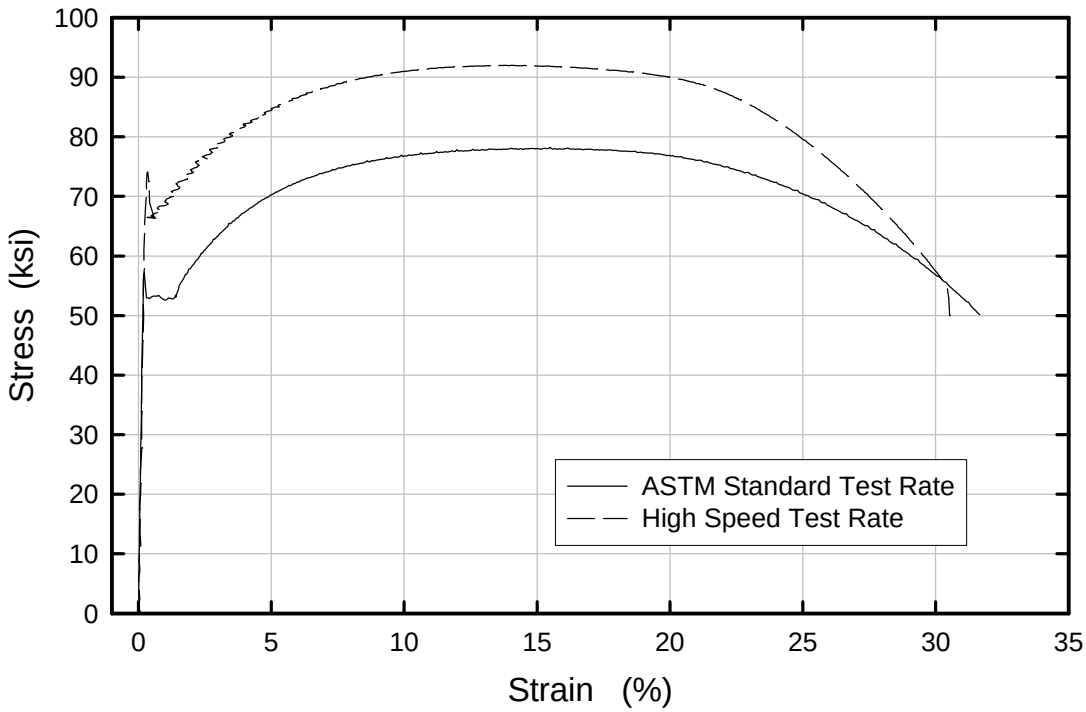

Figure 14: Typical Stress-Strain Curve for the 2 1/4 in. Flange Plate at F-28 (A-588 steel)

The solid line in figure 14 shows a typical stress strain curve recorded during testing. The upper yield point is reported in addition to the 0.2% offset yield strength. The elastic modulus is also calculated from linear regression on the elastic portion of the stress strain plot. The dashed line shows the same steel tested at a dynamic load rate at -30 °F. This shows that the strength clearly is elevated at higher strain rates and lower temperatures. The dashed line also shows a pronounced upper yield point due to the high rate of loading.

2.2.3 Charpy Vee Notch Tests of Bottom Flange Plates

Tests were performed on the flange plates from each of the girders at the fracture location at the TFHRC Structures Laboratory. Similar to the web plates, a full CVN transition curve was developed at each location to define the variation in material toughness with temperature. All specimens were machined from the ¼ thickness location parallel to the rolling direction of the plate. The notch was machined in the standard L-T orientation.

Figures 15, 16, and 17 show the transition curves for the bottom flange plates at the fracture locations on girders D-28, E-28, and F-28. Both 2-¼ in. plates (D-28 and F-28) have similar transition curves that show relatively good toughness and low variability. The transition curve was different for the 3 in. plate. There was a larger scatter band for the data and the transition temperature is shifted about +40 °F. The toughness of the 3 in. plate was significantly lower than the 2-¼ in plates.

The AASHTO 1998 Specification requirements for grade 50W steel are plotted on the figures for reference. (See section 2.1.3 for an explanation) For each plate, only one test (3 specimens) was performed at the standard test temperatures specified in the AASHTO materials specification. One sample is insufficient to make any definite conclusions with respect to meeting specifications. The AASHTO Materials Specification allows retests for plates that cannot

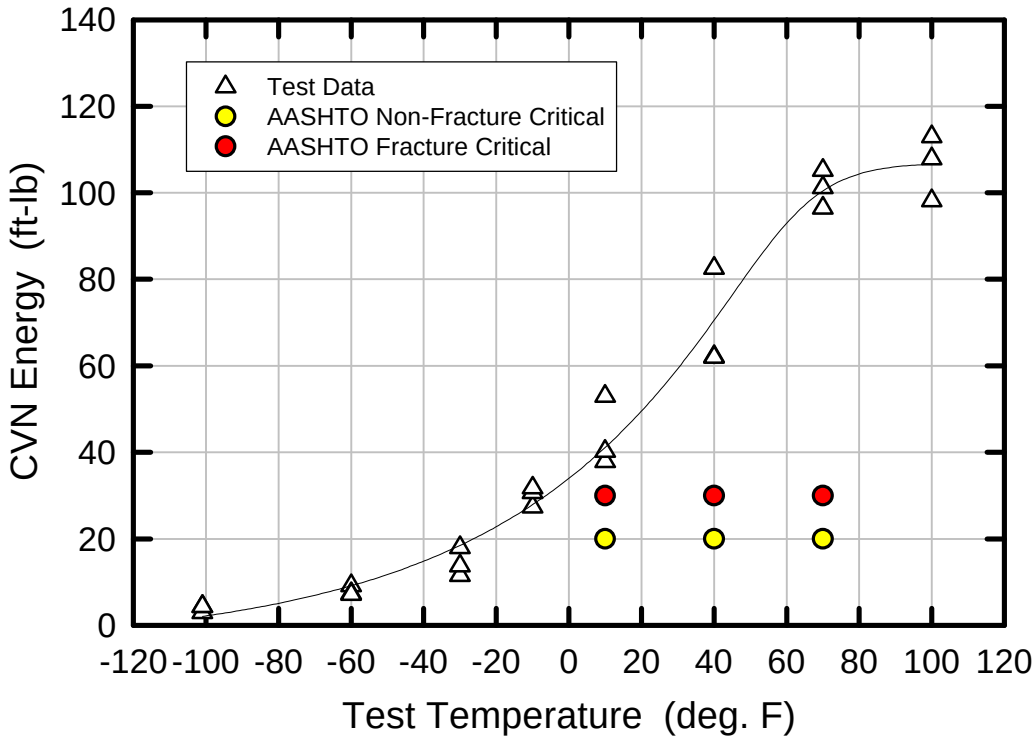

Figure 15: CVN Transition Curve for the Bottom Flange Plate at D-28

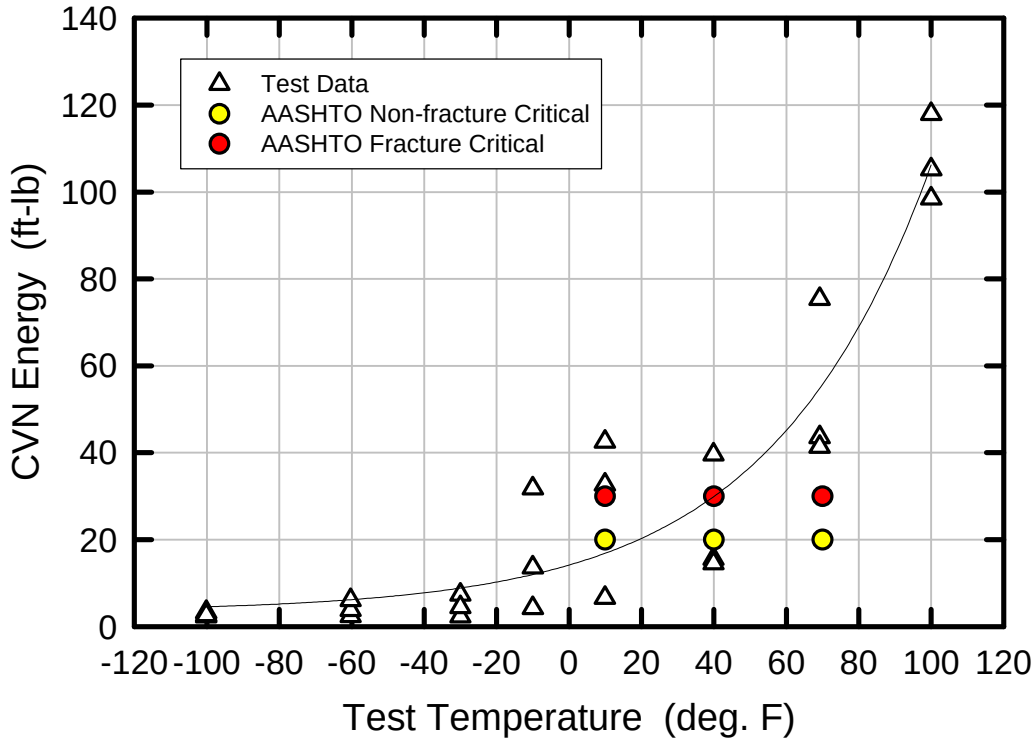

Figure 16: CVN Transition Curve for the Bottom Flange at E-28

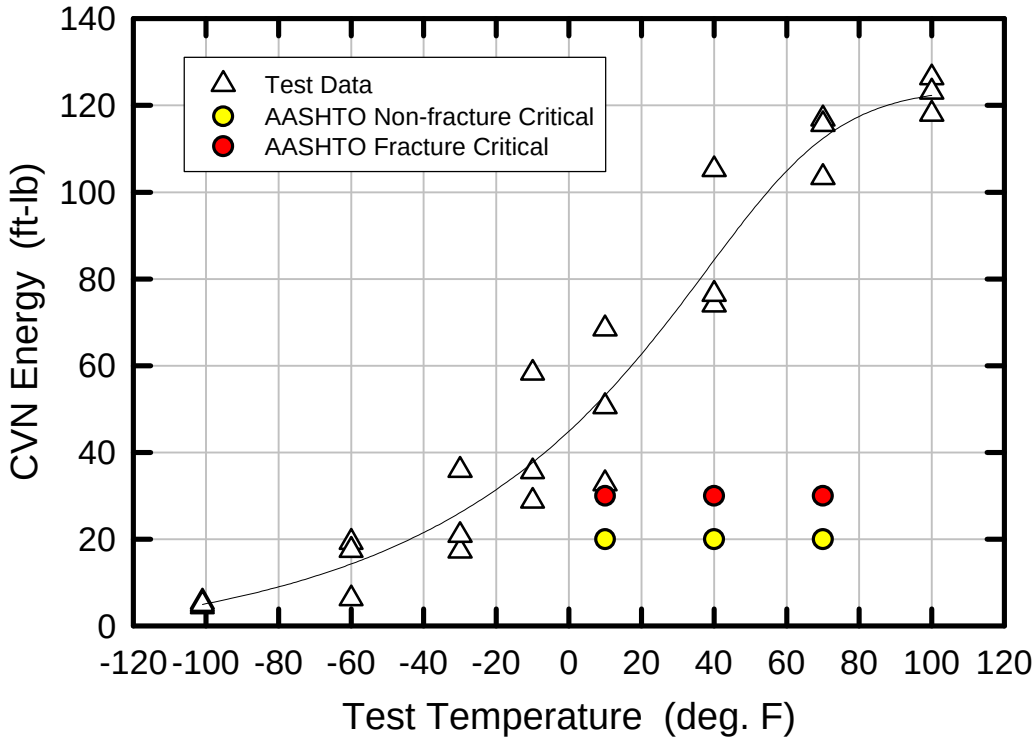

Figure 17: CVN Transition Curve for the Bottom Flange at F-28

meet specifications the first time. For this small sample size, the transition curve regression line provides a better indicator than re-tests since it helps average out variability. Based on the transition curve, the 2-¼ in. flange plates at D-28 and F-28 would have exceeded the 1998 requirement for zone 3, fracture critical service. The 3 in. flange plate at E-28 would generally meet the requirement for zone 2, non-fracture critical service. However, without regression analysis, two of the three specimens tested at +40°F would have fallen below the required 20 ft-lb and the plate would only have passed the requirement for service in zone 1.

2.2.4 Fracture Toughness of Bottom Flange Plates

The fracture toughness of the flange plates was directly measured at two temperatures using the compact tension (C(T)) test. In addition, equations 1 and 2 were used to calculate the fracture toughness transition curves for the bottom flange plates from the CVN data. Similar to the web plates, both the K_{Ic} and K_{Id} curves are plotted to predict the crack resistance under both dynamic and bridge loading rates.

C(T) tests were performed on the flange plates from girders D and E. The girder F flange was not tested, but the properties should be similar to girder D since they were both cut from the same plate. All tests were conducted according to the ASTM E-1820 combined standard for measuring fracture toughness in metallic materials. Two-inch thick (2T-C(T)) specimens were machined from the center of the flange plates with the notch orientation transverse to the rolling direction of the plate (L-T). A total of four tests were conducted on each flange at two different temperatures as shown in table 2.8. The –30 ºF temperature was chosen to evaluate toughness at the lowest anticipated service temperature for AASHTO zone 2.

Table 2.8 Compact Tension Test C(T) Matrix for Flange Plates

Flange Plate Location	Specimen ID	Test Temperature (°F)	Load Rate (seconds)
E-28	DBF-CT1	+70	Static
	DBF-CT2	-30	Static
	DBF-CT3	-30	0.20
	DBF-CT4	-30	0.02
D-28	EBF-CT1	+70	Static
	EBF-CT2	-30	Static
	EBF-CT3	-30	0.20
	EBF-CT4	-30	0.02

During the static tests, the specimens were periodically unloaded to measure the amount of crack extension occurring during the test. The higher rate tests were pulled continuously and the load rate represents the approximate time it took to reach maximum load. Under service live loads, bridges usually experience a load rate around 1 second. The 0.2 second rate is about 5 times faster and serves as a slightly conservative estimate of bridge loading rates. The 0.02 sec. rate can be classified as intermediate, about 50 times faster than bridge loading rates but far short of the high dynamic rate caused by a propagating brittle fracture.

Figures 18 and 19 show the load versus load line displacement curves for the bottom flange plates at locations D-28 and E-28, respectively. The results of all four tests are overlaid in the figures. The unloading data has been omitted from the static tests for clarity in the figures. The load versus load-line-displacement curves provide a good general indication of the ability of steel to resist fracture in service. Similar to a load versus displacement plot for a structural test, a ductile test reaches it's maximum capacity and is capable of sustaining large deformations without fracture. When material toughness drops, the specimens fracture prematurely at some point during the test. Fractures occurring during the initial elastic loading part of the curve indicate brittle behavior. Some amount of non-linearity before fracture indicates some ductility and transitional toughness behavior.

In figure 18, the static test at room temperature shows a large amount of ductility and the crack is extending through stable tearing instead of unstable fracture. When the temperature is reduced to –30 °F, the ductility is reduced but the maximum load increases due to the elevated yield strength of the steel at low temperatures. This test ended in a ductile fracture, but there was a significant amount of plastic deformation prior to failure. The tests at the higher load rates show almost a total lack of ductility and there is very little plastic deformation prior to fracture. The failure mode is not ductile, but the relatively high load at fracture still indicates significant fracture resistance.

Figure 19 shows the same set of four curves for the 3 in. flange plate at location E-28. There is almost no ductility in any of the tests, even at high temperatures. At room temperature the steel has relatively good crack resistance, but there is a clear decrease in maximum load for the low temperature and high rate tests.

The linear elastic fracture toughness of the material was calculated from the data shown in figures 18 and 19 according to procedures of the ASTM E-1820 specification. The first step in the procedure is to calculate a provisional toughness K_Q. There are several way this can be calculated, but for this report K_Q is based on the maximum load occurring before fracture. To be called K_{Ic}, the provisional K_Q must satisfy several validity checks to insure that true plain strain conditions are achieved. The results of these calculations are shown in table 2.9. Only two of the eight tests resulted in valid K_{Ic} numbers.

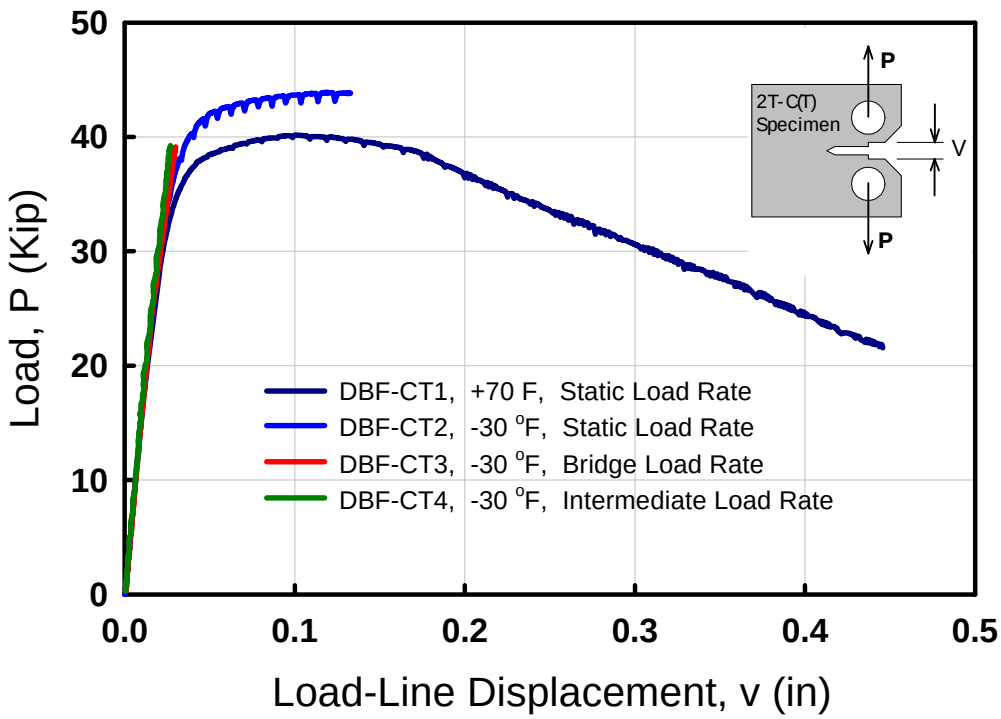

Figure 18: C(T) Test Data for the Bottom Flange at D-28

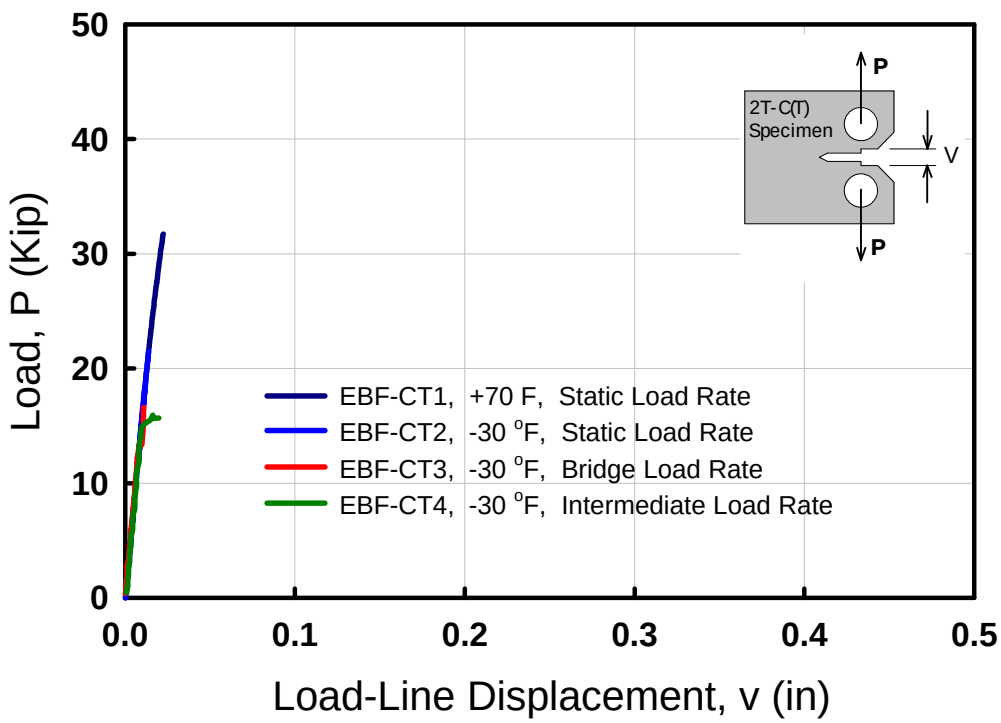

Figure 19: C(T) Test Data for the Bottom Flange at E-28

Table 2.9 Toughness Results from the C(T) Tests

Location	Temperature (EF)	Load Rate	P_{max} (kip)	K_Q (ksi-in$^{1/2}$)	K_{Ic} (ksi-in$^{1/2}$)
D-28 Bottom Flange	+70	Static	40.15	112.6	--- [(a)]
	+70	Static	43.88	123.3	--- [(a)]
	-30	Bridge	39.09	103.0	--- [(a)]
	-30	Intermediate	39.25	103.0	--- [(a)]
E-28 Bottom Flange	+70	Static	31.74	84.9	--- [(a)]
	+70	Static	21.49	57.3	--- [(a)]
	-30	Bridge	16.62	44.7	44.7
	-30	Intermediate	15.91	42.9	42.9

(a) Invalid K_{Ic} – Insufficient specimen thickness to reach plane strain conditions.

Figures 20, 21, and 22 show the K_{Ic} transition curves calculated from the CVN data using equations 1 and 2 from section 2.1.4. The curve for bridge loading rates, indicated by the open square symbols, shows the material's resistance to brittle fracture initiation at any given service temperature. Once a brittle fracture initiates, the cracks propagate at an explosively high rate of speed. The dynamic load rate curve shows how the material's fracture resistance decreases at very high load rates. The toughness values from the dynamic curve can be used to estimate the point where crack arrest will occur during a brittle fracture event.

The horizontal green line curve marks the approximate location of the nil-ductility transition (NDT). This point has been shown to be a reasonable indicator of when the material starts to show some degree of ductile fracture.[(6)] Technically, the theory of linear elastic fracture mechanics only is valid for data below the line where fracture occurs under plane strain conditions. In the upper transition region and on the upper shelf the mode of fracture changes from brittle to ductile. However, K continues to provide a useful indication of fracture resistance in the upper regions and it is common practice to extend the use of linear elastic fracture mechanics to predict ductile fracture.

The data from the C(T) tests are plotted with solid symbols on figures 20, 21, and 22 to show how it compares to the data calculated from the CVN tests. The red symbols indicate that the tests did not yield valid K_{Ic} results and the K_Q value is plotted. Green symbols indicate a valid K_{Ic} test. The shape of the symbol corresponds to the loading rate during testing.

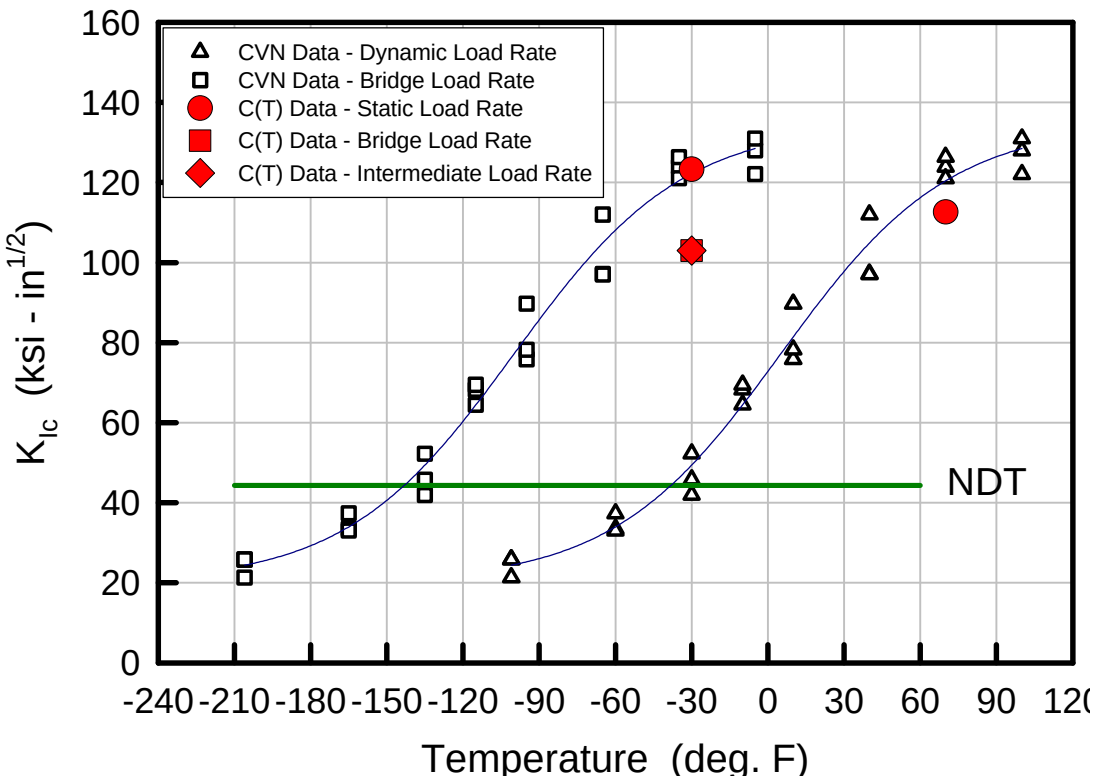

Figure 20: K_{Ic} Data for the Bottom Flange at Location D-28

Figure 20 shows the fracture toughness of the 2 ¼ in. bottom flange plate at location D-28. This is the flange where crack arrest was found to have occurred during the failure. The C(T) test results correlate well with the CVN data for the bridge-loading rate. There is little difference in the data between the bridge load rate and the intermediate load rate tests, but both show somewhat lower toughness than the static tests. At the lowest anticipated service temperature of –30 °F, the fracture initiation toughness is expected to be close to upper shelf with K > 100 ksi-in$^{1/2}$. Little variation in crack initiation toughness is expected within the range of bridge service temperatures. The toughness for crack arrest is lower, as expected. At -30 °F, K is expected to be around 40 ksi-in$^{1/2}$, close to the point where brittle behavior is expected. The slope of the dynamic load rate curve indicates that toughness will be expected to increase rapidly as a function of temperature.

Figure 21 shows the fracture toughness of the 3 in. flange plate at location E-28. For crack initiation at bridge load rates, the C(T) test data indicates lower toughness than the data derived from the CVN tests. The CVN data indicates that behavior would be in the upper transition region, while C(T) tests indicate lower transition region. At –30 °F, the fracture initiation toughness from the C(T) tests is down around 40 ksi-in$^{1/2}$, compared to about 80 ksi-in$^{1/2}$ for the CVN data. Part of this difference can be explained by the specimen size of the C(T) tests. To get a 2 in. thick specimen from 3 in. thick material, 1/2 in. had to be machined off each surface. Because the material at the surface of plates is usually tougher than that at the center, the average toughness of the C(T)

specimen will be lower than the average for the full thickness plate. Therefore, the C(T) tests should be considered a somewhat conservative lower bound on the data. Note that the C(T) data below the NDT line gives valid K_{Ic} behavior, while the data above the line is invalid. This indicates the NDT line is giving a reasonable prediction of the transition point between purely brittle and somewhat ductile fracture.

The dynamic load rate curve indicates that the E-28 flange has very little resistance to fracture at high load rates. At –30 °F, the dynamic toughness can be as low as K = 20 ksi-in$^{1/2}$, and little increase will be expected until the temperature increases above 0 °F.

Figure 22 shows the fracture toughness of the 2-¼ in. bottom flange plate at location F-28. According to the fabrication records, the D-28 and F-28 flanges were both stripped from the same plate. Both the dynamic and bridge load rate curves are similar to those from location D-28, therefore the toughness of the two flanges can be considered similar.

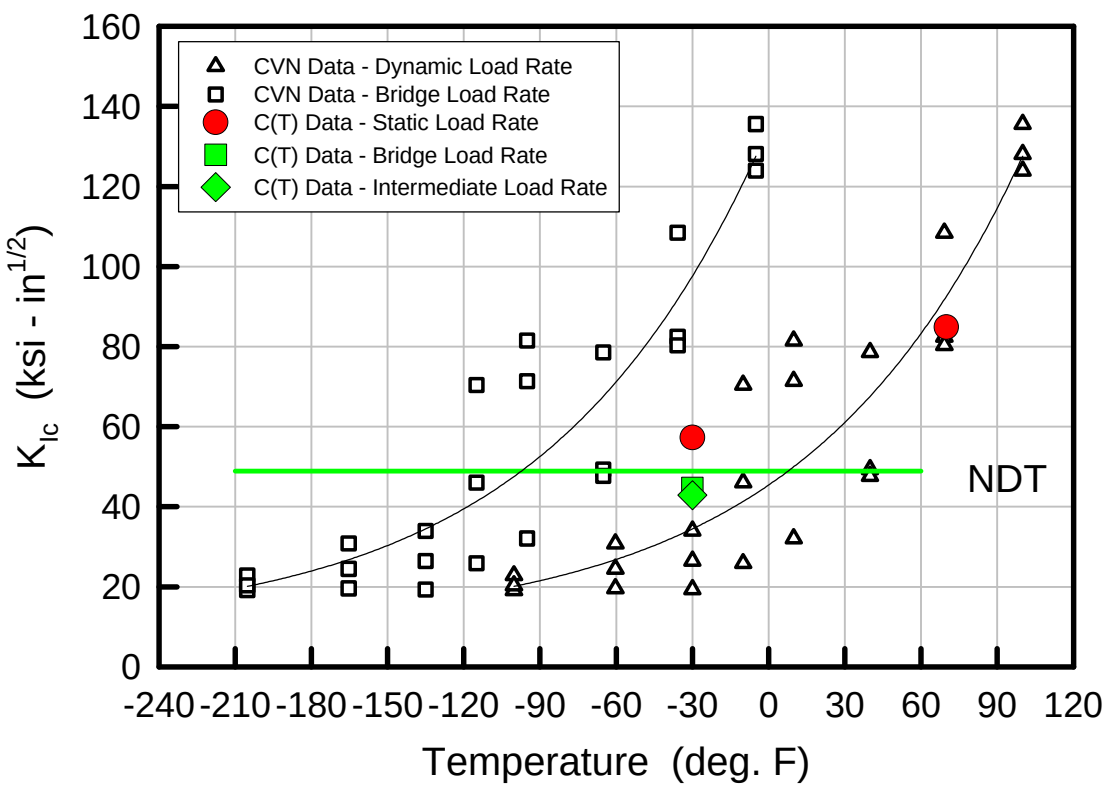

Figure 21: K_{Ic} Data for the Bottom Flange at Location E-28

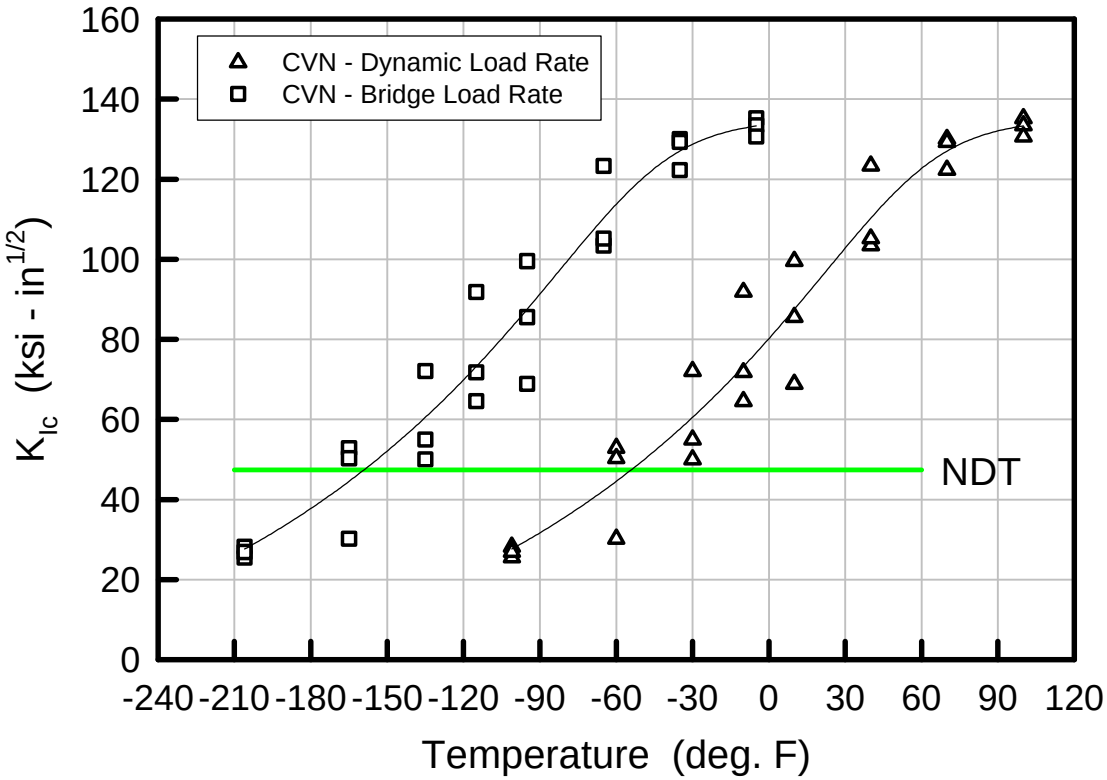

Figure 22: K_{Ic} Data for the Bottom Flange at Location F-28

Tables 2.10 and 2.11 show an estimate of the toughness and type of behavior that will be expected at the indicated service temperatures for both crack initiation and crack arrest. The toughness values are chosen in the judgment of the authors to represent a reasonable lower bound estimate based on both the C(T) and CVN data.

Table 2.10 Estimated Fracture Toughness of Bottom Flange Plates at Bridge Loading Rates

Plate Location	Probable Failure Temperature T = -10°F		Lowest Anticipated Service Temperature, Zone 2 T = -30°F	
	K_{Ic} (ksi-in$^{1/2}$)	Behavior	K_{Ic} (ksi-in$^{1/2}$)	Behavior
D-28	110	Upper Shelf	100	Upper Shelf
E-28	50	Lower Transition	40	Lower Transition
F-28	110	Upper Shelf	100	Upper Shelf

Table 2.10 shows that there is a large difference in the crack initiation resistance between the 2 ¼ and 3 in. flange plates. The 2-¼ in. plates are on the upper shelf throughout the service temperature range expected for the Hoan Bridge, indicating there is little chance of brittle fracture initiation. The 3 in. plate has much lower toughness down in the lower half of the transition region. At –30 °F, the 3 in. plate is around the limit where purely brittle fracture becomes possible. This does not mean that brittle fracture will occur, only that it becomes possible under certain combinations of defect size and loading. The general intent of the modern AASHTO fracture toughness specifications is to insure that steel toughness is above the NDT limit at the lowest possible service temperature. The C(T) data shows that the 3 in. plate is right at the limit. The CVN test data shown in figure 16 indicates that the 3 in. flange barely meets the modern AASHTO requirements for zone 2, non-fracture critical use. This is consistent with the C(T) data and shows the plate meets the intent of the fracture control plan, but just barely.

Table 2.11 Estimated Fracture Toughness of Bottom Flange Plates at Dynamic Loading Rates

Plate Location	Probable Failure Temperature T = -10°F		Lowest Anticipated Service Temperature, Zone 2 T = -30°F	
	K_{Id} (ksi-in$^{1/2}$)	Behavior	K_{Id} (ksi-in$^{1/2}$)	Behavior
D-28	60	Transition	42	Close to NDT
E-28	25	Lower Shelf	20	Lower Shelf
F-28	60	Transition	47	Close to NDT

Table 2.11 provides the lower bound estimates of resistance to dynamic cracks traveling at high speed. These values provide a reasonable estimate of crack arrest toughness. Again, there is a clear difference between the 2-¼ and 3 in. plates. The thicker plate is on the lower shelf and will expected to have very low resistance to dynamic cracks. The 2-¼ in plates are in the transition region and would expect to show some degree of ductility and resistance to dynamic cracks. This indicates that crack arrest is possible for the 2-¼ in. plate depending on conditions, but the 3 in. plate will have very little ability to arrest dynamic cracks.

2.2.6 Summary - Properties of Bottom Flange Plates

- The chemistry of all of the bottom flange plates tested is very uniform and exceeds the requirements of the A-588 specification.

- The 2-¼ in. flange at D-28 has yield strength about 7% below the specified minimum strength for A588 steel. Tensile strength, ductility, and toughness all meet the requirements for A-588 steel, however. In addition, the flange steel meets all of the strength requirements of A-441 steel for which the girder was originally designed.

- The bottom flange plate at locations F-28 and E-28 both met all applicable strength requirements for A-588 steel.

- The CVN toughness indicates that the 3 in. flange material would just barely meet the 1998 AASHTO Specification requirements for use in zone II, non-fracture critical applications.

- The CVN toughness indicates that the 2 ¼ in. flanges would meet the more severe 1998 AASHTO requirements for zone 3, fracture critical use.

- The 2-¼ in. flange plates at D-28 and F-28 show upper shelf behavior indicating there is little likelihood of brittle fracture initiation in service. There is little variability of crack initiation toughness over the service temperature range for zone 2.

- The 3 in. flange plate at E-28 shows crack initiation toughness falling in the lower half of the transition region. This generally meets the intent of the modern AASHTO fracture control plan but brittle fracture might be possible under certain conditions. The crack initiation toughness will slowly increase as a function of temperature.

- The crack arrest toughness of the 2-¼ in. flanges at D-28 and F-28 is in the transition region. The ability to arrest dynamic cracks increases as a function of temperature.

- The 3 in. flange has very low crack arrest toughness at service temperatures below about +30EF. Above this temperature, crack arrest toughness begins to increase.

- Since the D-28 flanges were the only ones that did not fracture, their failure to meet the yield strength criteria for A-588 steel was beneficial in resisting the brittle fracture. This is discussed further in section 5.3.

3. STRUCTURAL MODELS AND FIELD MEASUREMENTS

3.1 GLOBAL STUCTURAL ANALYSIS

A model of the Hoan bridge approach unit S2A has been generated using STAAD Pro 2000/2001. The model has been generated to perform the dual purposes of aiding in the investigation of the failure and to evaluate various retrofit strategies.

The model uses a combination of beam members and plate elements with both in plane and bending capacity. The three spans of unit S2A have been modeled with 3 dimensional assemblies to capture the global effects of interest in both the main load carrying members (girders, floorbeams, and stringers) and the secondary members (deck, transverse connection plates, and bottom flange bracing members). A typical cross-section is shown in Figure 23.

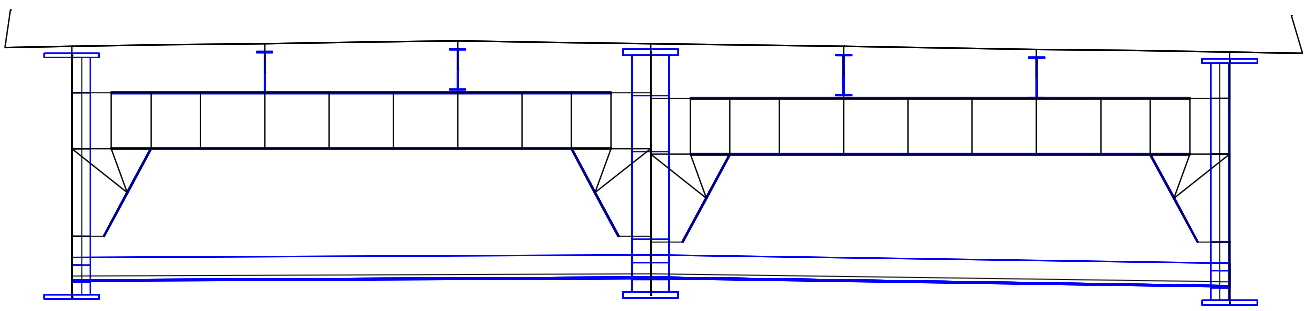

Figure 23: Typical Cross Section of Global Model

3.1.1 Load Cases

The model has been analyzed for cases of:

1. Dead Load
   A. Original structural and non-structural components.
   B. 2 inch thick asphalt concrete wearing surface added in 1989.

2. Live Loads
   A. AASHTO Standard Specification HS20-44 Lane Loading
   B. East and Center lane positions of a short rear axle length truck considered typical of truck traffic on the Hoan with a Gross Vehicle Weight of 67.6 kips for the load test comparisons, as shown in Figure 24, and 73.7 kips for the WIM study.

3. Wind Load (AASHTO specifies 50 lb/ft^2 ≥ 300 lb/ft on the exterior surface).

4. A uniform temperature drop of 30 degrees Fahrenheit.

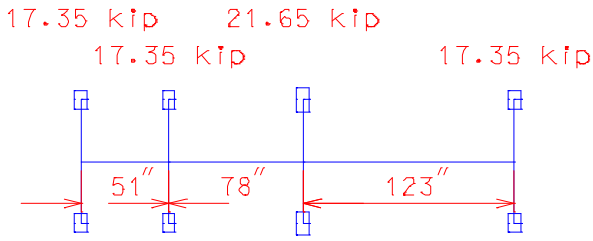

(a) Test Truck **(b) WIM Truck**

Figure 24: Test Truck and WIM Loading

5. A temperature gradient where the concrete and the top flange of the girders experience no temperature change due to the thermal mass of the deck and the steel beneath the top flanges of the girders experiences a temperature drop of 15 degrees Fahrenheit.

Each of the above load cases has been considered in terms of the failure at Panel Point 28 of unit S2A. Each load case has also been used on a version of the model where the bracing members are removed to show how the bracing members affect the behavior and whether they are required.

3.1.2 Results

The members reported on are given in the following table and shown in the Figures 25 and 26. Web stresses in the global model are collected from elements 9242 and 9353 on the center girder.

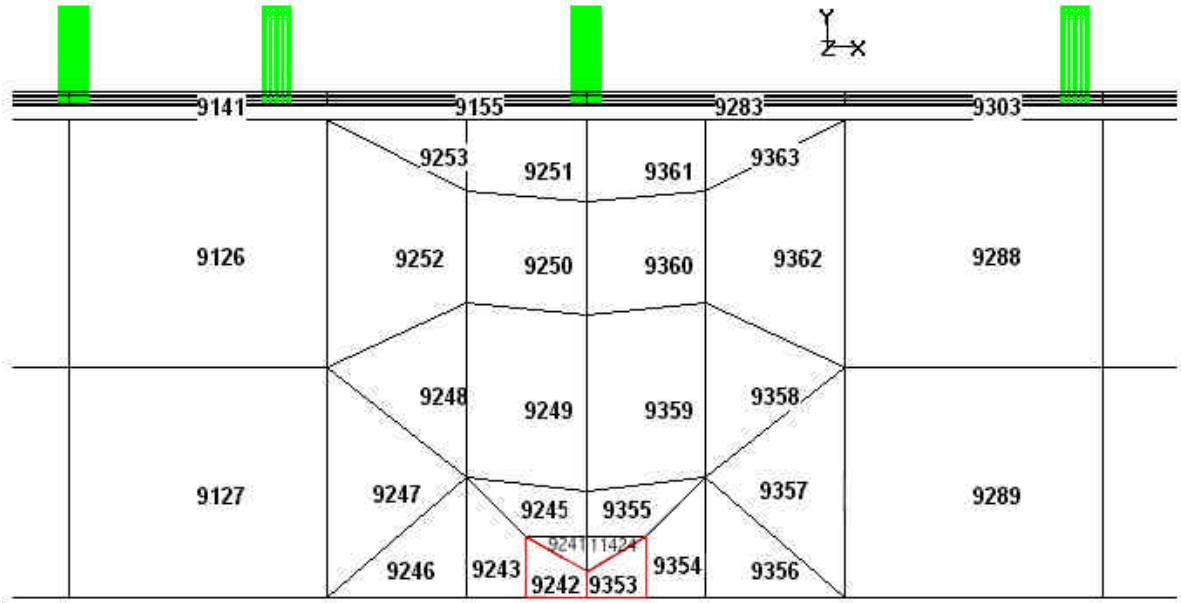

Figure 25: Web Elements at E28 (shown with 4 axle truck loading)

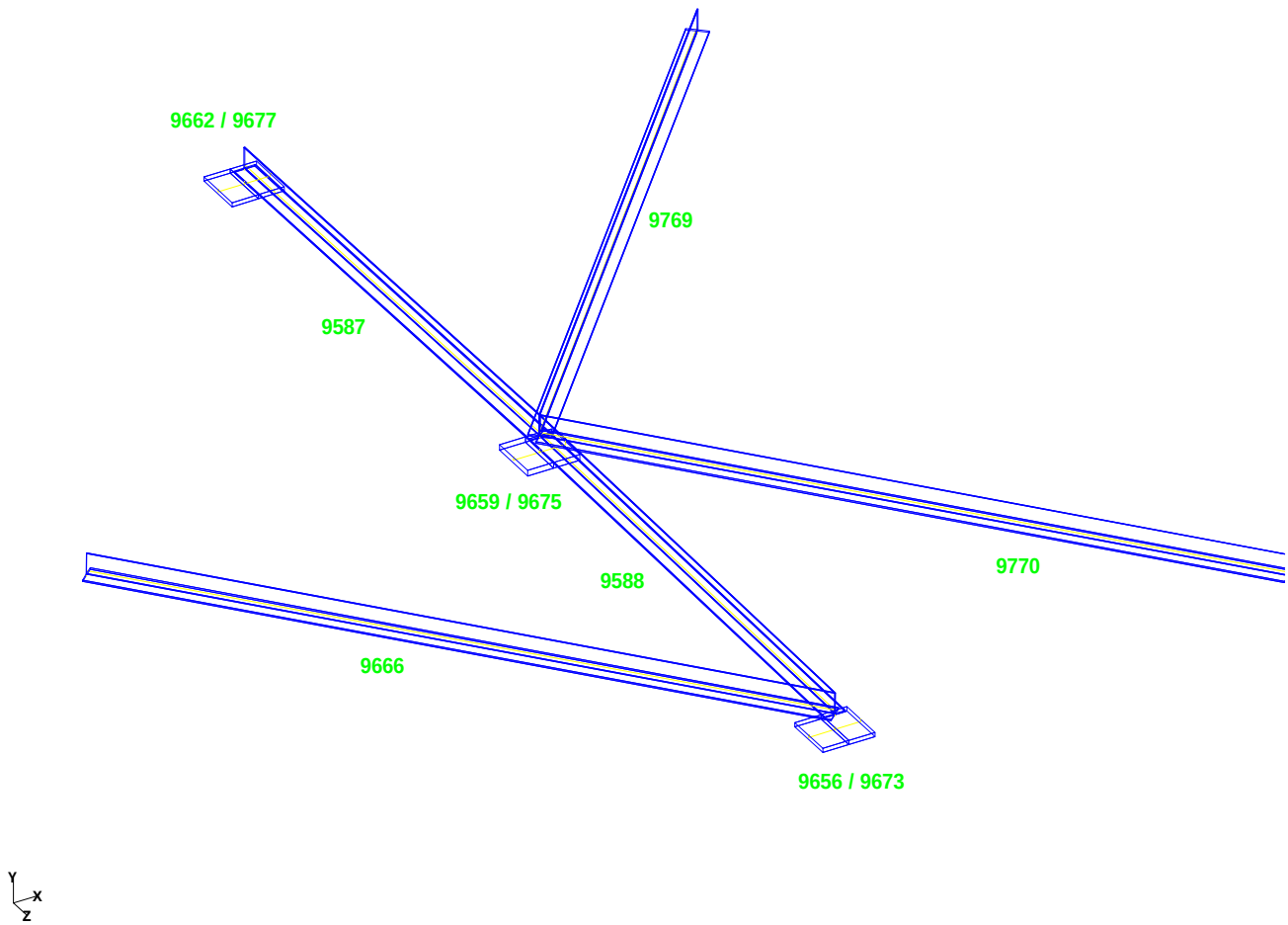

Figure 26: Bracing Members and Bottom Flange Members at Panel Point 28. (Girders not shown)

3.1.3 Dead Load

Original dead loads applied to the structure consist of the self-weight of the members and additional uniform loads applied to the girder flange members in unit S2A and the girder members in unit S3A. The uniform loads account for the components of the structure that have not been modeled (haunches, longitudinal stiffeners, intermediate transverse stiffeners, splice material, connection plates, railing, welds, bolts, and paint in S2A; deck, stringers, parapets, haunches, railing, bracing in unit S3A).

Total quantity of original dead load measured by reactions on piers 2, 3, 4, and 5 compare well between the current global model and the original design calculations. The total dead load reaction for the four piers (not including arch span dead load reaction on pier 2) from the original design calculations is 7235.6 kips. The total vertical dead load reaction for the global model is 6612.3 kips. The global model loads are therefore 91.4% of the original design calculation values. The initial design calculations included some conservative assumptions appropriate in the design phase that were not required for the evaluation of the existing bridge.

Both the dead load of the original design and the additional wearing surface dead load results for the bracing members and web stress at E-28 are summarized in Table 3.1.

Table 3.1 Calculated Dead Load Forces and Stress

Bracing Member	Dead Load
	Axial Force (kips)
East Transverse	5.6 (C)
West Transverse	6.1 (C)
East Diagonal	30.5 (T)
West Diagonal	30.1 (T)
Diagonal from E27 to F28	33.4 (T)
Web around the shelf plate	Longitudinal stress (ksi)
	15.2 (T)

3.1.4 Live Load: AASHTO HS20-44 Lane Loading

The AASHTO Standard Specification HS20-44 Lane Loading is applied to each of the three lanes. The lane loading consists of a uniform load of 640 lb/ft. (over a 10 ft width of each lane) acting where it increases the force effect and a concentrated load of 18 kips for flexure.

The results checked here correspond to the AASHTO loading for bending moment at the E-28 location. The uniform load is therefore applied over all of the outside two spans of S2A (pattern loading extended into S3A is neglected) with the interior span unloaded. The concentrated loads are each 18 kips and are applied at panel point 28, as illustrated in Figure 27. The concentrated load for the center lane is applied on the deck node directly over E-28. The concentrated load for the right (truck) lane is applied at the deck node over Stringer 7. The concentrated load for the left (passing) lane is applied at the deck node between Stringers 5 and 6. Each of the concentrated loads was applied at the deck node next to the center of the 10 foot loaded width in the direction of Girder E.

Each lane load is considered as its own load case and the various combinations of lane loads with multiple presence factors are made. There are a total of seven load cases. Only results for Load Case 7 (shown in Figure 28) are presented in the following table. Load Case 7 consists of all three lanes loaded with a 0.9 factor applied to all results.

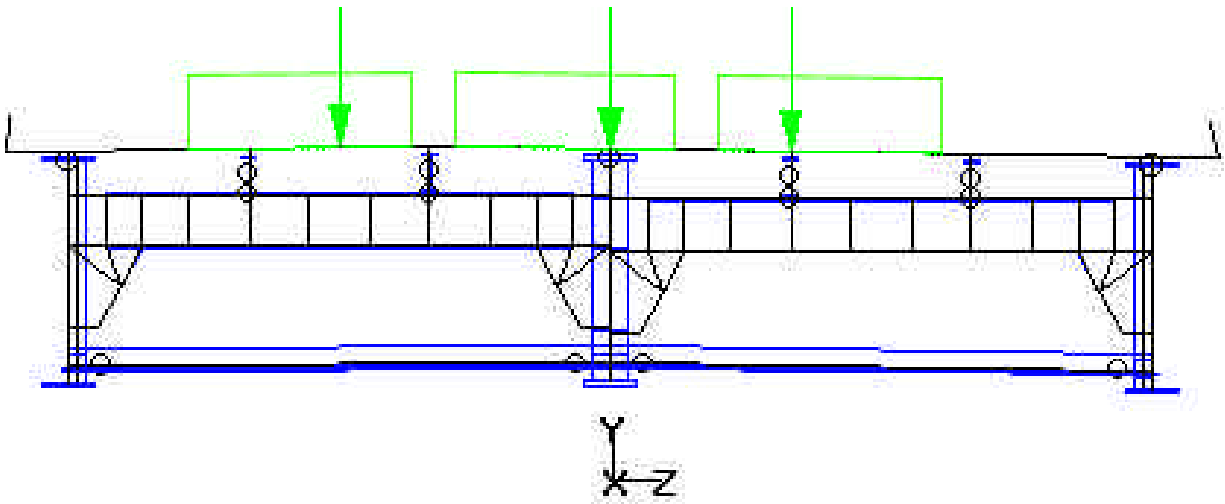

Figure 27: Cross Section View of Load Case 7

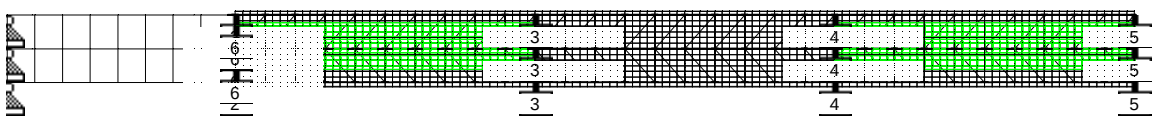

Figure 28: Plan View of Lane Loading for Load Case 7

A summary of results for AASHTO HS20-44 lane loading is provided in Table 3.2

Table 3.2: Load Case 7 - Lane Loading in All Three Lanes

Bracing Member	Design Live Load
	Axial Force (kips)
East Transverse	0.1 (C)
West Transverse	1.7 (C)
East Diagonal	10.5 (T)
West Diagonal	15.7 (T)
Diagonal from E27 to F28	14.9 (T)

Web around the shelf plate	Longitudinal stress (ksi)
	4.4 (T)

3.1.5 Live Load: 4 Axle Truck

The live load model used for the failure investigation is based upon the 4 axle vehicle configuration used for calibrating the weigh-in-motion study (see Section 3.4) on the Lincoln Avenue Bridge and in the load test of the Unit N2A approach section of the Hoan Bridge. The gross vehicle weight of the truck was 73.7 kips and 67.6 kips for the two tests respectively. The vehicles have been positioned to maximize web stress at E28 and were also centered in the east and center lanes to provide a match to the load test, as illustrated in Figure 29.

An influence surface for web stress at E-28 due to loads in the right and center lanes from Pier 3 to Pier 2 was determined. The influence surface shows the expected result that the peak result is obtained by placing a load directly over the point of interest. The influence surface indicates that loads placed to the west (toward Girder D) of E-28 have slightly higher coefficients around the point of interest than loads place east (toward Girder F). This meant that the single truck configuration was maximized by centering one wheel line over Girder E and placing the second wheel line in the corresponding position toward Girder D. The influence surface coefficients are higher in the direction of Pier 3 than in the direction of pier 2. This resulted in placing the heaviest (second) axle at E-28, as illustrated in Figure 30. For the two truck case in order to keep within the lane boundaries the second vehicle was placed to the east of the first vehicle (in the right lane). Shifting both vehicles from the position in Figure 29 toward Girder D so that the inside wheel line of the second truck was centered over Girder E would increase the web stresses slightly but the effect would be small and that positioning would not be within the existing lanes.

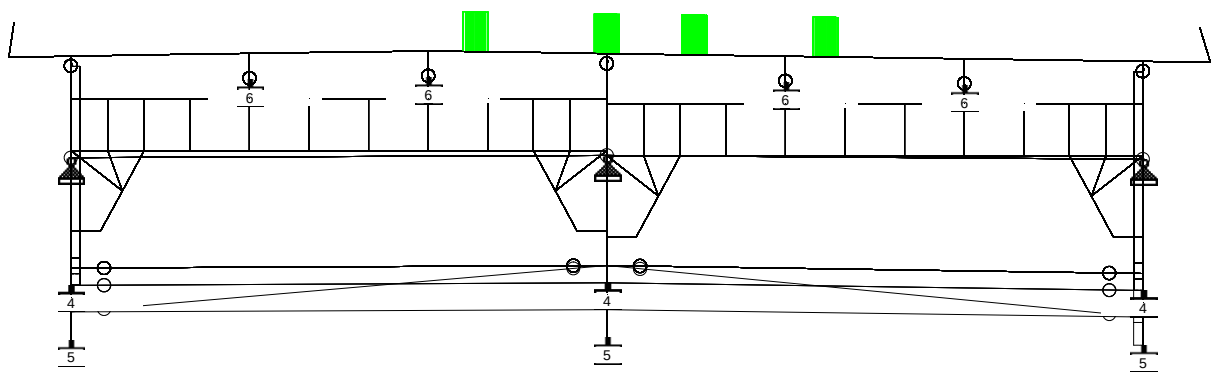

Figure 29: Transverse position of Loads for Two 4 Axle Vehicles to Maximize Center Girder Web Stress

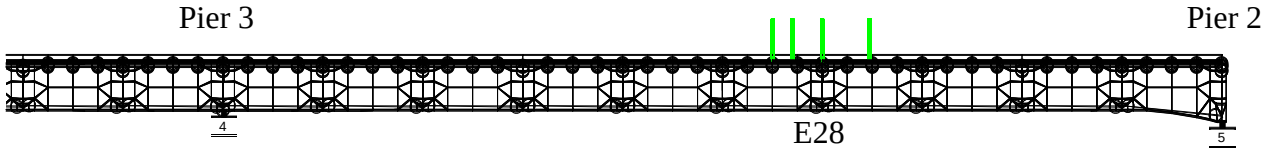

Figure 30: Longitudinal Position of Loads for 4 Axle Vehicles

Table 3.3 provides a comparison of global model to field test for live load (4 axle truck, GVW = 67.6 kips).

Table 3.3 Comparison of Measured and Calculated Stresses for Test Truck Girder Bottom Flange Stresses (ksi)

	3D Model	Load Test	Hand Calculation (Lever Rule)
	Truck in East Lane		
East Girder	1.46	1.16	1.11
Center Girder	1.31	1.20	2.15
West Girder	0.65	0.48	0
	Truck in Center Lane		
East Girder	0.85	0.58	0
Center Girder	1.40	1.22	2.64
West Girder	1.07	0.83	0.47

Table 3.4 provides the 4 axle truck live load results for failure analysis of E-28 (GVW = 73.7 kips).

Table 3.4 Estimated Live Load at Failure

	4 Axle in Center Lane	4 Axle in East Lane
Bracing Member	Axial Force (kips)	
East Transverse	0.8 (C)	3.6 (T)
West Transverse	1.6 (C)	1.8 (T)
East Diagonal	1.8 (T)	7.3 (T)
West Diagonal	5.3 (T)	0.2 (C)
Diagonal from E27 to F28	5.8 (T)	6.0 (T)

Web around the shelf plate	Longitudinal stress (ksi)	
	1.5 (T)	1.4 (T)

3.1.6 Wind Load

The global model shows that wind load is carried primarily by the concrete deck. The current bracing contributes mostly at the panels close to the piers where it helps to transfer the wind forces from the concrete deck down to the bearings, as illustrated in Figure 31. The maximum force in the bracing members under the wind loading is 22 kips and occurs in the diagonal members connected to the girders at the supports on the piers. The maximum stress due to wind alone in the girder flanges is 2 ksi. The following figure shows the relative magnitude of the wind force in the bracing members and girder bottom flanges along the length of the last span in unit S2A.

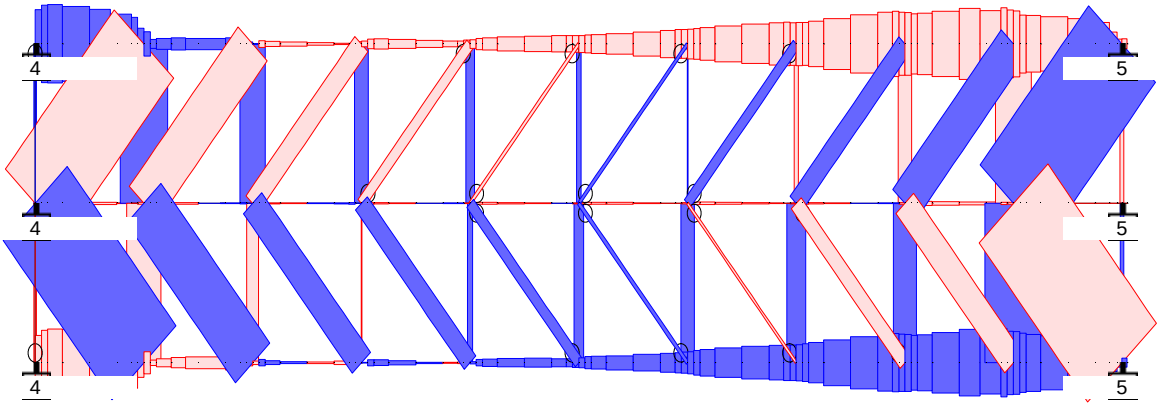

Figure 31: Wind Load Forces in Bracing Members and Girder Bottom Flanges Before Failure

3.1.7 Uniform Temperature Change

All of the same modeling assumptions are made for the uniform temperature change load case as for the vehicular live load with the following differences:

1. The model is run with two settings for the modulus of the concrete deck. The first case is the same as for the vehicular live load analysis. The second case uses a concrete modulus multiplied by 1/3 to account for creep.

2. The expansion joints at the cantilever overhang and at pier 2S are assumed to be able to accommodate the expansion at the ends. This assumption means that the only global longitudinal driver of temperature induced forces will be the longitudinal reactions generated at the piers. A second assumption that the bearings at Pier 2S are frozen has also been run.

The uniform temperature change results in the entire structure attempting to change in dimensions. Since the spans are continuous over a long distance this results in movements at the piers. Table 3.5 presents the bracing member forces and web stresses at E-28 due to the uniform temperature change.

Table 3.5: Calculated Forces and Stress Due to Temperature Change

Bracing Member	Axial Force (kips)
East Transverse	1.77 (C)
West Transverse	1.74 (C)
East Diagonal	1.04 (T)
West Diagonal	0.97 (T)
Diagonal from E27 to F28	1.00 (T)

Web around the shelf plate	Longitudinal stress (ksi)
	0.55 (T)

3.1.8 Temperature Gradient

The Hoan bridge site is subject to sudden drops in temperature brought on by weather fronts. A temperature gradient due to a 15 degree Fahrenheit decrease has been assumed. The sudden change causes a temperature change in the webs and bottom flanges of the structural steel. The top flanges and the concrete deck do not experience this sudden temperature change due to the large thermal mass of the deck. Unlike the uniform temperature change the temperature gradient does not result in a uniform expansion over the entire structure but instead results in bending. The pattern of the deflections are shown in Figures 32 and 33.

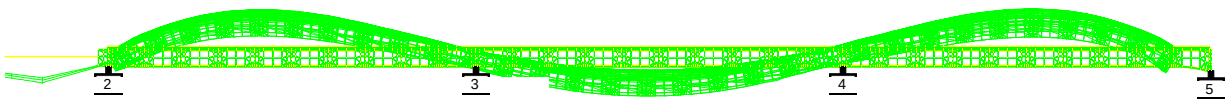

Figure 32: Temperature Gradient Deflections in Unit S2A

The configuration of the spans leads to higher temperature gradient induced stresses in the interior span than in the two end spans since both ends take on a curvature that accommodates some of the temperature induced strain while the center span is forced by the outside spans to take on the opposite curvature.

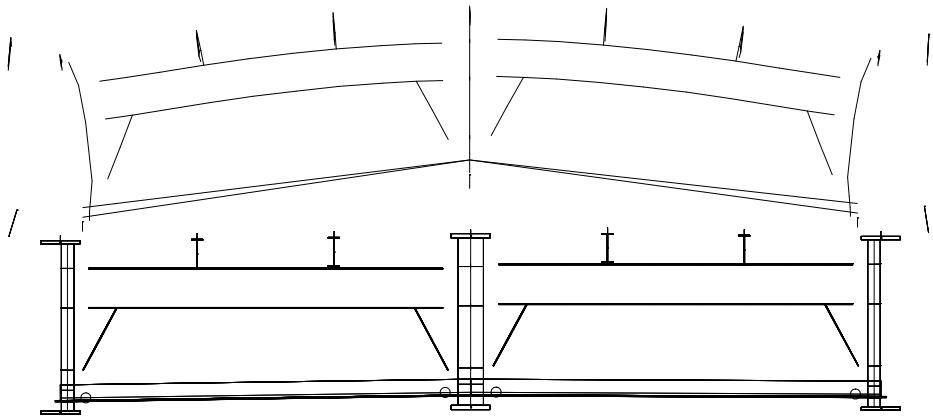

Figure 33: Deflected shape of the Cross Section at Panel Point 28

The deflected shape of the cross section in Figure 33 shows that a temperature gradient causes some distortion of the exterior girder webs but no distortion of the interior girder web. This is due to the mostly symmetric nature of the cross section and the fact that the temperature gradient is applied to all of the steel below the level of the top flanges.

The forces in the bracing members at panel point 28 and the longitudinal web stress are shown in Table 3.6.

Table 3.6: Calculated Forces and Stress Due to Temperature Gradient

Bracing Member	Axial Force (kips)
East Transverse	5.5 (C)
West Transverse	5.6 (C)
East Diagonal	2.5 (T)
West Diagonal	2.5 (T)
Diagonal from E27 to F28	2.1 (T)

Web around the shelf plate	Longitudinal stress (ksi)
	0.74 (T)

3.1.9 Bracing Removal

Removal of the bracing members and the shelf plate used to connect the bracing members to the web and transverse connection plate is necessary to remove the fracture prone detail. The negative impact of bracing removal must be considered in terms of the effect upon live load stresses and the wind load stresses.

Table 3.7 shows the bracing removal effect on design (HS20 Lane) live load stresses from 3D Model.

Table 3.7: Effect of Bracing Removal on Flange Stress

	Maximum Stress (ksi)		
	Existing Bracing	Bracing Removed	% Change
East (F)	3.7	3.4	- 8.1%
Center (E)	4.4	4.6	+ 4.5%
West (D)	4.1	4.3	+ 4.9%

The decrease in stresses for the east girder is due to the current lane configuration which places a 10 foot wide shoulder in the east. The modeling and placement of the loads reflect this current condition. If the lane striping is considered variable then the same result will apply to all of the girders. The increases are slightly higher for the 4 axle load configuration, however, the stress magnitude for that loading is much lower and therefore unimportant in terms of the girder capacities.

The maximum result of bracing removal is a 5 percent increase in girder flange stresses. Given the low magnitude of the live load stresses (around 4.5 ksi) the 5 percent increase is not critical.

Wind load forces are quickly transmitted into the deck slab for both with and without bracing conditions. The floorbeams with their large knee brace style support brackets are effective in transmitting the wind load up into the slab. The increases in flange and web stresses due to wind loads is minimal. The current bracing system does decrease the stresses in the web

and bearing stiffeners at the piers where the wind forces in the deck must be transmitted to the piers. Removing the bracing members would result in overstressing the web and bearing stiffeners at the piers under the code wind load. This means that strengthening of the end diaphragms, specifically in a manner that directly connects from deck to bottom flanges, would be required.

3.1.10 Summary Global Structural Analysis

- Analysis using a full three-dimensional model demonstrated that significant forces are imposed in the bracing members by the dead loads of the structure. The two diagonal bracing members framing into E-28 were found to have dead load tension forces of 30.1 and 30.5 kips. The transverse bracing members had 5.6 and 6.1 kips compression.

- Live loads produced small stresses in the girders and bracing members relative to the dead loads.

- Removal of the lateral bracing system had a very small impact on the bottom flange stresses. The four-axle load configuration which is most common resulted in the center girder flange stress increasing from 4.1 to 4.3 ksi.

- The global model verified that wind loads are transferred by the girder webs and transverse floorbeam connection plates into the concrete deck and then back down into the pier bearings. This occurred with or without the bracing members.

3.2 3-D FINITE ELEMENT STRESS ANALYSIS OF JOINT E-28

3.2.1 Model Description

A detailed three dimensional model of the joint assembly at panel point E-28 was constructed to study stress concentrations occurring at the detail. Twenty node solid elements were utilized to avoid any problems due to large stress gradients in the model. The model includes a section of the web, transverse connection plates, shelf plates, and all welds. Sections of the transverse lateral braces were also included to accurately model the stiffness of the connection between the shelf plates and transverse stiffener. The bracing members are only connected to the other plates in the model at the bolthole locations to simulate the flexibility of the connection. The mesh was refined in the web gap area to accurately capture the large stress concentration in this area. The model was created with FEMAP software and analyzed using the ABAQUS program operating on a UNIX based workstation.

Figure 34 shows a 3-dimensional view of the model with the hole in the west shelf plate. Note that the deflected shape is greatly exaggerated. The color contours show the magnitude of the stress in the X-direction along the axis of the girder.

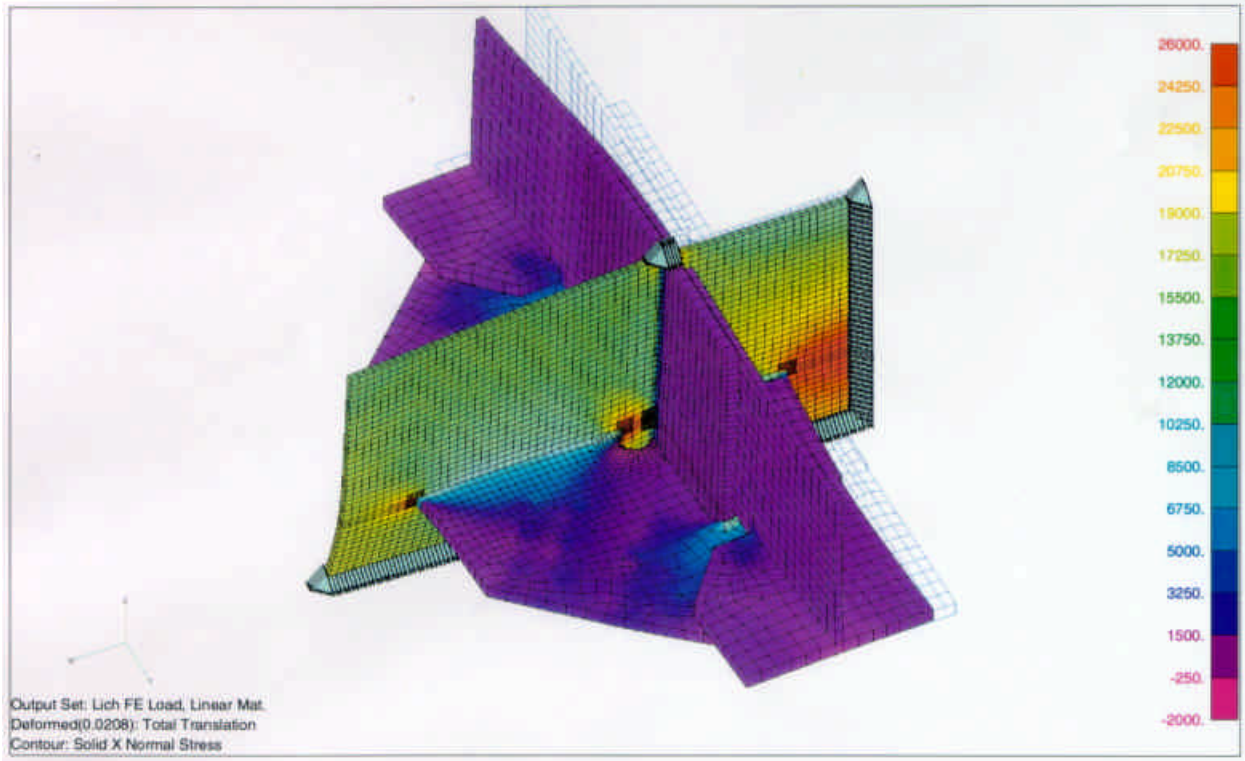

Figure 34: 3-D Solid Finite Element Model with Hole in Shelf Plate

The red areas clearly show stress concentrations that are occurring at the ends of the shelf plate and in the web gap areas. The size of the web plate is sufficient so the effect of stress concentrations is minimal at the edges of the plate.

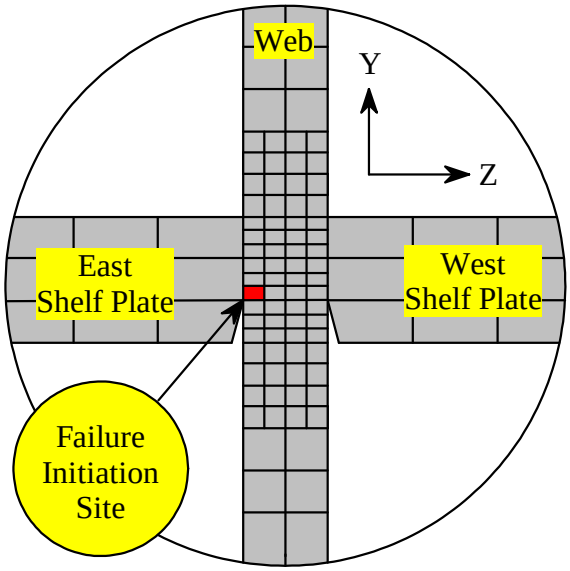

Figure 35: Section Through the F.E. Model Showing the Mesh Density and Location of the Failure Site

A refined mesh was used in the web gap area as shown in figure 35. There are four elements through the thickness of the ½ in. web plate in the vicinity of the web gap area. The bottom third of the shelf plate is not connected to the web to model the gap created by the partial penetration weld. Figure 35 also shows the direction of the Y and Z-axes used to define the stress components in the following sections. The X-direction represents the direction of normal bending stress in the girder web. The red square in figure 35 marks the element that corresponds to the failure initiation site identified by the fractographic investigation. The following stress plots all refer to elements with the same Y coordinate as the red square. All stress data points represent the average stress state at the center of an individual element. Therefore, the model is not capable of calculating the actual surface stress in the web. The elements on the surface of the web plate give the average stress state 1/16 in. away from the surface. Because of the large through-thickness stress gradient occurring in the web gap areas, the actual surface stress will be higher than those reported by the element average stress.

The model geometry was varied to study the significance of local conditions that were on the stress distribution in the web gap area. The following geometric variables were studied:

1. Symmetry of Web Gap. One model was run with the 1-1/2 in. shelf plate cutout perfectly centered on the floor beam connection plate. This resulted in the web gaps being equal on both sides of the connection plate and there was a 1/8 in. gap between the toe of the fillet weld on the floor beam connection plate and the termination of the partial penetration shelf plate weld. A second model was run with the shelf plate offset 1/8 in. to one side, thereby reducing the web gap to ¼ in. on the critical side causing the two welds to intersect. The shelf plate was observed to have this offset at the locations E-28 and F-28 where failure occurred in the bridge.

2. Effect of Shelf Plate Hole. A 2 in. hole was added to the shelf plate on the west side of the connection to recreate the exact geometric condition that existed at E-28.

Two different levels of analysis were performed for each geometric model. An initial run was made assuming linear elastic material. The analysis was then repeated using a non-linear material model that captures plastic deformation in the joint. A true stress-strain curve was developed for the web plate based on the tests reported in section 2.1.2. The F.E. program uses this curve to determine the point where yielding occurs in the model. Because stress is no longer proportional to strain in non-linear plastic analysis, an iterative solution scheme is required to obtain the final results. The point where yielding occurs is determined by the Von Mises Yield Criterion as follows:

$$\sqrt{\frac{(s_1 - s_2)^2 + (s_2 - s_3)^2 + (s_3 - s_1)^2}{2}} \geq s_{yp} \qquad \textbf{(3.1)}$$

Where σ_1, σ_2, and σ_3 are the principal stress components in three directions and σ_{yp} is the uniaxial yield strength of the web. This yield criterion accounts for the effect of the triaxial stress state when determining yielding. Under a pure triaxial stress state ($\sigma_1 = \sigma_2 = \sigma_3$), yielding cannot occur and stress can increase to levels many times greater than σ_{yp} .

3.2.2 Loading Applied

The loads applied to the model are determined from the 3-D structural analysis described in section 3.1. A bending stress distribution is applied to one edge of the web plate while the other edge is restrained. Axial loads in the lateral braces are also applied to the model. For the transverse laterals, the axial force is applied as a uniform stress distribution over the total cross section. The diagonal lateral members were not included in the model, so the diagonal lateral loads were applied to the shelf plate at the locations corresponding to the boltholes. An equal share of the force was distributed to each bolt location.

The loads applied to the model are obtained by adding the total effect of dead and live loads calculated from analysis. The dead load numbers were obtained from the structural self-weight including effects of the wearing surface. The exact live load at the time of failure is not known, but it is reported that two trucks were seen simultaneously on the bridge. A reasonable assumption of live load was chosen to be 2 times the loads caused by one of the WI-73 kip trucks in the right lane. Because the live load is only about 13% of the total load, minor differences in truck weight and lane position are assumed insignificant. Figure 36 shows the magnitude and direction of the loads applied to the E-28 joint assembly. The loading does not include any thermally induced loading or any forces that are locked in the structure during fabrication. In addition, no attempt has been made to introduce residual stress into the model due to cooling of weldments.

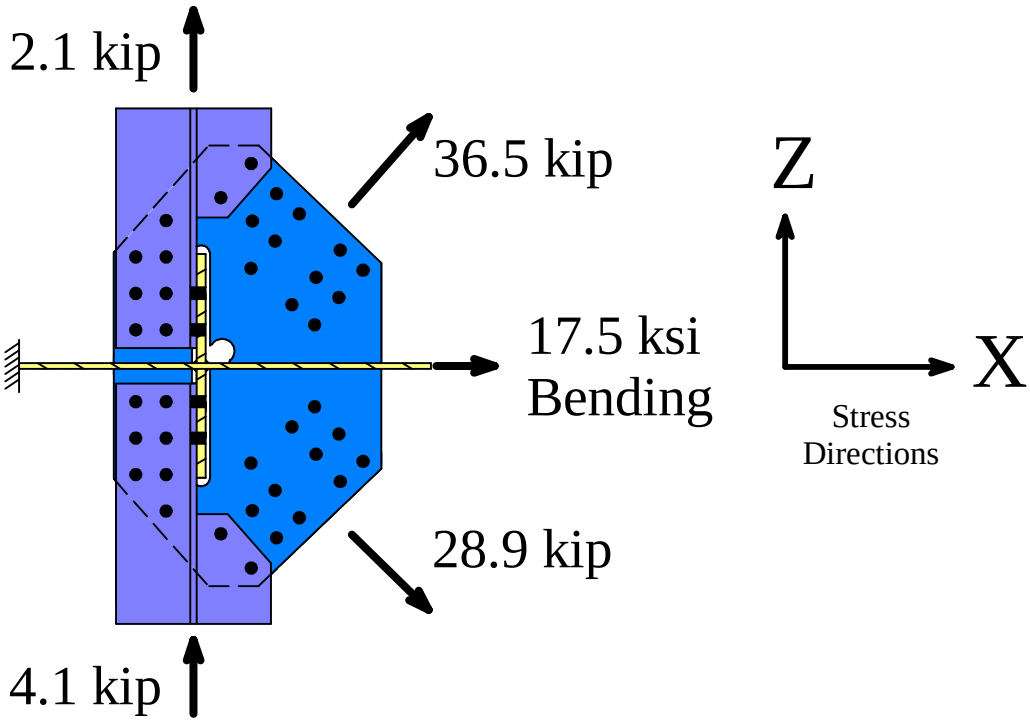

Figure 36: Total Load (DL + LL) Applied for Stress Analysis

3.2.3 Stress Concentration Due to Shelf Plate Detail

Figure 37 shows the variation in bending stress (σ_x) that occurs along the length of the shelf plate detail due to the applied loading shown in figure 36. There is no hole in the shelf plate and the web gap is ¼ in., simulating the as-built conditions in the bridge. The horizontal axis shows the location relative to the center of the floor beam connection plate with positive numbers increasing in the north direction. The horizontal blue line at 17.5 ksi shows the applied bending stress that would exist without the geometric stress concentrations and the effect of the lateral brace forces.

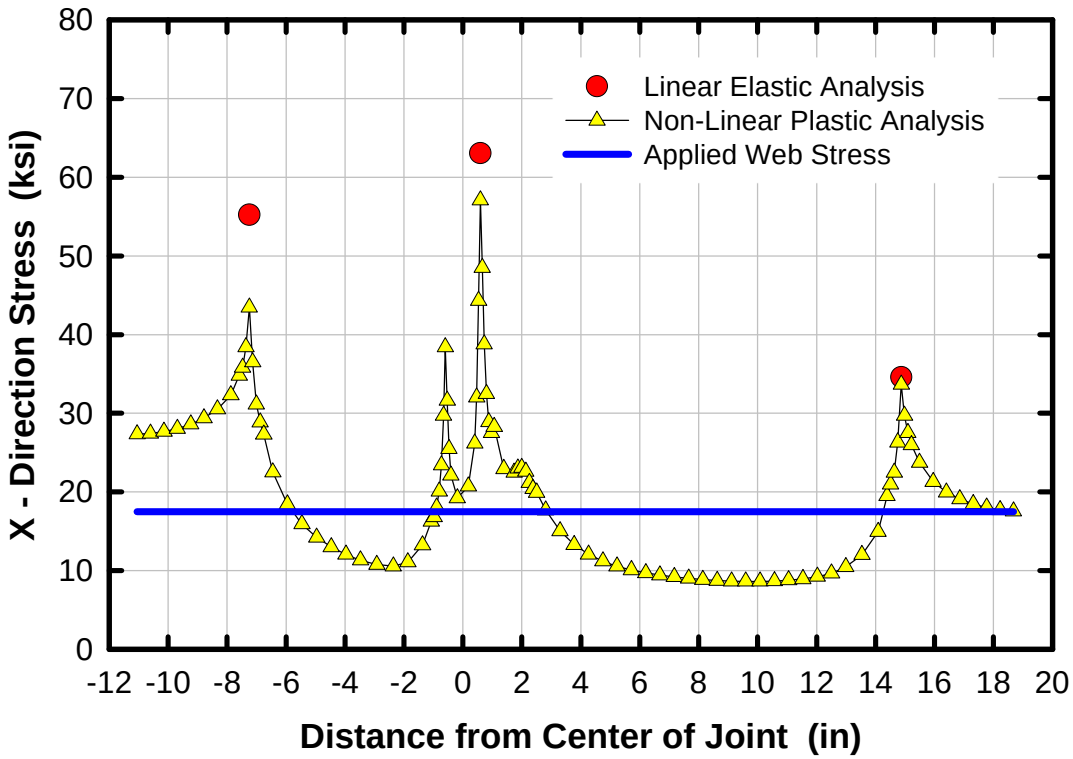

Figure 37: Variation in Bending Stress (s_x) in the Web Along the Length of the Shelf Plate

The stress concentration occurring at the two shelf plate ends and in the web gap area is clearly visible in this figure. The yellow symbols show the results of the non-linear analysis where yielding is allowed to occur. For comparison, the red symbols show the peak elastic stress concentration that was calculated without yielding. At the south end of the shelf plate (X = -7.2 in.), yielding caused a 27 percent reduction in the stress from 55.2 ksi down to 43.5 ksi. This shows the effect of yielding when the web plate has a relatively low level of triaxial constraint. At the failure location (X = 0.59 in.), there is clearly less yielding and the initial stress concentration of 63 ksi is only reduced 10 percent to 57.1 ksi. This shows that an increased triaxiality in the web gap area is preventing yielding.

The effect of the forces in the lateral braces can be seen at the south end of the plot (X = -11 in.). On the north end (X = 19 in.) the stress converges to the applied bending stress level at about 4 in. past the end of the shelf plate. However at the south end, the stress is elevated. This elevation in stress is the result of the forces in the lateral bracing system. The asymmetric "K" pattern of the lateral bracing requires an additional axial stress in the girder to satisfy equilibrium in the joint assembly. This effect can help explain why several fatigue cracks were found at this end of the shelf plate at other locations in the structure.

3.2.4 Effect of Fabrication Tolerance

Figures 37 and 38 show the stress distribution through the thickness of the web in the gap area. The horizontal axis gives the through-thickness location Z relative to the center of the web with positive numbers indicating the west side of the girder. Similar to figure 37, the red symbols show the results of the linear elastic analysis while the yellow symbols include the effect of yielding. All three components of principal stress are plotted to illustrate the effect of triaxiality. The maximum principal stress component σ_1 is the critical stress that will cause fracture initiation. In these figures, the directions of the principal stress components (1-2-3) correspond closely to the directions of the global coordinate system (x-y-z). As mentioned previously, the stress results are calculated at the center of the elements so the peak stress at the surface of the web will be higher and must be estimated by extrapolation.

The result of the model with the symmetric web gap (3/8 in. – 3/8 in.) is shown in figure 37. Under elastic conditions, there is a large elevation in the σ_1 stress component toward the surface of the web, but this decreases toward the middle of the plate. Yielding allows stress relaxation to occur and the σ_1 stress component becomes relatively constant through the web thickness. The σ_3 stress component is low in the middle of the web resulting in a biaxial stress state. Toward the surfaces, σ_3 increases changing the stress state to a more triaxial condition. This triaxiality is the reason the maximum principal stress is still well above the yield strength of the material, even after yielding occurs.

Figure 38 shows the model with the offset web gap (1/4 in. – 1/2 in.). The reduced gap causes an increase in the σ_3 stress component towards the surface of the web indicating an increase in the amount of triaxiality. This increased triaxiality causes about a 13% increase in the maximum principal stress compared to the symmetric web gap. Table 3.8 shows a summary of the effect of decreasing the web gap for the west surface of the web at Z = 0.1875 in.

Table 3.8 Effect of Fabrication Tolerance on Principal Stress in the Web Gap (Z = 0.1875)

Non-linear Principal Stress Component	Symmetric Web Gap (3/8 in. – 3/8 in.)	Offset Web Gap (1/4 in. – 1/2 in.)	Change Due to Offset
σ_1 (ksi)	57.4	64.9	+13 %
σ_2 (ksi)	26.3	32.9	+25 %
σ_3 (ksi)	20.6	30.6	+49 %

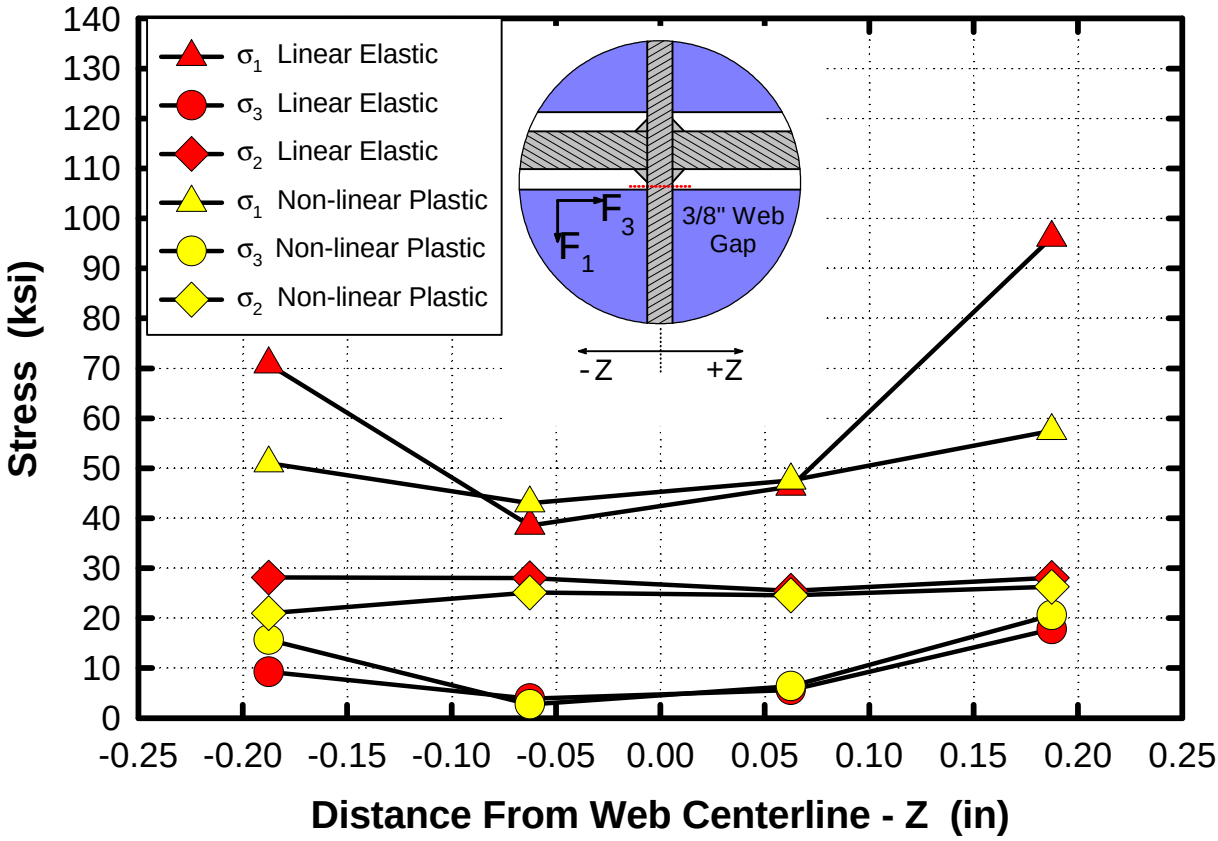

Figure 38: Variation in Principal Stress Through the Web Thickness with the Symmetric Web Gap

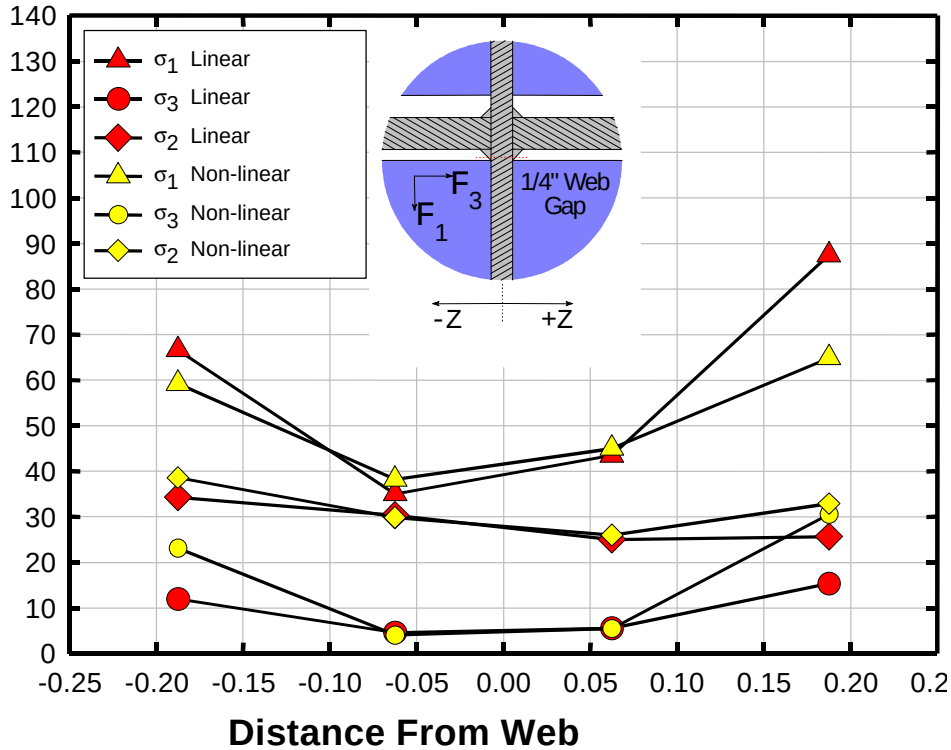

Figure 39: Variation in Principal Stress Through the Web Thickness with the Offset Web Gap

3.2.5 Effect of Shelf Plate Hole

The model with the offset web gap was modified to introduce a 2 in. diameter hole in the shelf plate on the west side of the connection. This simulates as closely as possible the geometry present at the failure location in the bridge. Results in figure 40 can be compared to figure 39 to show the effect of adding the hole. On the west side at Z = 0.1875, there is almost a total elimination in triaxiality resulting in a sharp decrease in the maximum principal stress. On the east side, however, there is an increase in triaxiality resulting in an 7 % increase in the maximum principal stress compared to the model without the hole. Table 3.9 summarizes this effect for the east surface of the web at Z = -0.1875.

Because the 2 in. hole is only present in one side of the shelf plate connection, the principal stress axes are no longer in the same direction as the global coordinate system. As shown in the inset in figure 39, the axis of maximum principal stress is rotated about 23 degrees relative to the global x axis. This correlates with observations of the fracture initiation site at location E-28. The fracture plane in the web gap was oriented approximately perpendicular to the $\sigma\sigma_1$ axis shown in figure 40.

Table 3.9 Effect of 2 in. Shelf Plate Hole on Principal Stress in the Web Gap (Z = -0.1875)

Non-linear Principal Stress Component	Offset Web Gap (1/4 in. – 1/2 in.) Without Hole	Offset Web Gap (1/4 in. – 1/2 in.) With Hole	Change Due to Hole
σ_1 (ksi)	59.2	63.1	+7 %
σ_2 (ksi)	38.6	32.0	-17 %
σ_3 (ksi)	23.1	28.1	+22 %

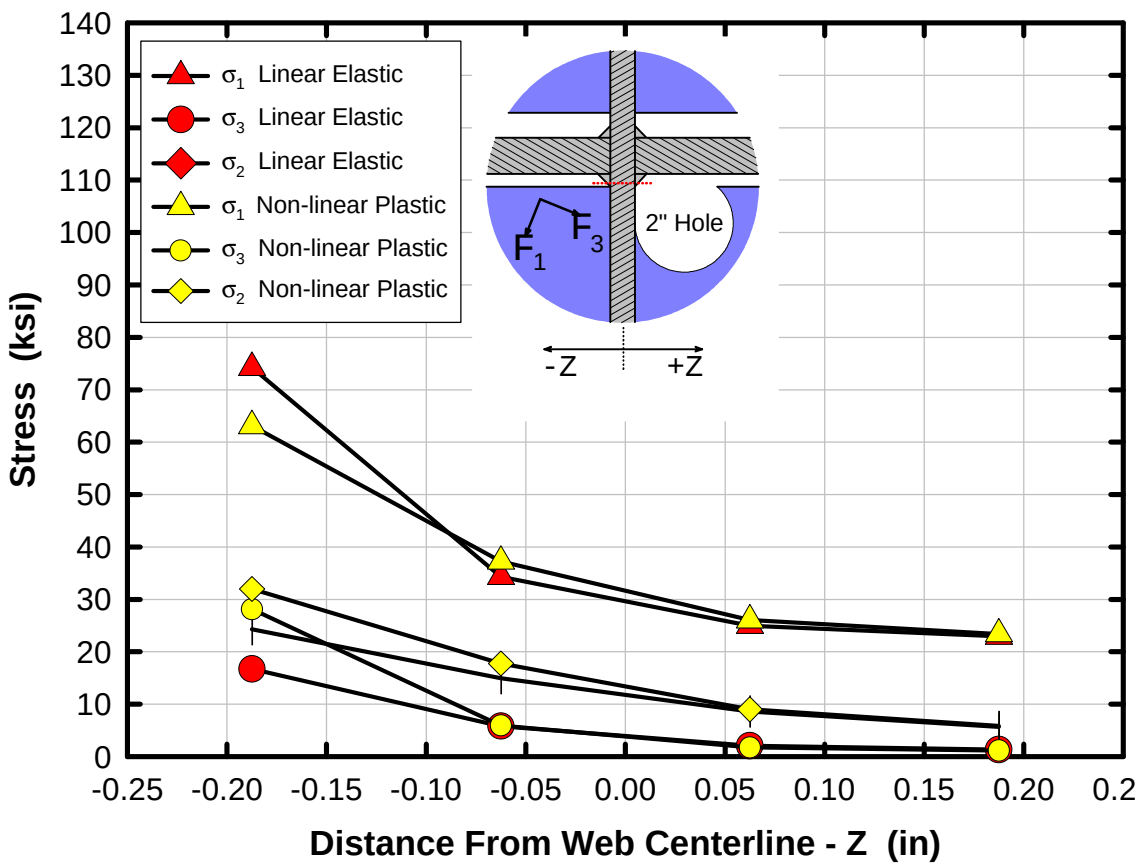

Figure 40: Variation in Principal Stress Through the Web Thickness with a 2 in. Hole in the West Shelf Plate

3.2.6 Effect of Lateral Bracing Forces

The model with the symmetric web gap was run with and without the lateral acing forces shown in Figure 36. Both models had the same applied bending stress of 17.5 ksi. The non-linear plastic model was not run for the case without the bracing force, therefore only elastic analysis is used as the basis for comparison. The results, shown in figure 41, show a significant increase in stress concentration in the web gap and at the south end (X = -7.5) of the shelf plate. The change in the 3-dimensional stress state in the web gap is shown in table 3.10. The stress components in the x and y direction both increase, but there is little change in the Z direction.

The increase in stress concentration in Figure 41 is primarily due to a rigid twisting of the joint assembly due to the asymmetric nature of the lateral brace forces. The stress pattern shows there is very little out-of-plane distortion occurring in the web gap area.

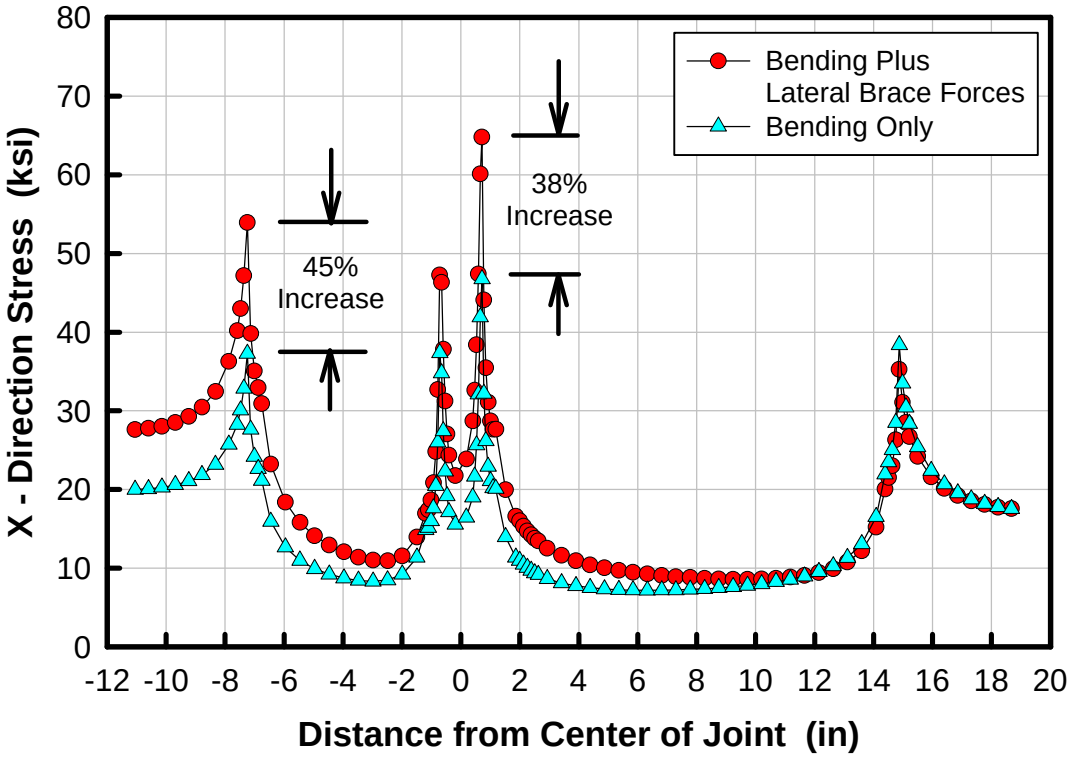

Figure 41: Change in Elastic Bending Stress (s_x) in the Web Due to Lateral Brace Forces

Table 3.10 Change in Elastic Stress State Due to Forces on the Lateral Bracing

Stress Component	Bending Only (ksi)	Bending Plus Lateral Brace Forces (ksi)	Change
σ_x	46.7	64.8	+ 38 %
σ_y	24.5	33.5	+ 37 %
σ_z	9.5	9.9	+ 4 %

3.2.7 Calculation of Triaxiality

The Von Mises yield criteria, shown in Equation 3.1, is used to predict when yielding will occur under triaxial conditions. The ratios of the three principal stress components in the finite element model can be used to calculate a triaxiality factor that can be used in fracture analysis. Knowing the ratio of the three principal stresses, a triaxiality factor can be calculated as:

$$T_r = \sqrt{\frac{1}{\left(1+\left(\frac{s_2}{s_1}\right)^2+\left(\frac{s_3}{s_1}\right)^2-\left(\frac{s_2}{s_1}\right)-\left(\frac{s_3}{s_1}\right)-\left(\frac{s_2}{s_1}\right)\left(\frac{s_3}{s_1}\right)\right)}} \tag{3.2}$$

Therefore, first yielding in the web gap area would not be expected to occur until:

$$s_1 \geq T_r\left(s_{yp}\right) \tag{3.3}$$

Results of the model with the hole show that T_r = 1.36 can be expected based on the linear elastic analysis. Therefore, first yield is expected to occur when the maximum principal stress is equal to 1.36 σ_{yp}.

Beyond first yield, there is an increase in triaxiality during plastic flow. The results of the non-linear F.E. model show that T_r = 1.95 can be expected in areas where yielding occurs. This is consistent with the constant volume flow rule of plasticity theory where Poisson's ratio increases to < = 0.5 after yielding.

3.2.8 Summary – Local Stress Analysis

- The stresses calculated by local stress analysis should only be used as a conservative general indicator of conditions occurring in the web gap. Actual local stress magnitudes may increase significantly with a finer F.E. mesh and the addition of residual stress. The results are useful, however to show effects of geometry change and triaxiality.

- Significant elastic stress concentrations exist at the ends of the shelf plates and in the web gap area. Without triaxial constraint, yielding occurs and relaxes the local stress level and there is no decrease in structural capacity. These concentrations do have an effect on fatigue performance, but this is accounted for in the AASHTO fatigue design provisions.

- The location where the highest stress and constraint occur in the finite element model corresponds exactly with the failure initiation site found by the fractographic analysis at

E-28. The direction of the maximum principal stress is also oriented perpendicular to the observed fracture plane at this area.

- The size of the web gap has a significant effect on the level of plastic constraint. Elastic triaxiality exists for both the symmetric and offset web gaps, but the restraint to plastic flow increases in the offset case. Therefore, the case where the web gap is reduced and the welds intersect creates a higher constraint condition than the case where there is a gap between the welds. The reduced gap was observed at all three details at floor beam 28.

- Elastic stress results indicate that triaxiality will prevent yielding until the stress exceeds about 1.36 times the yield strength of the material. Beyond yield, the triaxiality increases due to constraint of plastic flow. Under high plastic constraint, local stress levels can easily reach levels 2 to 3 times the yield strength.

- The 2 in. retrofit hole in the west shelf plate reduced the stress concentration and constraint on the side of the web with the hole, but increased the stress concentration on the opposite side by about 7% compared to the joint without the hole. Because plastic constraint was high in both cases, the presence of the hole has only a minor effect on the fracture vulnerability of the joint at E-28.

- Tensile forces in the lower lateral bracing cause an increase in stress concentration at the shelf plate ends, but have only a minor effect in the web gap area. There is no significant evidence of out-of-plane web gap distortion due to forces on the lateral braces.

- Although a model was not run for this case, the results suggest that drilling a 2 in. retrofit hole symmetrically in the shelf plates on both sides of the web would have eliminated the constraint in the web gap and significantly reduced the vulnerability to fracture.

3.3 LOAD TESTING

Load testing of the south span in unit N2A was performed from 3/1/2001 to 3/3/2001.

Testing on 3/1/2001 was of the bridge in its original condition. The south span of unit N2A is almost a mirror image of the failed span (unit S2A). The primary difference between the two units is that the individual span lengths in N2A are 213 feet instead of the 217 feet spans in unit S2A.

Testing on 3/2/2001 consisted of reading the gages before, during, and after unbolting the bracing member connections from first E5 and then from the rest of the center girders (E) in the span.

Testing on 3/3/2001 was of the bridge in a condition simulating the retrofit removal of the bracing members.

A more detailed description of the 3-D modeling and load testing is provided in Ref. 7.

3.3.1 Strain Gage Details

The strain gages are divided into three types. For each type a description of the type of location, the number of gages for one of those location, the number of locations, and the combined number of gages are listed.

1) 1/4" gage-length welded gages:

Girder top flanges	(1 x 3)	=	3 gages
Girder bottom flanges	(2 x 3)	=	6 gages
Floor beam bottom flange	(3 x 1)	=	3 gages
transverse bracings	(3 x 3)	=	9 gages
diagonal bracings	(2 x 3)	=	6 gages
interior shelf plate	(2 x 1)	=	2 gages
Total		=	29 gages

2) 1/8" gage-length bonded gages:

exterior girder webs	(2 x 2)	=	4 gages
interior gider web	(3 x 1)	=	3 gages
Total		=	7 gages

3) 10-element bonded strip gages:

exterior girder webs	(1 x 2)	=	2 gages

The location of each group of gages listed in this set of results is shown on the figure on the next page. Each location has various strain gages at the section .

● GIRDER GAGES:
2 ON THE BOTTOM FLANGE, 1 ON THE TOP FLANGE, 2 ON THE WEB (END OF SHELF PLATE).
STRIP GAGES ON FASCIA GIRDERS.
GAGE ON WEB ABOVE SHELF PLATE AND 2 GAGES ON SHELF PLATE ON INTERIOR GIRDER.

○ LATERAL BRACING GAGES:
2 ON THE BOTTOM FLANGE.
1 ON VERTICAL LEGS (TRANS. BRACING ONLY)

⊕ FLOORBEAM GAGES:
3 ON THE BOTTOM FLANGE
(ENDS NEXT TO BRACKETS AND MIDSPAN)

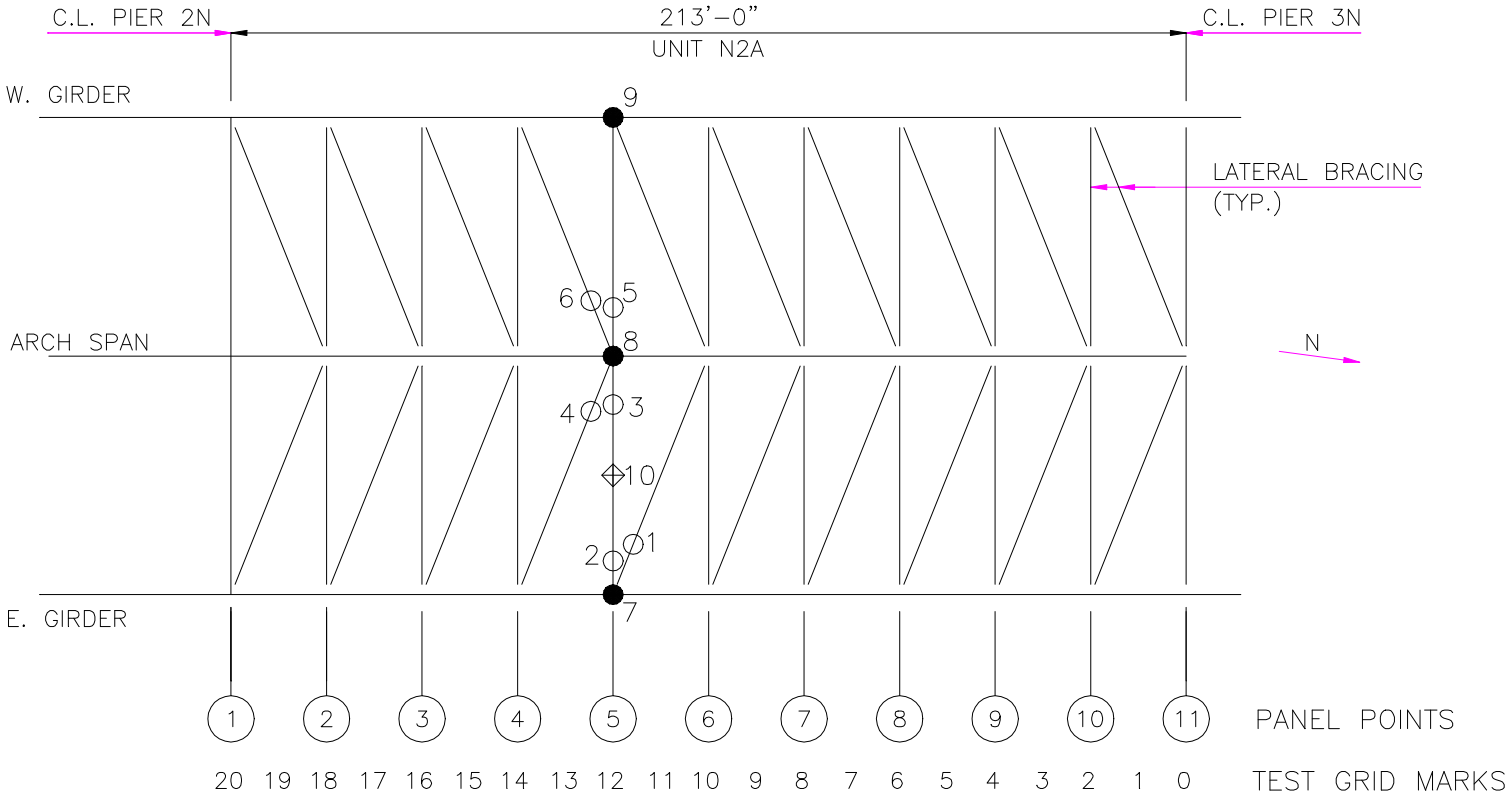

Gages on the bracing members (locations 1-6) are each 4 inches from the end of the shelf plate and are centered through the width of the plate section they are attached to. The transverse bracing members (locations 2,3,5) have 3 gages (2 on flange and 1 on web) at each location. The diagonal bracing members (1,4,6) have 2 gages (on the flange) at each location. The photograph on the left shows the gage setup on east bay bracing connected to the center girder.

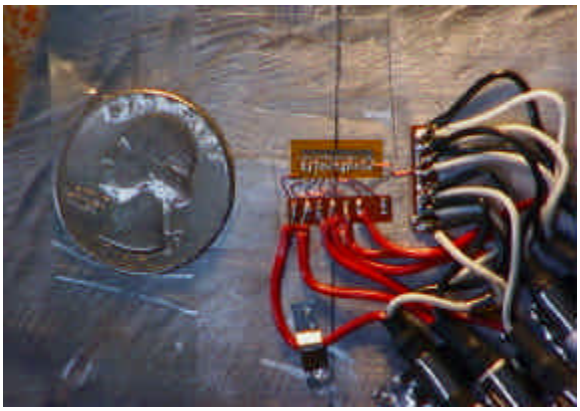

The exterior girder (fascia) sections (7 and 9) have 2 gages on the bottom of the bottom flange, 1 gage on the bottom of the top flange, 2 gages on the interior side of the web (one at the north and south ends of the shelf plate, shown in photograph below on right) and a strip gage (shown in photograph above on right) centered on the intersection of the transverse connection plate and the shelf plate on the outside of the web. The interior girder section (8) has 2 gages on the bottom of the bottom flange (shown in the photograph below on the left), 1 gage on the bottom of the top flange, and 3 gages on the web (one at the north and south ends of the shelf plate and one over the shelf plate close to the gap in the shelf plate on the south side of the transverse connection plate).

The east bay floorbeam has three gages on the bottom flange (shown in the photograph below).

Figure 43: Photo's of Strain Gage Installation

3.3.2 Test Truck Load Cases for 3/1/2001 and 3/3/2001

LL1 Truck in Right Lane (Crawl)

LL2 Truck in Center Lane (Crawl)

LL3 Truck in Left Lane (Crawl)

IM Truck in Center Lane (40MPH)

Each of the static truck passes (LL1, LL2, LL3) was performed 3 times on each of the two days. Static tests consisted of zeroing the gages, positioning the test truck with its front axle over pier 3N (panel point 11, grid mark 0), and moving the truck from grid mark to grid mark, recording data at each mark. The grid mark spacing corresponds to half the floorbeam spacing. The grid mark spacing is also very close to the distance from the front axle of the test vehicle to the second axle. The second axle is the heavy axle of the truck and the maximum positive moment effect is produced with that axle over the location of interest. Panel point 5 is the instrumented cross section of unit N2A, it corresponds to grid mark 12 in the test plan. The maximum moments in the girders occur with the truck at grid mark 13 which places the heavy axle over panel point 5.

Due to problems with reading the strip gages only one individual gage out of the set on each strip gages was recorded during each pass of the truck. Three individual gages were selected on each strip gage and these one of each of the three gages was read during each truck pass. This resulted in having data for each truck lane location and distance along the span for each of the 6 individual strip gage channels. All other gages were read during all tests. This results in having three data points for each truck lane location and distance along the span. In order to capture more information from the strip gages two additional load cases were added on 3/1/2001 to the original plan. These load cases consisted of placing the truck at grid mark 13 in first the east and then the west lanes and manually switching the connected gage on the strip gages.

The dynamic load case (IM) consisted of the test truck running at approximately 40 mph over the span from south to north (opposite direction of the static tests).

In addition to the vehicular load testing and the removal of bracing members the gages were set to record for extended periods of time without supervision to capture strains caused by the temperature changes and wind.

The area of the bracing members (ST 12WF50) are 14.55 in^2, strong axis I is 176.5 in^4, weak axis I is 111.7 in^4.

3.3.3 Gage Results

Strain readings were collected in a time history format for each position of the truck in static tests and for the duration of the test for the dynamic and unbolting load cases. The time history data for the static tests was then reduced to single values at each grid point by taking the statistical mode of the last 10 seconds of data. Strain values have been converted into stresses in the tables as being more intuitive and representative of the capacity of the steel. The conversion assumes that the strain in the direction perpendicular to the gage is zero, this is accurate for the readings on the girder flanges and floorbeam flanges but may introduce some error into locations such as the girder webs and bracing members.

The readings on the top flange of the girders are uniformly low for all load positions. This indicates that full composite action is present between the girders and the deck.

The following table summarizes the peak values for any of the static tests on each girder in the bottom flange, web (except for the strip locations), and the floorbeams.

Maximum Truck Load Stresses (ksi) from all Passes and Lanes

		Bolted Condition	Un-Bolted Condition	% Difference
Flange	East Girder	1.2	1.5	+ 25%
	Center Girder	1.4	1.7	+ 20%
	West Girder	1.7	2.0	+ 17%
Web	East Girder	4.9	3.5	-29%
	Center Girder	2.9	2.6	-10%
	West Girder	4.1	4.4	+ 7%
Floorbeam	East	1.2	1.7	+ 50%
	Center	2.3	3.2	+ 38%
	West	-1.5	0.6	-60%

The maximum stresses for any static live load positions shown in the previous table indicate that the girder flange stresses and stresses in the floorbeam are low. The stresses in the web of the girders are taken from the two gages positioned at the ends of the shelf plates. These values show a stress concentration in the web for both the case where the bracing members are connected and for when they have been unbolted. This indicates that fatigue cracking at the ends of the shelf plates would be a problem even with the bracing members removed if the shelf plate itself is not also taken out.

The ratio of the peak dynamic strains to the peak static strains are 1.25 in the girder flanges, 1.28 in the girder web gages north and south of the shelf plates, 1.00 in the bracing members, and 1.00 in the floorbeam.

The following table presents the results from the load test in terms of locations 1 to 9 given on the gage layout diagram. The average value from the three passes of truck loading are given (as opposed to the peaks in the previous table). As with the previous table the web gages show a stress magnification over the flange stresses and the strip gages stresses show even greater increases in peak stress.

Summary of Maximum Stresses
(average of three passes)

Gage Location	Member Description		Truck Loading Maximum Stresses (ksi) Bracing Attached	Bracing Removed
1	**Diagonal Bracing** connecting East Girder (F5) to Center Girder (E6) Gages near East Girder		0.58	
2	**Transverse Bracing** connecting East Girder (F5) to Center Girder (E5) Gages near East Girder		0.87	
3	**Transverse Bracing** connecting East Girder (F5) to Center Girder (E5) Gages near Center Girder		-0.96	
4	**Diagonal Bracing** connecting East Girder (F4) to Center Girder (E5) Gages near Center Girder		1.05	
5	**Transverse Bracing** connecting West Girder (D5) to Center Girder (E5) Gages near Center Girder		0.58	
6	**Diagonal Bracing** connecting West Girder (D4) to Center Girder (E5) Gages near Center Girder		0.48	
7	**East Girder** (F5)	Flange	1.16	1.26
		Web	3.96	3.29
		Strip	-8.11	
8	**Center Girder** (E5)	Flange	1.35	1.54
		Web	2.61	2.42
9	**West Girder** (D5)	Flange	1.65	1.94
		Web	3.77	3.68
		Strip	-6.38	

The testing on 3/1/2001 included an additional test where the live load was placed in the grid 13 location and the strip gage channels were manually cycled. The results of this test are shown in the following table. Both the raw microstrain values and converted stress values are given in this table.

Strip Gage Strains

microstrain (ksi)

Gage is centered on Transverse Connection Plate and Shelf Plate intersection.

Loading	East Girder			West Girder		
Truck in East Lane Heavy Axle @ PP5	Strip S	-280	(- 8.1)	Strip N	-220	(- 6.4)
	Strip	128	(3.7)	Strip	-210	(- 6.1)
	Strip	160	(4.6)	Strip	-110	(- 3.2)
	Strip	130	(3.8)	Strip	-32	(- .9)
	Strip	90	(2.6)	Strip	60	(1.7)
	Strip N	130	(3.8)	Strip S	20	(0.6)
Truck in West Lane Heavy Axle @ PP5	Strip S	60	(1.7)	Strip N	200	(5.8)
	Strip	5	(0.1)	Strip	180	(5.2)
	Strip	0	(0.0)	Strip	170	(4.9)
	Strip	-10	(- 0.3)	Strip	0	(0.0)
	Strip	-70	(- 02.)	Strip	180	(5.2)

The results of the load testing correlate well with the results of the 3D model after modifications to match the composite action observed in the test.

The strip gage values provide a measure that can be used in the verification of the local model being used by FHWA.

3.4 WEIGH-IN-MOTION

The objective of the study was to measure truck weights using the weigh-in-motion (WIM) equipment. The WIM system operates on a bridge that serves as a scale. The structure is instrumented, strains are measured, and from the strain data, truck axle loads and gross vehicle weight (GVW) are calculated. The process is repeated for all vehicles passing on the bridge.

East Lincoln Avenue Viaduct, close to the Hoan Bridge, was selected as it carries most of the detour truck traffic from the Hoan Bridge. The eastbound entering span was selected for the instrumentation. The installation of the testing equipment was performed from February 11, 2001 to February 13, 200provided by W1. The truck weights were measured from February 13, 2001 to February 15, 2001. The measurement was taken by the project team from the University of Michigan, Ann Arbor. The equipment used was provided by University of Michigan. The calibration truck was Wisconsin Department of Transportation.

Summary of WIM Study Findings

- The gross vehicle weight (GVW) data include all trucks with a GVW of 5 kips and greater.
- The maximum gross vehicle weight observed was 109.7 kips.
- The mean value of the GVW of all trucks was 62.5 kips with a standard deviation of 27 kips.
- The mean value of the GVW of top 20% of trucks was 89.7 Kips
- Approximate ADTT = 1000

Figure 44: Typical Truck Traffic

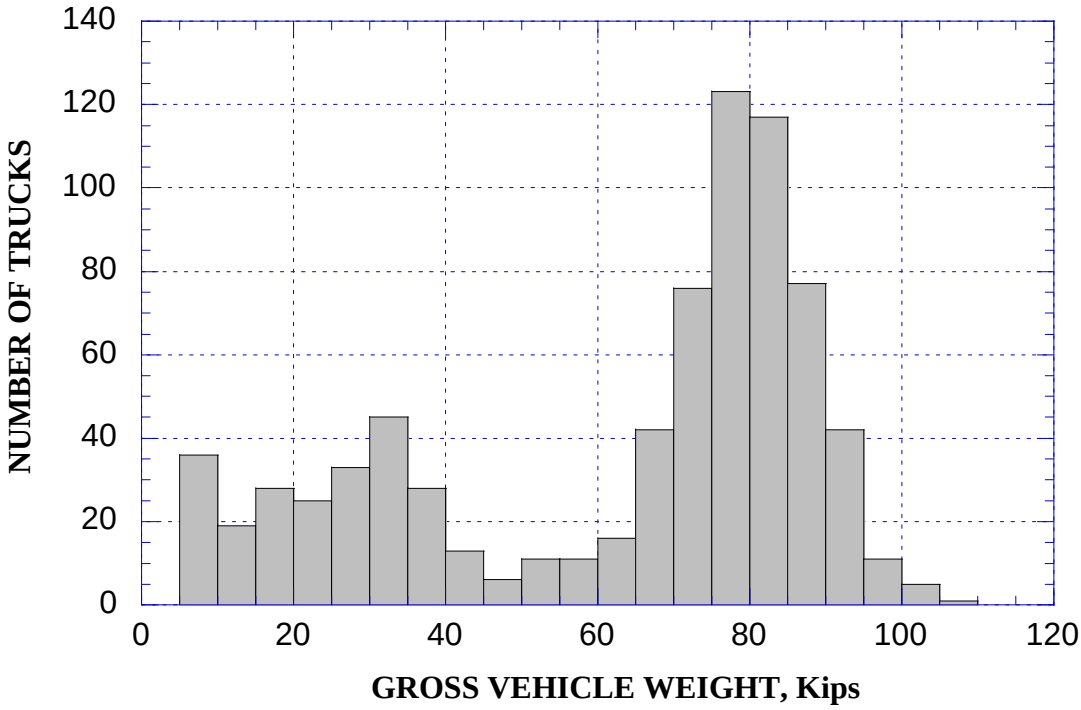

Fig. 45: Gross Vehicle Weight Distribution for All Trucks

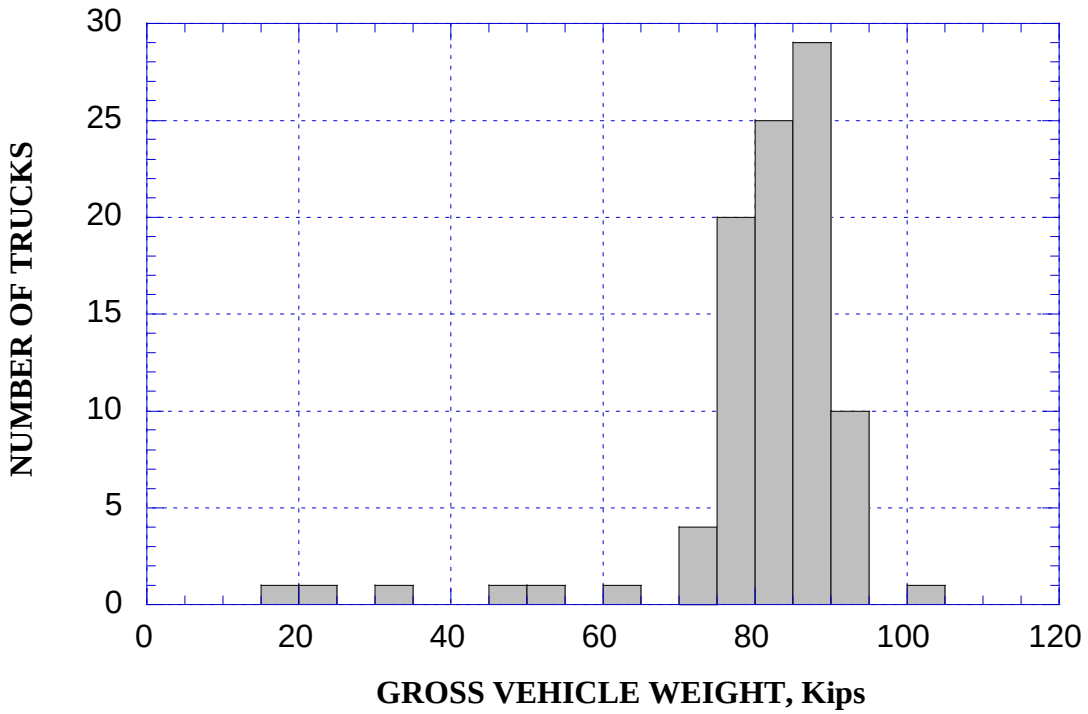

Figure 46: Gross Vehicle Weight Distribution, 6 Axle Trucks

Axle Loads

The maximum axle weight observed was 47.6 kips. The mean value of observed axle loads were 14.6 kips with a standard deviation of 5.6 kips.

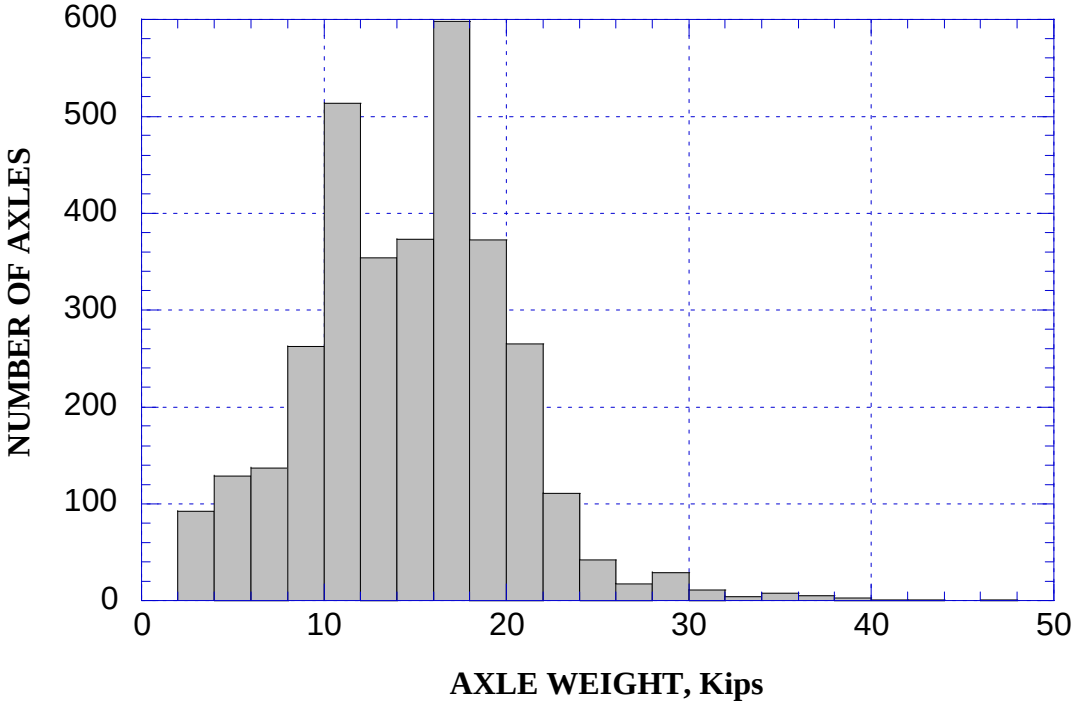

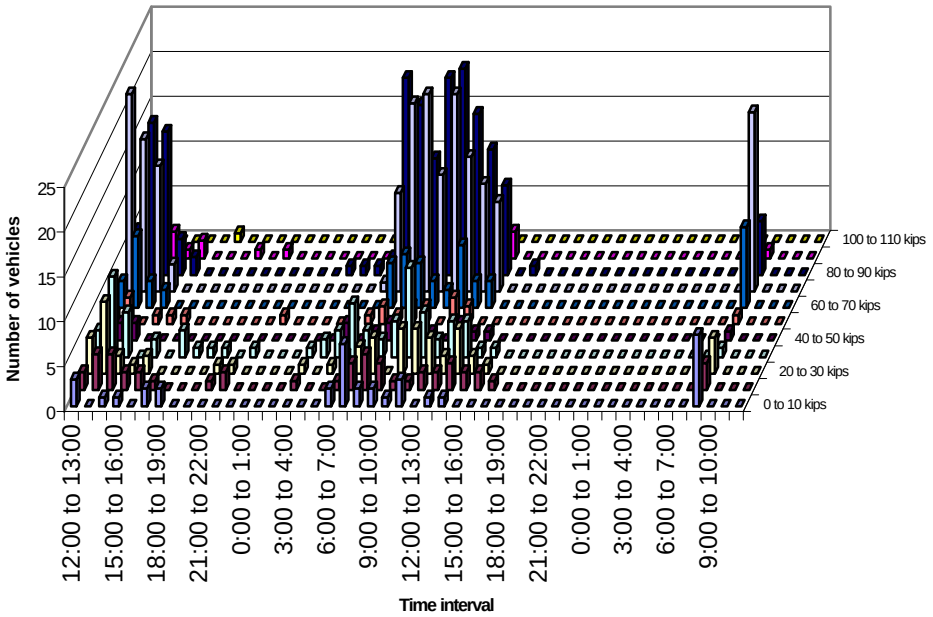

Figure 47: Axle Weight Distribution and Frequency Histogram, All Trucks

Time History

Table 3.11 Truck Traffic for Different Time Periods

Time Period		Gross Vehicle Weight (kips)										
		0 to 10	10 to 20	20 to 30	30 to 40	40 to 50	50 to 60	60 to 70	70 to 80	80 to 90	90 to 100	100 to 110
2/13/01 PM	12:00 to 1:00	3	2	4	3	2	1	3	22	5	1	0
	1:00 to 2:00	0	4	8	9	2	3	8	17	17	2	0
	2:00 to 3:00	1	4	2	5	2	0	3	14	16	3	0
	3:00 to 4:00	1	2	1	0	0	1	2	3	4	1	0
	4:00 to 5:00	0	2	2	2	0	1	0	0	2	2	0
	5:00 to 6:00	2	1	0	0	0	1	0	0	0	0	0
	6:00 to 7:00	2	0	0	3	0	0	0	0	0	0	1
	7:00 to 8:00	0	0	0	1	0	0	0	0	0	0	0
	8:00 to 9:00	0	0	0	1	0	0	0	0	0	1	0
	9:00 to 10:00	0	1	1	1	0	0	0	0	0	0	0
	10:00 to 11:00	0	2	1	0	0	0	0	0	0	1	0
	11:00 to 12:00	0	0	0	1	0	0	0	0	0	0	0
2/14/01 AM	12:00 to 1:00	0	0	0	0	0	1	0	0	0	0	0
	1:00 to 2:00	0	0	0	0	0	0	0	0	0	0	0
	2:00 to 3:00	0	0	0	0	0	0	0	0	0	0	0
	3:00 to 4:00	0	1	1	1	0	0	0	0	1	0	0
	4:00 to 5:00	0	0	0	2	0	0	0	0	1	0	0
	5:00 to 6:00	0	0	1	3	2	0	0	0	1	0	0
	6:00 to 7:00	2	1	2	6	0	1	0	1	2	1	0
	7:00 to 8:00	7	3	3	3	1	2	5	11	22	7	1
	8:00 to 9:00	2	4	4	2	2	1	6	21	19	5	0
	9:00 to 10:00	2	3	0	4	1	2	5	22	13	2	0
	10:00 to 11:00	1	1	5	10	1	2	3	13	22	6	0
	11:00 to 12:00	3	1	5	5	1	0	2	22	23	9	2
2:14/01 PM	12:00 to 1:00	0	2	4	2	0	3	7	15	18	4	1
	1:00 to 2:00	1	2	2	4	2	2	3	12	14	4	1
	2:00 to 3:00	1	3	5	4	1	0	3	10	10	3	0
	3:00 to 4:00	0	2	2	1	1	0	0	0	0	0	0
	4:00 to 5:00	0	2	1	1	0	0	0	0	1	0	0
	5:00 to 6:00	0	1	0	0	0	0	0	0	0	0	0
	6:00 to 7:00	0	0	0	0	0	0	0	0	0	0	0
	7:00 to 8:00	0	0	0	0	0	0	0	0	0	0	0
	8:00 to 9:00	0	0	0	0	0	0	0	0	0	0	0
	9:00 to 10:00	0	0	0	0	0	0	0	0	0	0	0
	10:00 to 11:00	0	0	0	0	0	0	0	0	0	0	0
	11:00 to 12:00	0	0	0	0	0	0	0	0	0	0	0
2/15/01 AM	12:00 to 1:00	0	0	0	0	0	0	0	0	0	0	0
	1:00 to 2:00	0	0	0	0	0	0	0	0	0	0	0
	2:00 to 3:00	0	0	0	0	0	0	0	0	0	0	0
	3:00 to 4:00	0	0	0	0	0	0	0	0	0	0	0
	4:00 to 5:00	0	0	0	0	0	0	0	0	0	0	0
	5:00 to 6:00	0	0	0	0	0	0	0	0	0	0	0
	6:00 to 7:00	0	0	0	0	0	0	0	0	0	0	0
	7:00 to 8:00	0	0	0	0	0	0	0	0	0	0	0
	8:00 to 9:00	8	3	4	1	1	1	9	20	6	1	0
	9:00 to 10:00	0	0	0	0	0	0	0	0	0	0	0
	10:00 to 11:00	0	0	0	0	0	0	0	0	0	0	0
	11:00 to 12:00	0	0	0	0	0	0	0	0	0	0	0

4. FRACTOGRAPHIC AND METALLOGRAPHIC EXAMINATION

4.1 FRACTURE SAMPLES

Selected areas of the fractures in Girders D, E, and F at P.P. 28 were examined both visually and microscopically using a scanning electron microscope (SEM) to characterize the fractures and gain additional information about the fracture mechanism(s). Examination focused primarily at the fracture origin areas in the girder web at the shelf plate weld terminating adjacent to the vertical connection plate in each of the girders. Similar areas in other girders where cracks were also found were also examined (Girder D P.P. 9 and Girder B P.P. 26). Several other areas of interest in the failed girders were also examined in detail. These included the crack arrest area at the bottom flange of Girder D, the web crack bifurcation near the fracture origin in Girder E, the shelf plate fracture in Girder E in the hole repair area, and the transverse brace fracture in Girder E located at the cope of the WT12 X 55 section.

In general, all of the fracture surfaces examined were covered with a layer of corrosion of varying thickness resulting from exposure to the weather and salt prior to removal from the structure. Evidence of abraded areas on some crack surfaces which occurred during demolition of the span was also observed. Prior to examining, the as-received fractures were documented photographically. Areas for detailed examination were extracted by saw-cutting followed by ultrasonic cleaning in Alconox detergent to remove as much of the corrosion product as possible. Removal of the corrosion layer to examine the underlying fracture surface was moderately successful, however, the tenacity of the corrosion product in some areas, often at fracture origin areas, frequently prevented microscopic information from being obtained in these areas.

4.2. FRACTOGRAPHIC EXAMINATION

4.2.1 Girder E P.P. 28 - Fracture Origin

The fracture origin in Girder E had been traced to the girder web at the lateral bracing connection where the shelf plate partial penetration weld joint to the web terminated adjacent to the vertical connection plate. The shelf plate which pulled out from the girder web during failure is shown in Figure 48. The opposing side of the web fracture with the vertical connection plate still attached is shown in Figure 49. Cleavage chevron marks on the web fracture surface were observed to point from both directions to the shelf plate weld termination thus confirming this area to be the fracture origin. The web fracture origin at the weld termination is shown in Figure 50 and clearly shows a fan-shaped cleavage chevron pattern emanating from the vicinity of the weld root lack of fusion. A similar radial cleavage chevron pattern at the shelf plate weld termination was also observed on both sides of the fracture coinciding with a origin point in the vicinity of the weld root lack-of-fusion.

Visual examination of the fracture origin area of both sides of the fracture showed no indication of a base metal or weld defect in this area. Microscopic examination with the SEM (see Figure 51) showed the presence of cleavage fracture as close to the fracture origin as could be discerned. Corrosion product not removed during cleaning of the surfaces obscured some areas at the origin, however, no indication of stable crack growth processes such as fatigue or ductile tearing was observed in corrosion free areas within 1mm of the origin. Without the presence of a macroscopic defect cleavage likely initiated from a microscopic discontinuity which may have sharpened by fatigue over time. Fracture initiation from a microscopic defect is not inconsistent with the high triaxial stress state believed to exist in this area.

Figure 48: Shelf Plate With Web Fracture Origin at the Weld Termination. (Girder E P.P. 28)

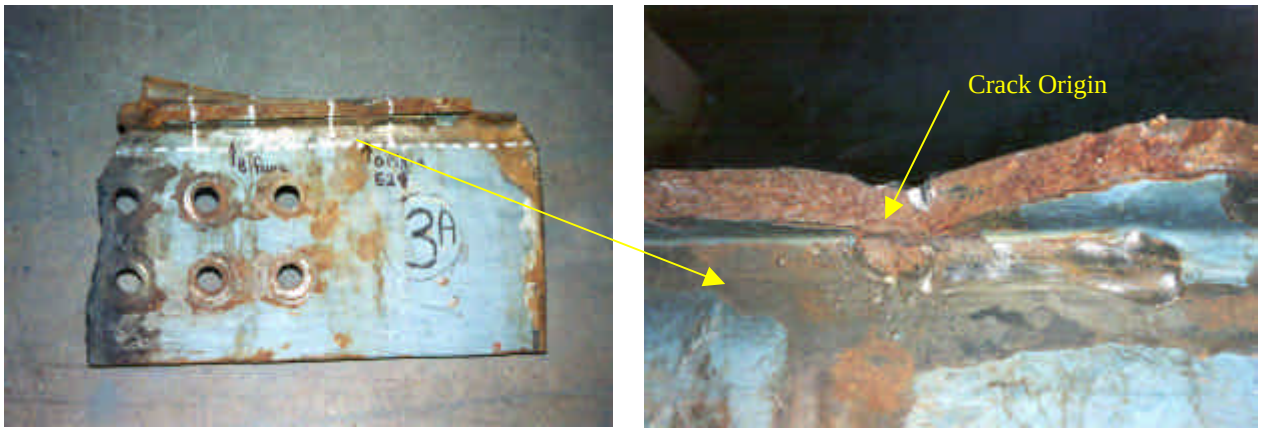

Figure 49: Opposing Web Crack Surface at the Fracture Origin Attached to the Vertical Connection Plate (Girder E P.P. 28)

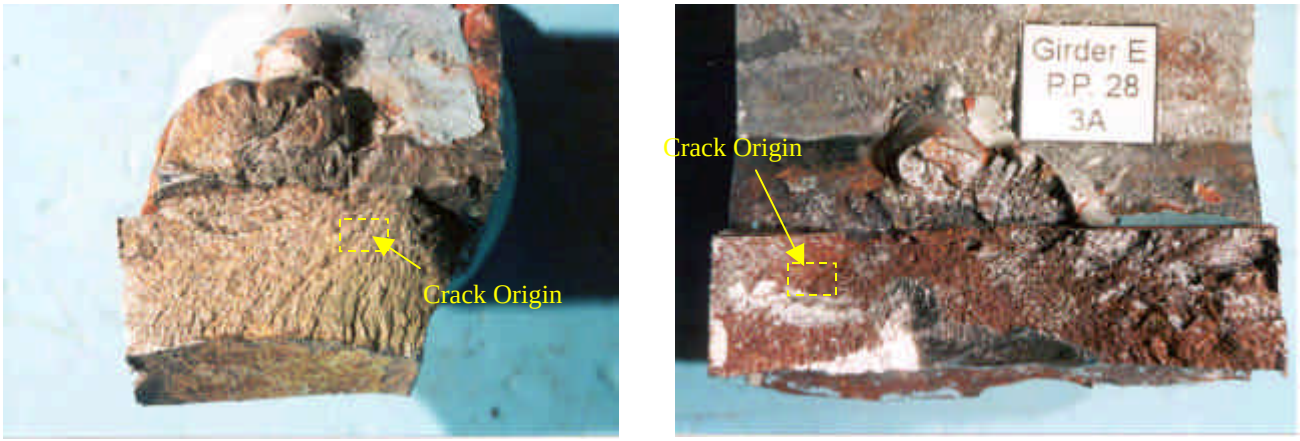

Figure 50: Opposing Crack Surfaces Showing the Web Fracture Origin Near the Weld Root (Girder E P.P. 28) (Enlarged View of Boxed Area Shown Below)

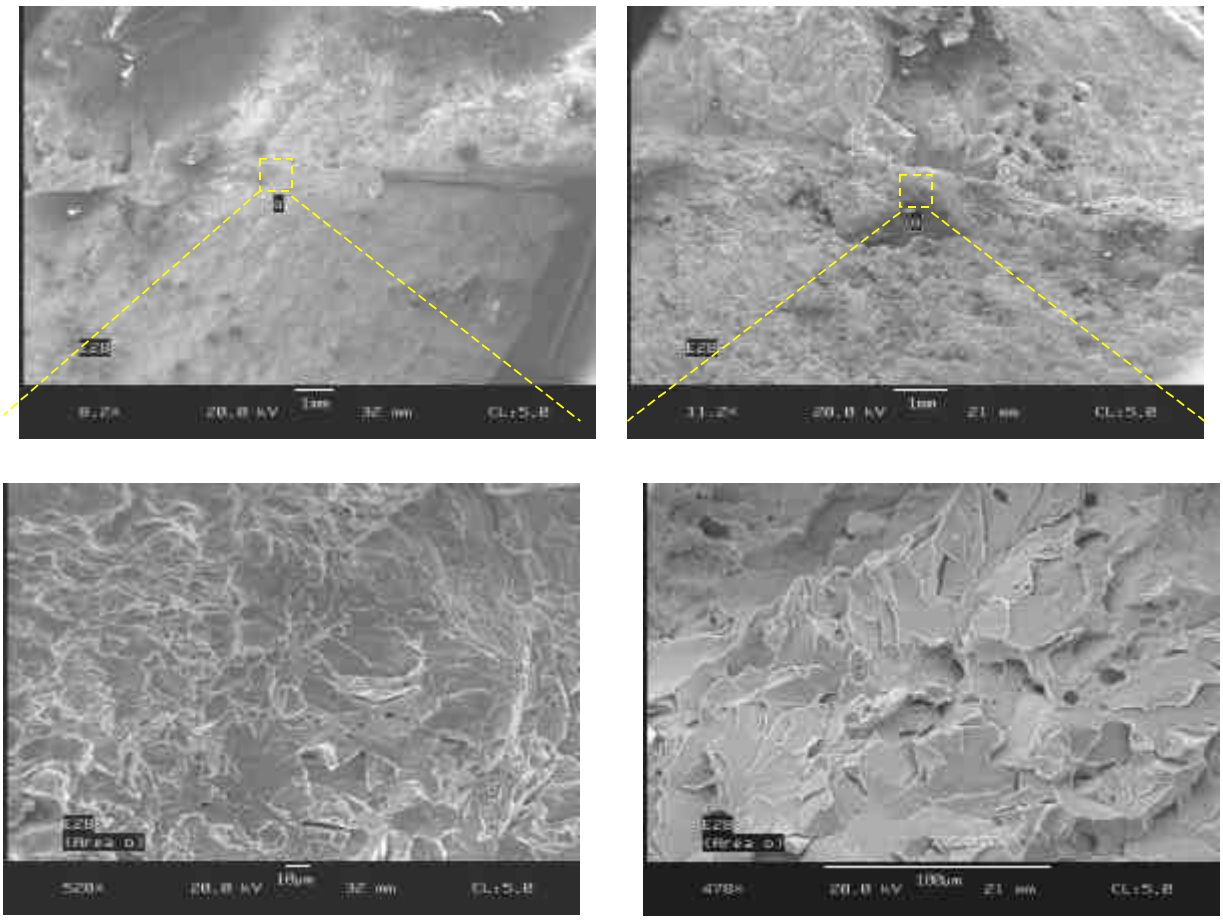

Figure 51: SEM Micrographs Obtained From Opposing Sides of the Fracture Showing Cleavage at the Fracture Origin (Girder E P.P. 28

4.2.2 Girder D P.P. 28 - Fracture Origin

The fracture origin in Girder D traced back to the same location as in Girder E. The section of Girder D containing the crack origin at the shelf plate weld joint termination is shown in Figure 52. The opposing crack surfaces at the fracture origin removed from the corner of the shelf plate and from the web along the vertical connection plate as for Girder E are shown in Figure 53. In this case two distinct cleavage fracture origins are seen occurring in offset planes resulting in the stepped appearance of the fracture. One origin appeared to be in the shelf plate weld near the weld root although a well defined origin as determined by cleavage chevron markings were not as clear as in Girder E. The other origin was clearly traceable to the shelf plate weld toe area. In both cases no visual indication of an initiating defect was observed in the origin areas. A weld metal gas pore about 1mm in diameter was observed in one of the origin areas, however, it is not certain if this defect was associated with the cleavage initiation.

Figure 52: Section of Girder D P.P. 28 Containing the Crack Origin Area and Arrested Crack in the Bottom Flange

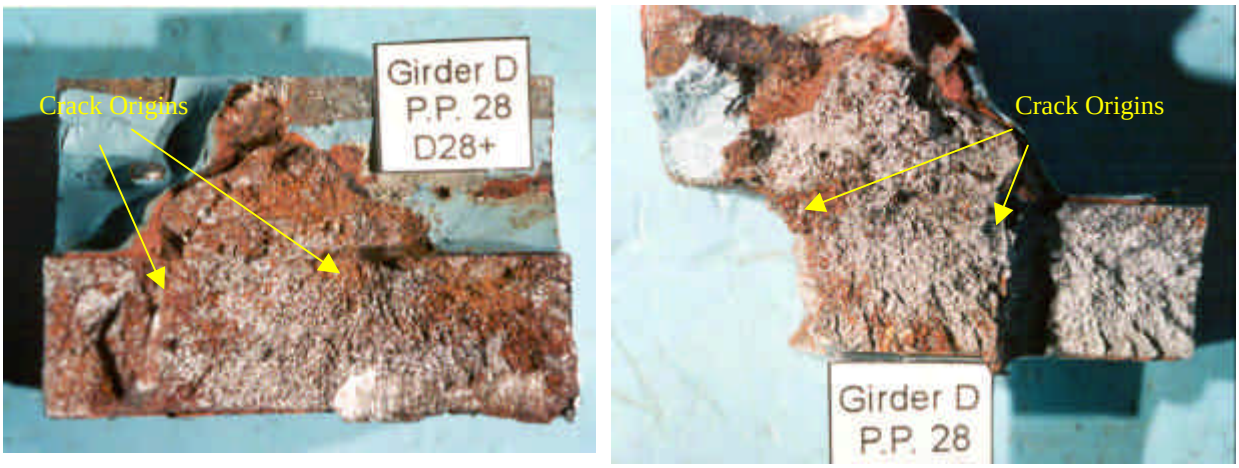

Figure 53: Opposing Crack Surfaces at the Shelf Plate Weld Termination Fracture Origin

Figure 54 shows low magnification SEM micrographs of the two origin areas and higher magnification micrographs revealing the mechanism of fracture in these areas. The weld toe fracture origin showed evidence of cleavage fracture at all areas near the origin from the web surface inward. The fracture mechanism at the weld root fracture origin was not as clear since corrosion product and corrosion damage to the underlying crack surface in this area was more severe. Evidence of cleavage fracture was observed at all areas which could be examined and no evidence of stable crack growth was observed, as was also found at the fracture origin in Girder E. The fractures did not provide any clear indication of the sequence of fracture, however, it is likely that the two cleavage instabilities occurred at a very short time interval.

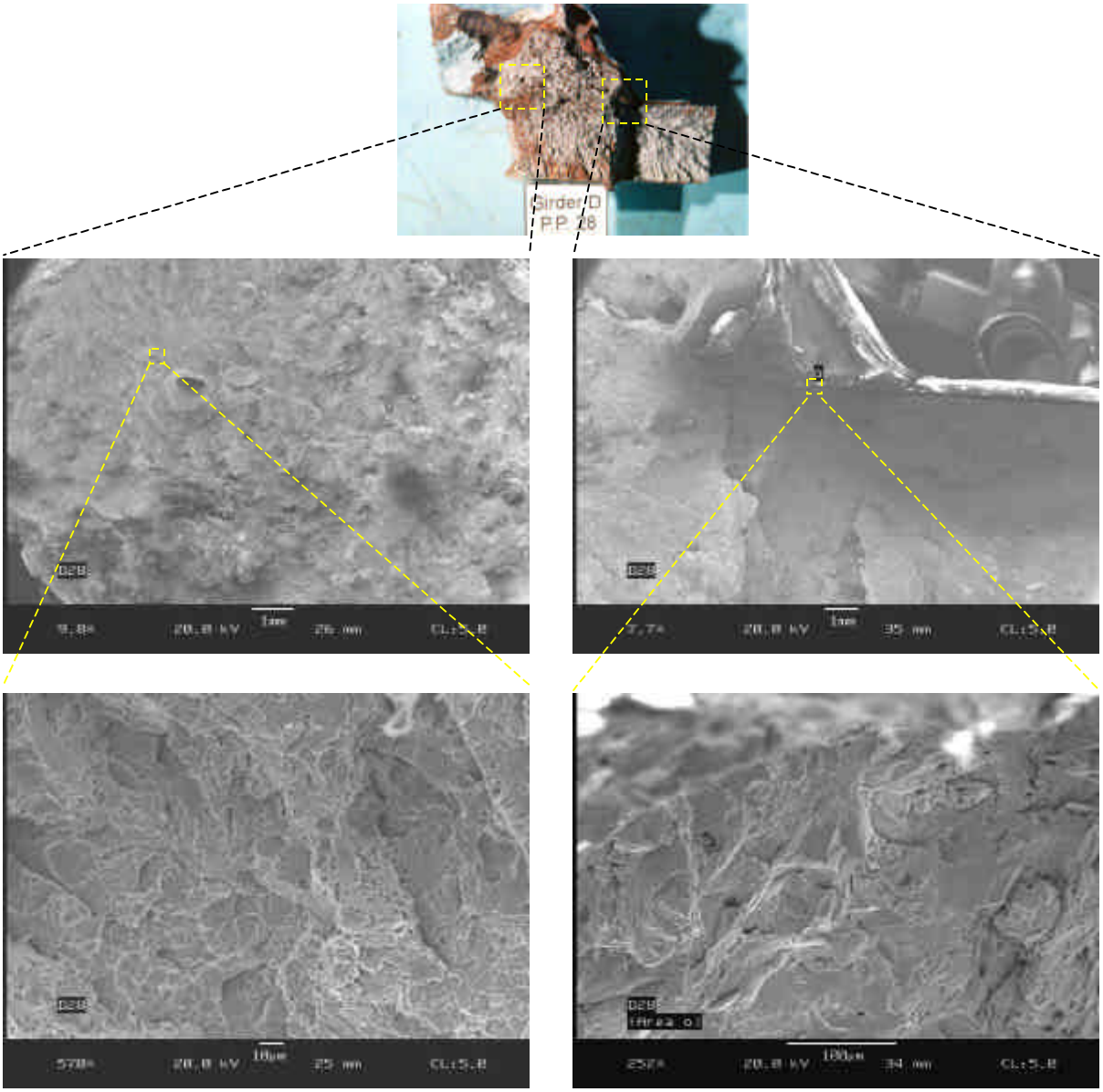

Figure 54: SEM Micrographs of the Fracture Origin Areas Showing Cleavage Fracture (Girder D P.P. 28)

4.2.3 Girder F P.P. 28 - Fracture Origin

The fracture origin in Girder F also traced back to the same location as in Girders D and E. The bottom flange and web section containing the lateral bracing connection detail fracture origin is shown in Figure 55. A view of the fracture surface in the origin area is shown in Figure 56. Again, cleavage chevron patterns indicated a fracture origin at the shelf plate weld termination in the vicinity of the web surface. Corrosion product again obscured a portion of the crack surface in this area, however, cleavage fracture was observed where the underlying crack surface could be viewed (see Figure 56). No indication of a material defect or stable crack growth was found in this area.

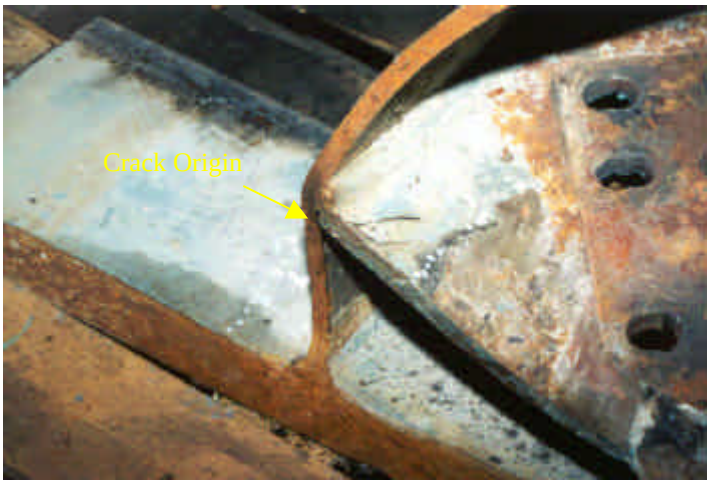

Figure 55: Section of Girder F P.P. 28 Containing the Shelf Plate Weld Fracture Origin

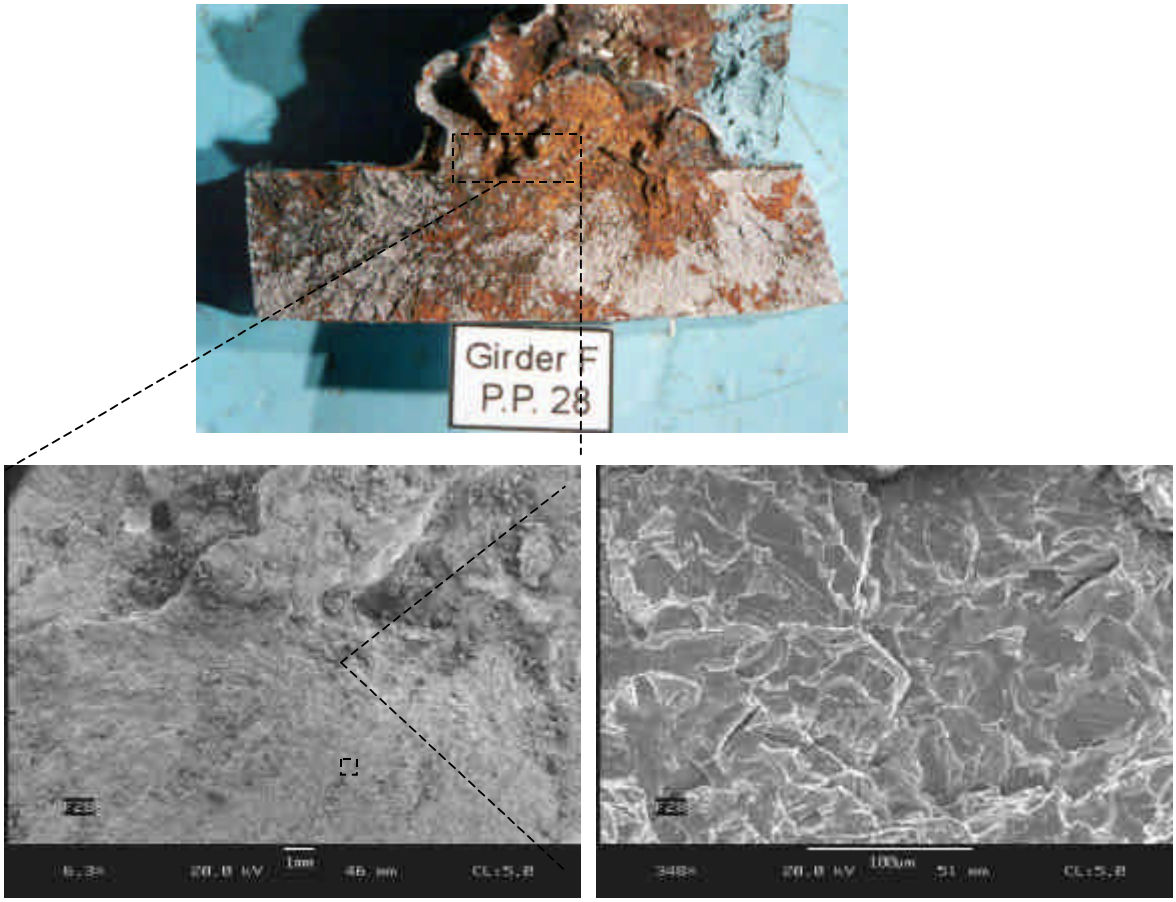

Figure 56: SEM Micrographs of the Fracture Origin Area Showing Cleavage Fracture (Girder F P.P. 28)

4.2.4 Girder D P.P. 9 and Girder B P.P. 26 - Fracture Origin

Two additional web cracks detected at other lateral bracing connections in other spans of the structure were removed and examined fractographically. Figure 57 shows the section of web and shelf plate removed from Girder D at P.P. 9 and the fracture surface at the termination of the shelf plate weld. Cleavage fracture initiation originating in the web in the vicinity of the weld root is clearly indicated by converging chevron marks. Viewed at higher magnification (see Figure 58) the origin area showed no macroscopic defect in this area and only cleavage fracture similar to the crack origins in Girders D, E, and F at the failed span.

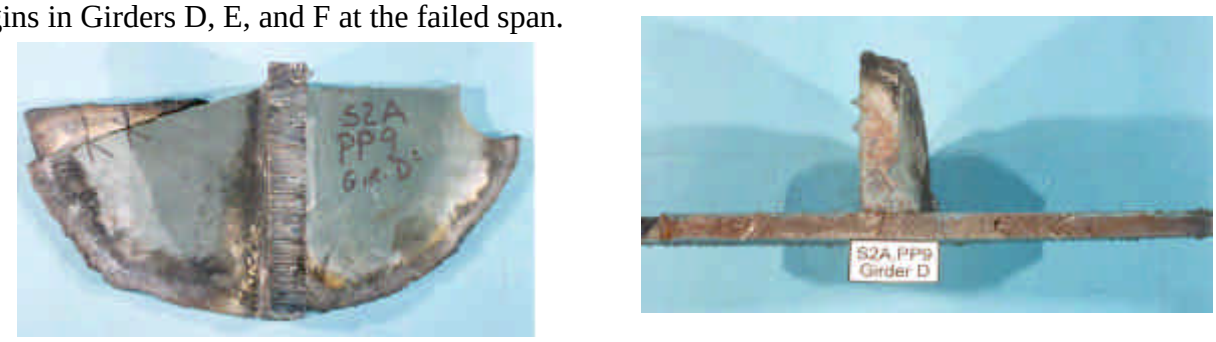

Figure 57: Web Crack Removed From Girder D at P.P. 9 at the Shelf Plate Connection

Another web crack at a lateral bracing connection found in Girder B of the adjacent span a P.P. 26 was also removed for examination (see Figure 59). The crack origin again appeared to be located at the shelf plate weld termination, however, in this case an unusual blackened thumbnail feature was seen penetrating the web surface adjacent to the weld from which cleavage fracture clearly initiated. The size and appearance of the thumbnail is enhanced in the photograph shown in Figure 60 after cleaning the crack surface. The blackened thumbnail extended into the web to a maximum depth of about 3/16" and remained fully covered with an oxide layer despite cleaning attempts. The oxide layer appeared slag-like , however, it was unusually adherent for weld slag. It would also be unusual for weld slag to be able to penetrate to this depth in the web plate. Viewed at higher magnifications (see Figure 54) the oxide covering the surface of the thumbnail area completely obscured the underlying fracture surface. At the boundary of the thumbnail some indications of mixed mode fracture (cleavage and ductile fracture) was observed. Beyond this area the fracture was entirely cleavage in appearance.

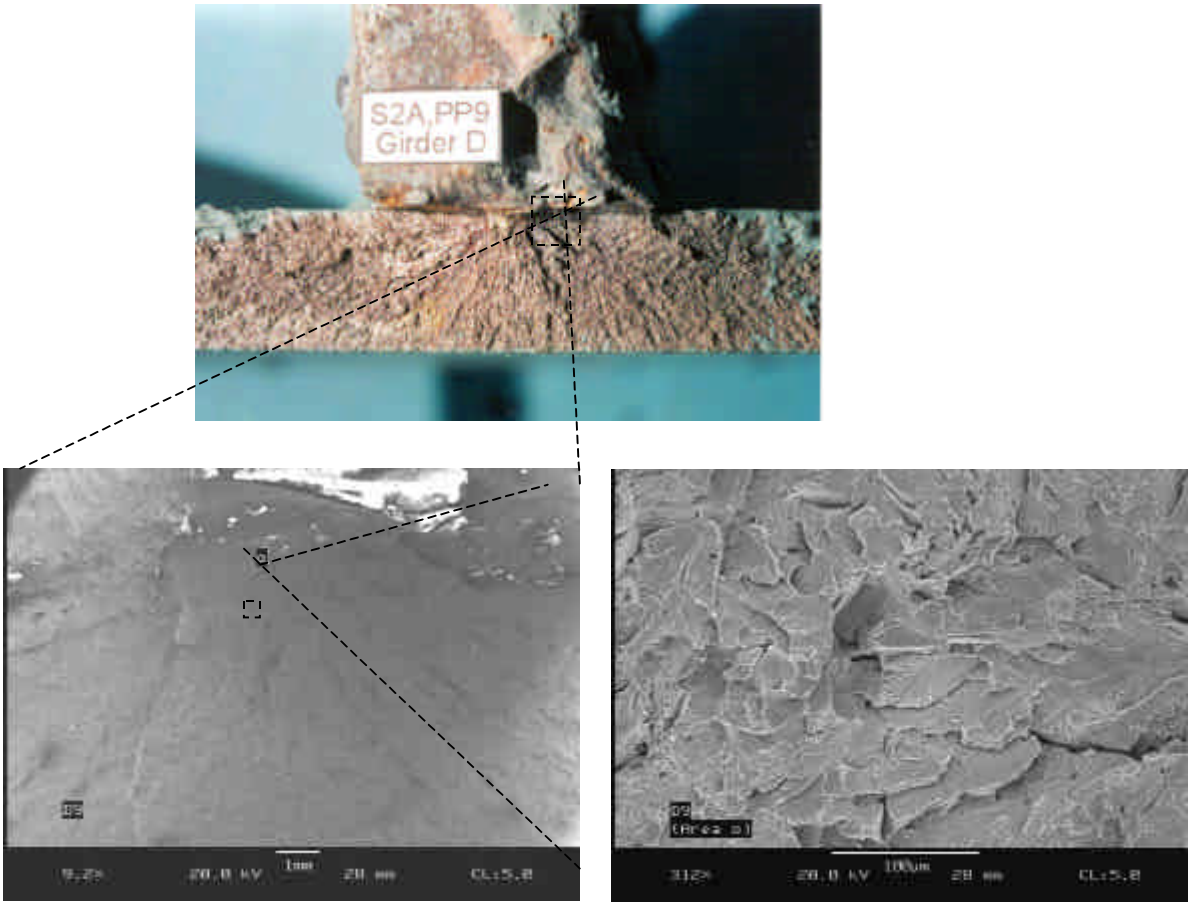

Figure 58: Fracture Origin in the Web Showing Cleavage Fracture (Girder D P.P. 9)

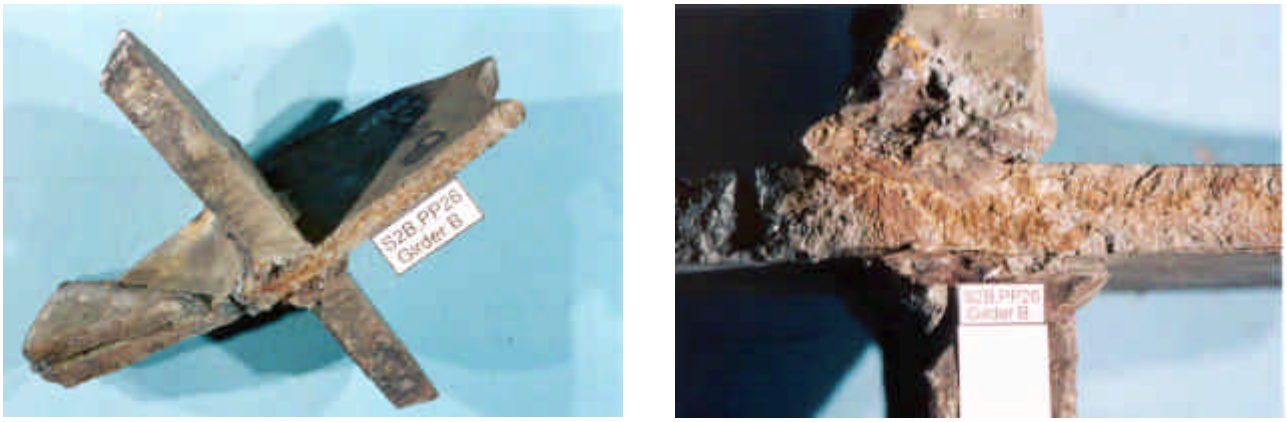

Figure 59: Web Crack Removed From Girder B at P.P. 26 at the Shelf Plate Connection

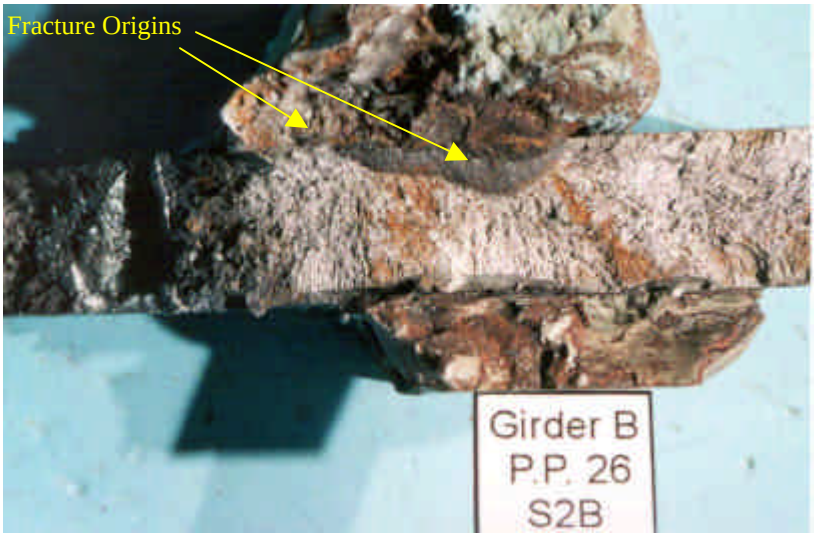

Figure 60: Fracture Origin Showing Blackened Thumbnail and Cleavage Initiation Areas (Girder B P.P. 26)

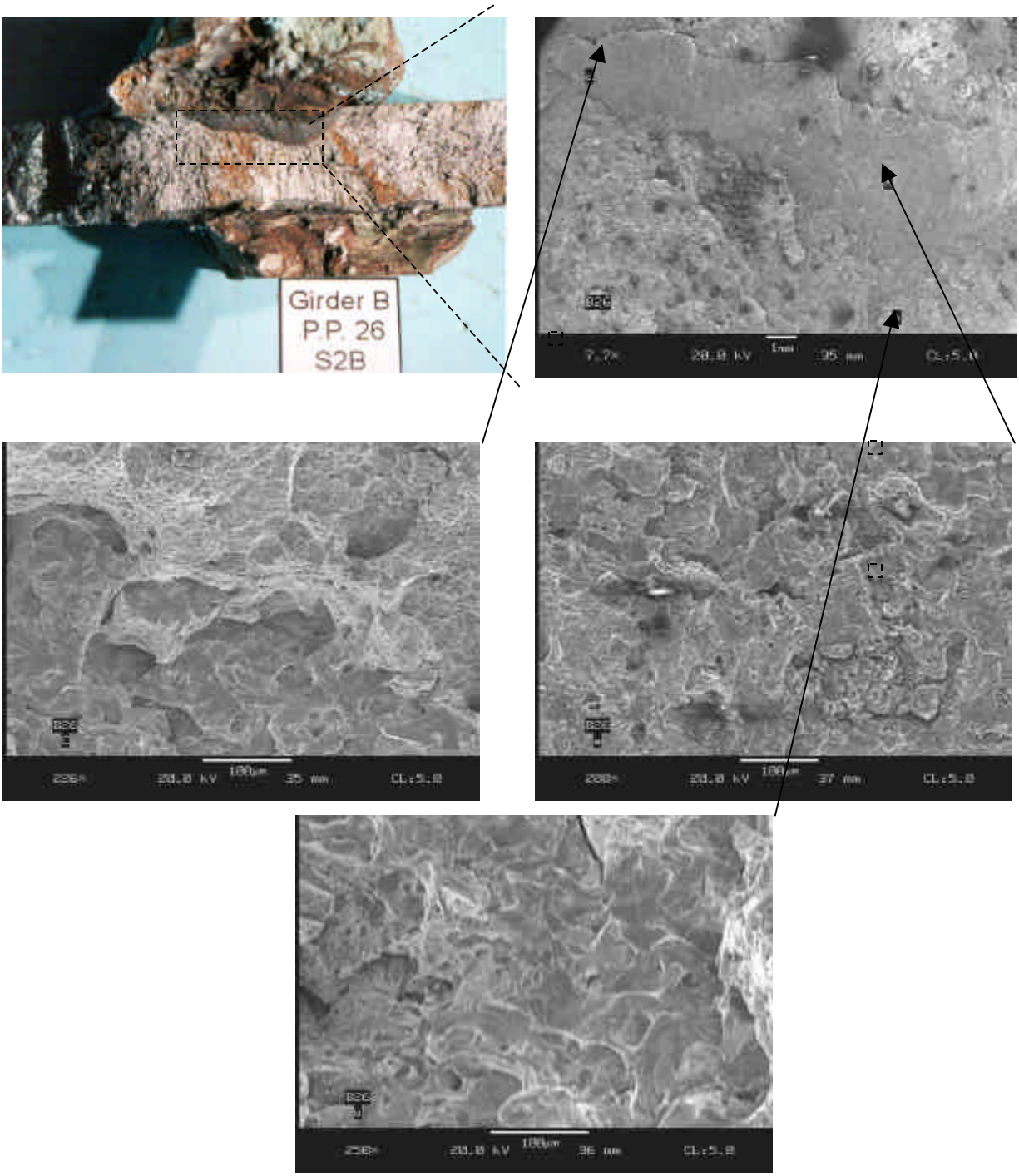

Figure 61: SEM Micrographs Showing the Oxide Layer Covering the Thumbnail Defect and Cleavage and Mixed Mode Fracture Near the Fracture Origin. (Girder B P.P.26)

To try to gain additional information about the origin of the thumbnail area the crack surface was cross-sectioned through the thumbnail and prepared metallographically. The resulting etched cross-section is shown in Figure 62 where the shelf plate, shelf plate weld, web plate, and a portion of the opposing shelf plate weld is seen. Weld slag is evident at the shelf plate weld termination, however, no slag layer was observed at the thumbnail area. Closer examination of the thumbnail area showed no evidence of weld metal or heat-affected base metal at the thumbnail thus discounting a weld metal or HAZ defect origin. The origin of the thumbnail may be associated with a fabrication crack which propagated into the web plate and arrested or with fatigue crack growth over an extended time period thus producing the heavily oxidized surface. A combination of the two may be the most likely source of the defect.

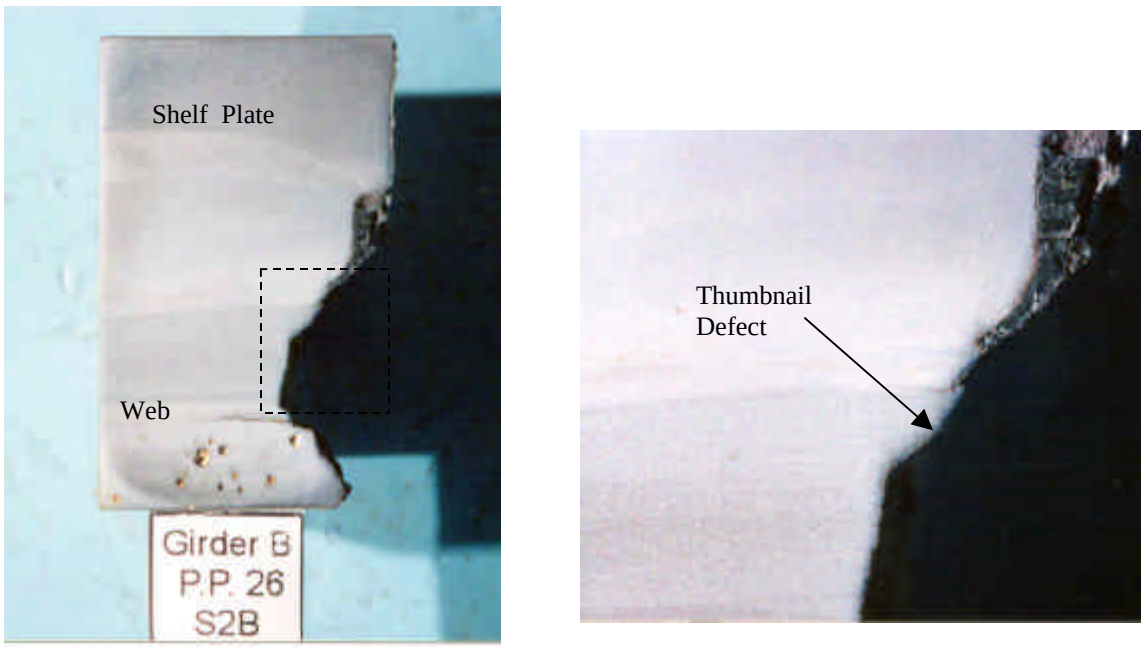

Figure 62: Etched Cross-Section Through Thumbnail Defect at Fracture Origin (Girder B P.P. 26)

4.2.5 Girder D P.P. 28 - Bottom Flange Crack Arrest

The crack arrest in the bottom flange region of Girder D was examined to determine the location where the crack arrested (i.e. web-flange fillet weld or flange plate) and also to characterize the change in fracture mechanism during crack arrest microscopically. To identify the arrest location the bottom flange of the girder in the area where the web crack terminated was saw-cut close to the web-flange fillet weld and fractured in bending at liquid nitrogen temperature. The exposed crack surface is shown in Figure 63 where the original crack is delineated by surface oxidation. The web crack clearly propagated through both web-flange fillet welds (except for a small ligament near both weld toes) and arrested just beyond the weld fusion line of each weld (¼ in. below the flange surface). The position of the arrested crack tip coincides with the heat-affected zone of the weld and likely arrested in the fine grained heat-affected-zone since this region generally has highest toughness within the HAZ and often higher than the unaffected base metal.

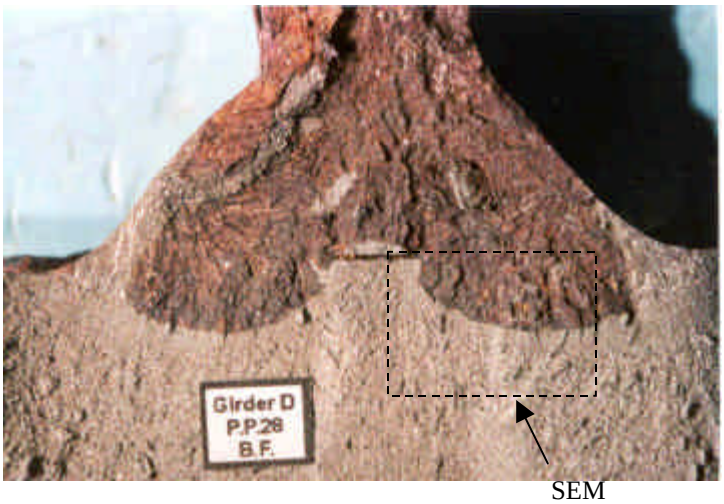

Figure 63: Exposed Fracture Surface From Girder D P.P. 28 Showing Crack Arrest in the Bottom Flange. Note the Weld Fusion Line Location

The crack surface was examined microscopically in the crack arrest region to detect changes in fracture mechanism during arrest. Figure 64 shows SEM micrographs at locations along the crack arrest boundary. The Afresh@ cleavage fracture developed at cryogenic temperatures to expose the crack surface is readily distinguishable from the oxidized original fracture. Interestingly, little change in fracture mechanism was detected along the crack arrest boundary. Some evidence of mixed mode fracture was observed at some locations, however, other locations showed all cleavage fracture up to the crack arrest boundary.

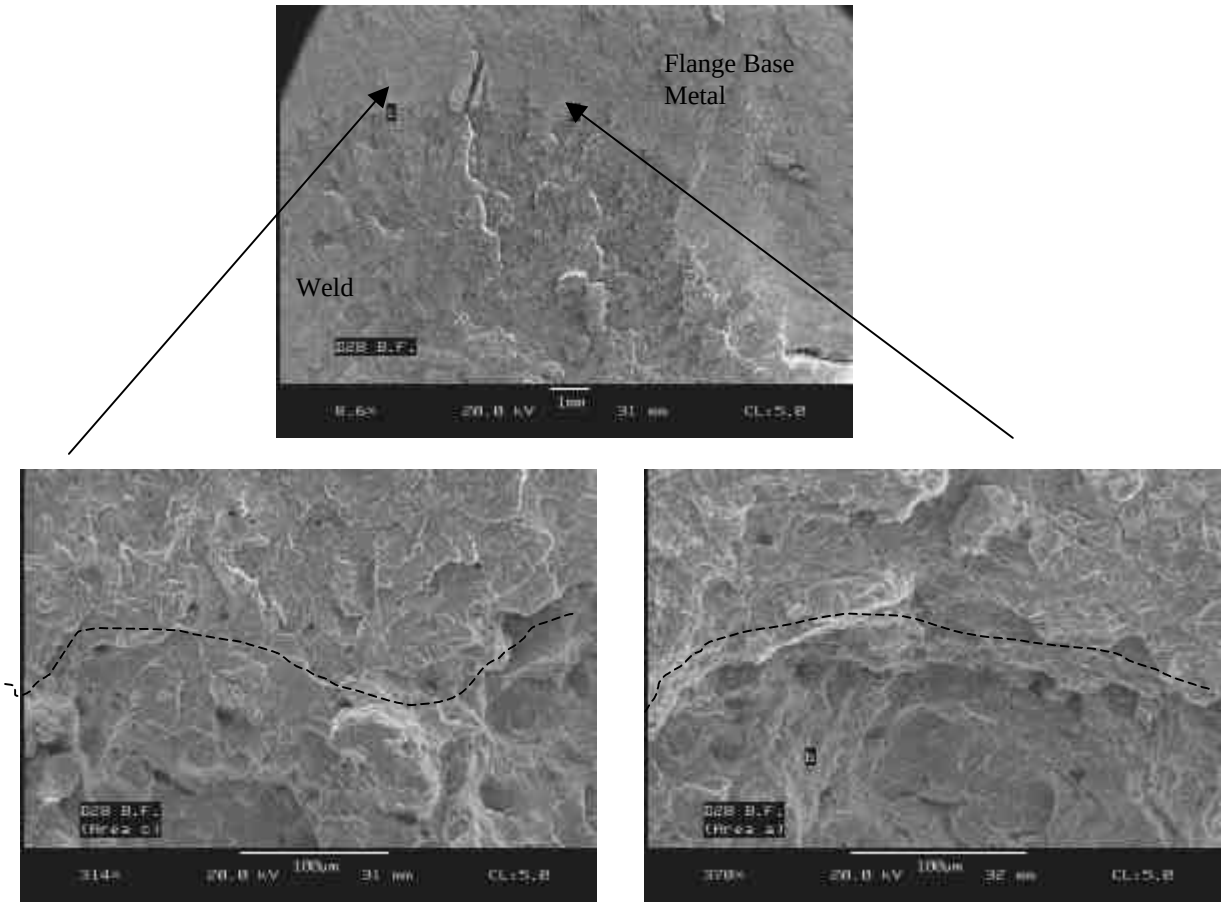

Figure 64: SEM Micrographs of the Crack Arrest Boundary Showing Cleavage and Ductile Fracture. Dashed Line Denotes Crack Arrest Boundary. (Girder D P.P.28)

4.2.6 Girder E P.P. 28 - Bottom Flange Fracture

The web-flange weld area of the bottom flange of Girder E ,where no crack arrest occurred , was also examined for any indication of fracture mechanism change. Figure 65 shows the crack surface in the web-flange area. Considerable corrosion attack of the crack surface had occurred prior to examining which cleaning only partially removed. No visual indication of a change in fracture mechanism was observed on the crack surface. Where observable with the SEM the traverse of the crack surface from the web through the web-flange fillet weld and flange plate showed only cleavage fracture.

Figure 65: Cleavage Fracture in the Web-Flange Area of the Bottom Flange of Girder E P.P. 28

4.2.7 Girder E P.P. 28 - Web Fracture Bifurcation

The web crack bifurcation observed several inches above the fracture origin area of Girder E P.P. 28 was also examined in detail for a possible metallurgical cause for the crack branching observed. Figure 66 shows the crack bifurcation area near the crack origin. Fractographic examination of the crack surface did not reveal a material defect in this location. A metallographic cross-section through the web, shown in Figure 67, also did not show any indication of a material defect below the crack surface or evidence of a possible weld repair at the point of crack bifurcation.

Figure 66: Crack Bifurcation in the Web of Girder E P.P. 28 Near the Fracture Origin.

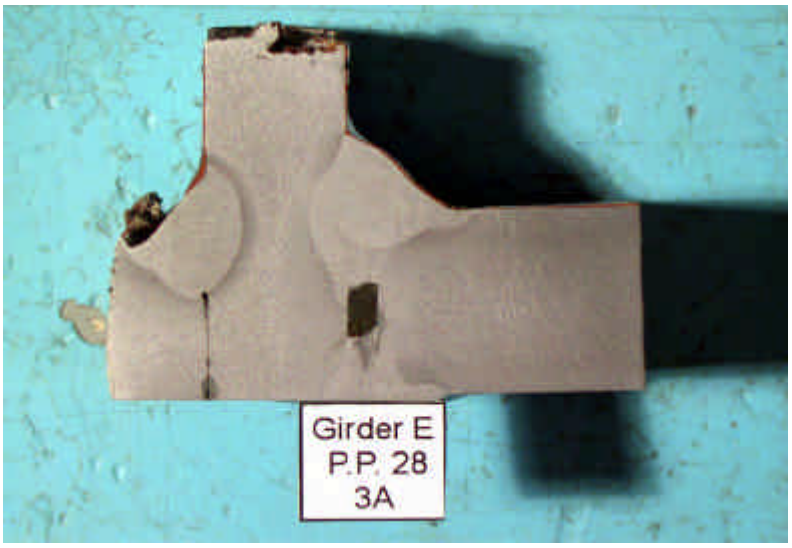

Figure 67: Etched Cross-section Through the Web and the Crack Bifurcation Location.

4.2.8 Girder E P.P. 28 - Shelf Plate Fracture at Hole Repair

The shelf plate from Girder E P.P. 28 is shown in Figure 68 with the hole removed at the corner of the plate next to the girder web and vertical connection plate. Since a smooth area previously observed on the fracture surface adjacent to the hole had a fatigue-like appearance (see Figure 68) this area was examined in detail to determine whether fatigue cracking had developed in the hole area prior to the girder failure. Visual examination of the crack surface after ultrasonic cleaning showed that a large part of the smooth area was due to abrasion presumably introduced during demolition. Fatigue striation indications, however, were observed at the edge of the plate on the inside face of the hole (see Figure 69). Further from the plate edge elongated dimple fracture, associated with ductile shear fracture, was observed which likely developed during failure of the girder. Due to abrasion and corrosion damage to the surface the size of the fatigue crack prior to fracture could not be estimated.

Figure 68: Girder E P.P. 28 Shelf Plate Showing the Hole Repair and Crack Surface Adjacent to the Hole

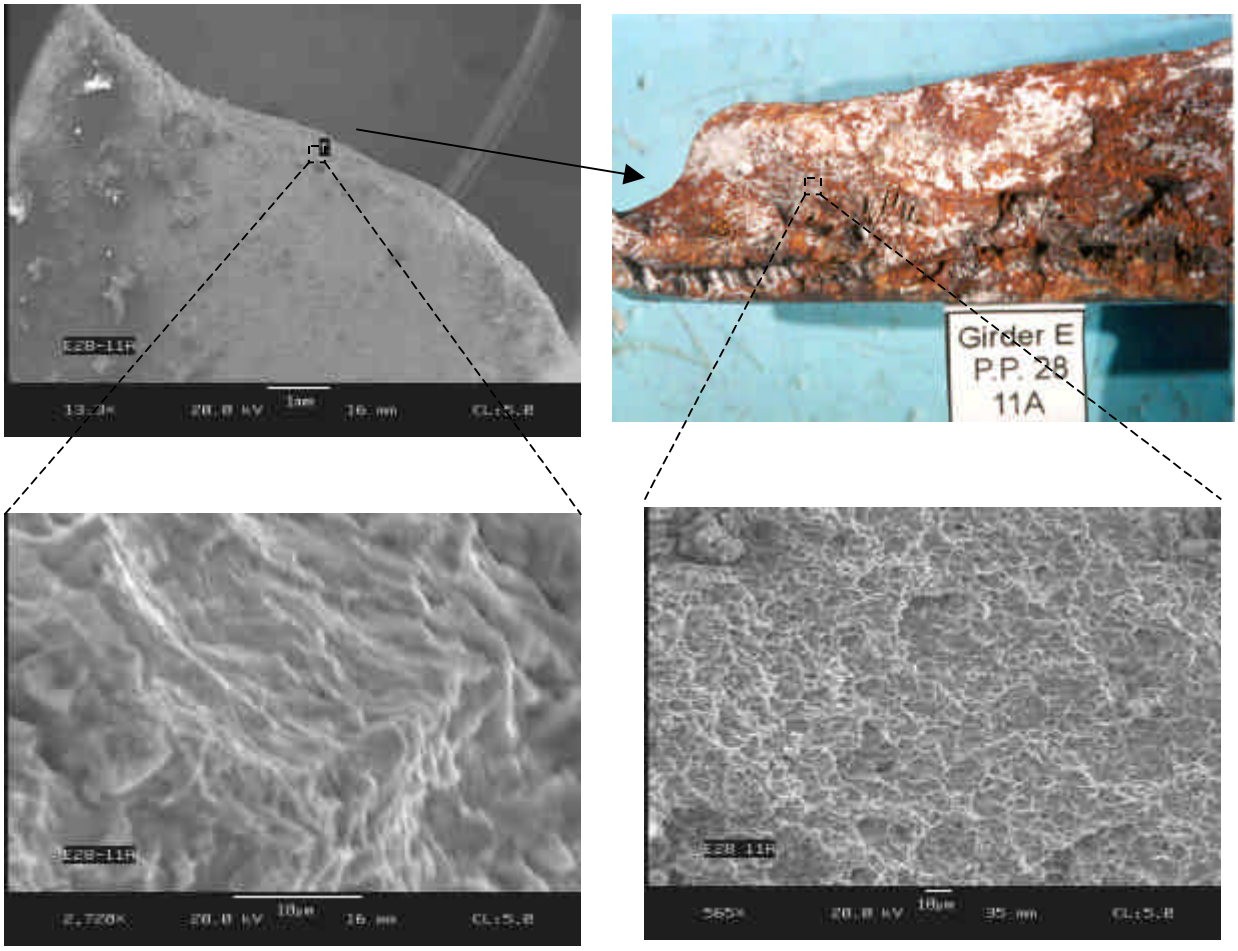

Figure 69: SEM Micrographs Obtained Near the Shelf Plate Hole Showing Fatigue Striations Near the Hole Edge and Ductile Shear Fracture Beyond (Girder E P.P. 28)

4.2.9 Girder E P.P. 28 - Transverse Brace Fracture

The fracture origin area of the brittle fracture which developed in the WT12X 55 transverse brace in the coped area was examined for ductile fracture prior to cleavage initiation. Chevron markings indicated that the brittle fracture initiated within the radius of the flame cut cope at the corner of the flange (see Figure 70). Microscopic examination of the corner region showed only cleavage fracture to within 1 mm of the corner. It was not possible to observe the crack surface closer to the corner due to abrasion of the surface, however, it would appear that little or no ductile fracture had preceded cleavage initiation.

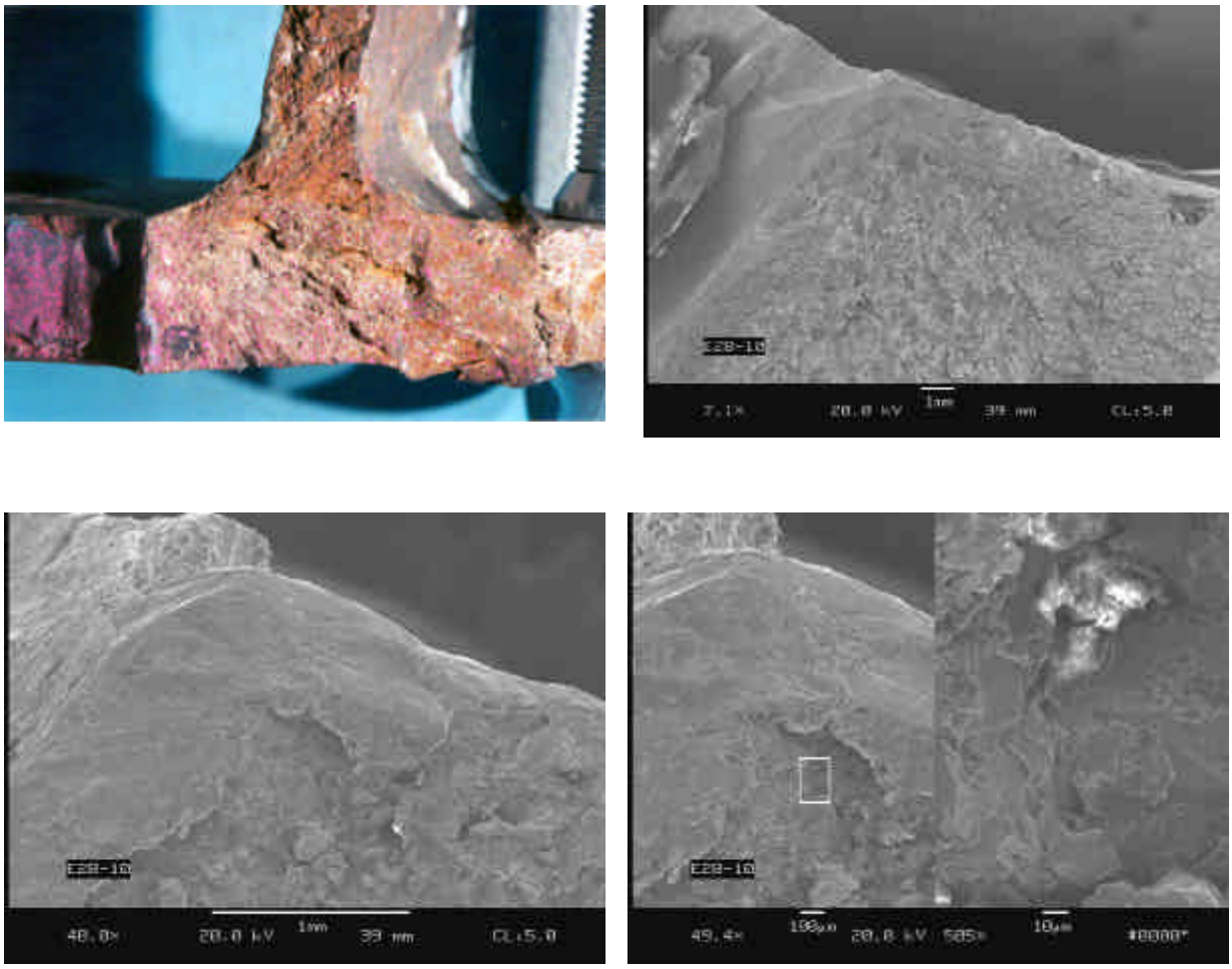

Figure 70: Transverse Brace Fracture at Girder E P.P. 28. Cleavage Fracture Initiated in the Radius of the Flame Cut Cope at the Corner Cleavage was Observed Next to the Abraded Crack Surface at the Corner

4.3 SUMMARY, FRACTOGRAPHIC AND METALLOGRAPHIC EXAMINATION

1. Fractographic examination of the fracture origin of Girder E at P.P. 28, located at the termination of the shelf plate weld adjacent to the vertical connection plate, indicated that the fracture initiated by cleavage in the girder web near the weld root. No evidence of a material or fabrication defect was found at the fracture origin. Without the presence of a macroscopic defect at the origin cleavage likely initiated from a microscopic discontinuity which may have sharpened by fatigue over time. Cleavage fracture initiation from a microscopic defect is consistent with the high triaxial stress state believed to exist in this area.

2. Examination of the fracture origins of the adjacent Girders D and F at P.P. 28, also located at the termination of the shelf plate weld adjacent to the vertical connection plate, showed similar conditions at the fracture origin as observed in Girder E. No evidence of a material or fabrication defect was found at either fracture origin. As for Girder E fracture initiation appeared to occur by a cleavage mechanism without evidence of stable crack growth by fatigue or ductile tearing preceding the fracture instability.

3. Examination of girder web fractures originating at the shelf plate weld termination which were detected in other spans of the structure (Girder D at P.P. 9 and Girder B at P.P. 26) also showed the same absence of a macroscopic defect and/or stable crack growth at the fracture origin in one case (Girder D at P.P. 9). A defect condition of undetermined origin was observed in the fracture origin area of Girder B at P.P. 26.

4. The fracture in the web of Girder D at P.P. 28 was found to have arrested in the flange plate close to the heat-affected-zone of the web-flange fillet welds. The crack penetrated the flange to a depth of approximately ¼ in. when it arrested. Little evidence of change in fracture mechanism was observed at the crack tip along the crack arrest boundary.

5. Evidence of fatigue crack propagation was detected near the hole introduced in the shelf plate of Girder E at P.P. 28. The size of the fatigue crack when failure of the girder occurred is not known due to damage of the crack surface in this area. Fractographic evidence suggests that it was less than ⅛in. in length .

5. FRACTURE ANALYSIS

The fractographic studies have demonstrated that crack instability developed in all lateral gusset connections examined as cleavage fracture that extended from the web plate surface. The intersection of the transverse connection plate fillet welds and the longitudinal shelf plate partial penetration weld created a crack-like condition. In most of the joints, the slotted shelf plate had been pushed against the transverse connection plate at the time of fabrication, as illustrated in Fig. 71. As the ½ in. beveled joint in the ¾ in. thick shelf plate was welded to the girder web, a condition of high triaxiality was formed. With the tight fit of the shelf plate against the transverse stiffener, the intersecting welds created a crack-like condition in the small gap.

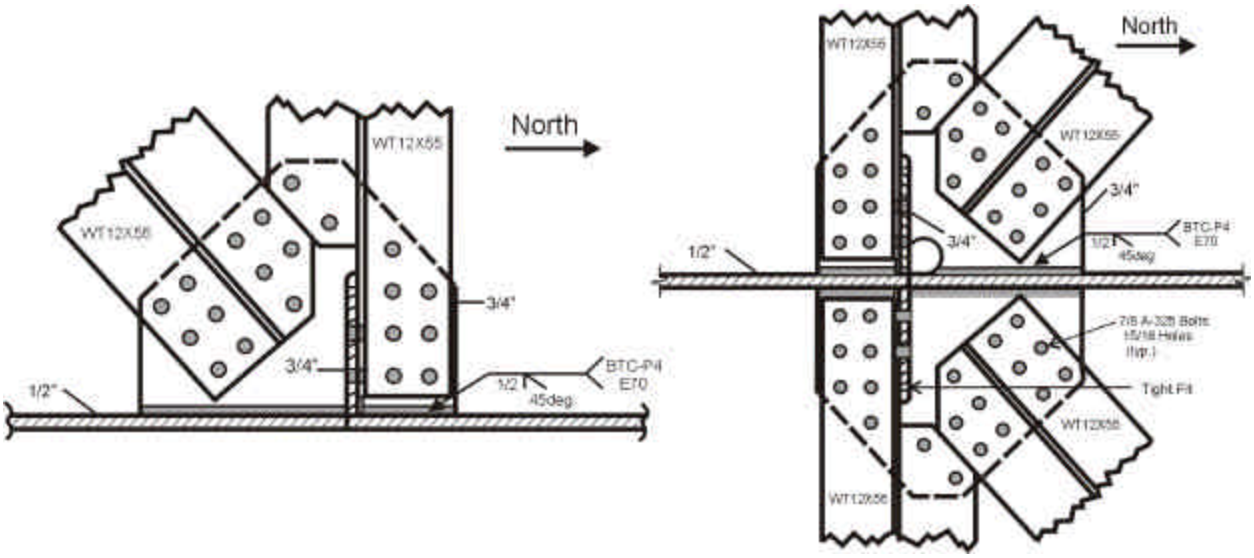

(a) Outside Girders (b) Interior Girder

Figure 71: Geometric Condition Providing a Crack-Like Plane When Shelf Plate is Touching Transverse Connection Plate

During service, the cyclic stress in the small gap served to sharpen the crack tip which was at or near to the web plate. No evidence of fatigue crack growth was observed at any of the five joints that were examined. In cases where there was entrapped slag or cold laps between the two welds any crack extension evidence was destroyed by corrosion or was sharpened at such low levels of crack growth that striations were not detectable. All that was observed in the fractographs seen in Figures 51 to 61 were cleavage facets.

5.1 PREDICTIONN OF WEB CRACK INITIATION

The finite element 3D model suggests that the stress field in the shelf plate is mainly compatible with the web for an effective width of 3 to 4 inches. T o account for the three-dimensional nature of the stressed crack-like shelf plate connection, an effective crack width of 3 inches was assumed. Experience with fatigue crack extension has demonstrated that the crack extends into the web plate as an elliptical surface crack (9,10). A suitable 3D model that

accounts for the geometric condition of the crack-like plane and its extension into the web plate is a penny-shaped crack, as shown in Fig. 72.

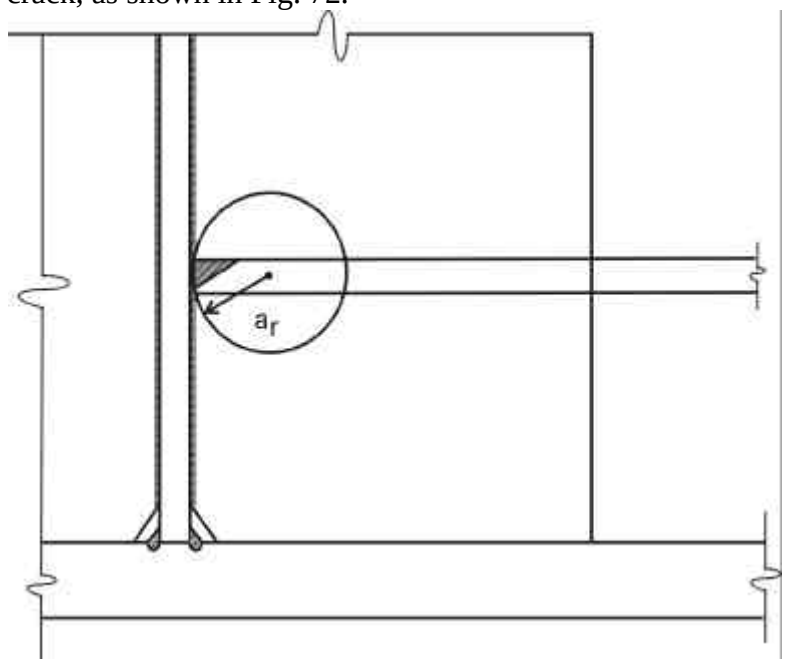

Figure 72: Idealized Circular 3D Crack Model at Shelf Plate - Transverse Connection Plate Intersection

The stress intensity factor for this case is defined as:

$$K = \frac{2}{p} s \sqrt{p a_r} \sqrt{\sec \frac{p a_r}{2t}} \tag{1}$$

where a_r = radius of the circular shaped crack and $2t = 2a_r + 2t_{2w}$. Hence, using the effective crack width $2a_r$ = 3 in. and t_w = ½ in. the web thickness, results in 2t = 4 in. With the crack tip at the web plate surface, K becomes

$$\begin{aligned} K &= \frac{2}{p} s \sqrt{p\,(1.5)} \sqrt{\sec \frac{1.5\,p}{4}} \\ &= 2.23\, s \end{aligned} \tag{2}$$

The finite element study has demonstrated that the triaxiality factor at the web gap was about 1.36 (see Section 3.2.4). Hence, the highest probable stress at the crack tip is $\sigma = 1.36\ \sigma_y$ where σ_y is the nominal yield point of the web plate or 42 ksi. This yields an estimated maximum stress intensity factor of

$$K_{\max} = 2.23\,(1.36\ x\ 42) \sim 127\ ksi\ \sqrt{in.} > K_{Ic} \sim 120\, ksi\ \sqrt{in.} \tag{3}$$

This maximum stress intensity exceeds the K_{Ic} estimated fracture resistance for bridge loading rates which is seen to be about 120 ksi $\sqrt{in.}$ for all three-web plates at PP 28 (Figs. 11 to 13). This demonstrates that the shelf plate detail under worst-case conditions of crack-like conditions will result in crack instability with no appreciable fatigue crack sharpening. When the shelf plate is not tightly fitted to the connection plate, the geometric condition is not as acute. The larger the gap, the less critical the detail becomes. Other factors such as the overlapping intersecting welds can be variable. In some cases there is trapped slag, as observed in Figures 61 and 62 for the sample removed from PP 26, Girder B.

The shelf plate at Girder E had a 2 in. hole installed on the west side of the girder web in 1993. The 3D finite element model demonstrated that this increased the web gap stress on the east side of the web by about 10%. Hence, at PP 28, center Girder E would logically be subjected to the highest web gap stress and be most vulnerable to crack instability.

5.2 CRACK ARREST AT BOTTOM FLANGE

Once initiated, the crack extended in the web dynamically and entered into the bottom flange through the two longitudinal fillet welds that connected the web to the flange plate. However, the crack shape changes as it extends into the flange through the submerged arc welds. These welds have a higher toughness than the web or flange plates. One possible model is to consider the crack as another penny-shaped crack, with a radius that is in the web near the toe of the web-flange weld, as shown in Figure 73.

Fatigue cracks that have developed in the web plate at stiffeners or gusset plates have been observed to propagate into the flange plate like a circular-shaped crack with its origin in the web near the flange (9,10,11). The crack front seen in Fig. 63 for Girder D confirms this characteristic shape at crack arrest. The effective radius, a_{rf}, is about 0.75 in. for the arrested crack.

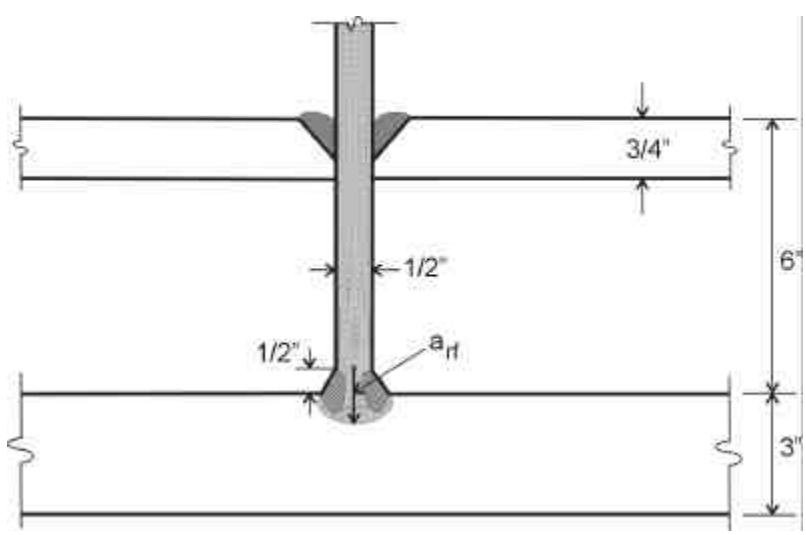

Figure 73: Idealized Circular 3D Crack Arrested in Web-Flange Weld Zone

Hence,

$$K = \frac{2}{p} s \sqrt{p\, a_{rf}} \tag{5}$$

where a_{rf} ~ 0.75 in. or

$$K = 0.98\, s \tag{6}$$

The stress in the welds is also at the flange yield point from the longitudinal weld shrinkage. However, no triaxiality exists. This results in an estimated maximum stress intensity of 51 ksi $\sqrt{in.}$ for Girder E with a yield point of 52.2 ksi with K_{Id} = 25 ksi $\sqrt{in.}$, the fracture toughness of Girder E was unable to arrest the crack after it propagated through the weld metal and fractured the flange. This also occurred at Girder F where its dynamic fracture toughness K_{Id} was also 60 ksi $\sqrt{in.}$ The higher yield point of 54.7 ksi for Girder F results in K_{max} = 53.6 ksi $\sqrt{in.}$ which is slightly below the dynamic fracture toughness and fracture resulted.

The crack in Girder D arrested in the fine grain heat affect zone, as was illustrated in Figures 63 and 64. The lower bound dynamic crack arrest capability of Girder D is about the same as Girder F, as seen in Section 2.2.4 Table 2.9. It was estimated to be 60 ksi $\sqrt{in.}$ at -10E F. Another difference between the two girders is the truckloads that were on the span when the fractures occurred. The truck(s) were likely in the east or center lanes which results in about 40% of the live load stress in West Girder D compared with the east Girder F and center Girder E during passage of the vehicles, as illustrated in Section 3.

The average yield point of the flange in Girder D was 50.3 ksi. Hence, the estimated K_{max} from Equation 6 is about 49.3 ksi $\sqrt{in.}$ which was less than the lower bound K_{Id} = 60 ksi $\sqrt{in.}$ for Girder D. The small differences in fracture toughness and yield point between Girders D and F were critical to the observed crack arrest in Girder D.

Once the crack in West Girder D arrested, its fracture resistance would return to the normal bridge loading rate fracture toughness of 120 ksi $\sqrt{in.}$ Hence, it was able to resist the redistributed dead loads from the cracked adjacent girders.

5.3 SUMMARY-FRACTURE ANALYSIS

1. The natural crack-like condition provided by the intersection of the shelf plate with the transverse floorbeam connection plate results from the intersecting welds, the small gap and the high triaxiality at the intersection.

2. The natural crack-like intersection sharpens with cyclic load, although no evidence of fatigue striations was detected at the fractured web details.

3. The web steel was found to have fracture toughness levels that are expected of the A36 steel plate. The bridge strain rate fracture toughness was between 120 ksi $\sqrt{in.}$ and 130 ksi $\sqrt{in.}$ at -10E F. for the three girders.

4. Center Girder E28 was subjected to higher web gap stresses as a result of the 2 in. retrofit hole drilled in the shelf plate in 1993. This was found to increase the stress on the opposite surface of the web by about 10%. This fact and the general observed behavior suggest that Girder E28 fractured first. The fracture models predicted the instability of the cross-section.

5. Fracture of the web plate at the shelf plate connection resulted in dynamic crack extension into the bottom flange plates. The center Girder E28 was found to have the least resistance to crack arrest. Its higher yield point and low dynamic fracture resistance K_{Id} of 25 ksi $\sqrt{in.}$ made it impossible to resist the web crack extension into the flange and was predicted by the fracture model.

6. The crack that initiated in the web of Girder F28 appears to have occurred at about the same time as Girder E28. The F28 flange plate had significantly higher dynamic fracture toughness (= 60 ksi $\sqrt{in.}$) than Girder E28 and could not arrest the web crack as it extended into the flange plate.

7. Only Girder D28 was found to possess dynamic fracture toughness capable of arresting the unstable web crack. This was in part due to its lower yield strength and characteristics of the truck loads crossing the structure.

8. In the absence of the high constraint and the severe stress conditions that were provided by the shelf plate, the web plates were found to possess sufficient fracture toughness to permit through thickness fatigue cracking without developing instability under normal conditions as assumed in the AASHTO Specifications.

6. SUMMARY AND CONCLUSIONS

1. All three girder web cracks at Panel Point 28 initiated from the crack-like geometric condition that resulted from the intersecting shelf plate and transverse connection plate welded connections with intersecting and overlapping welds.

2. The resulting geometric configuration caused extreme high levels of constraint and stress to develop in the web plate gap from the forces in the girders and the K-type lateral bracing members. This resulted in stresses in the girder web gap that were estimated to be at least 60% greater than the yield point of the web plate.

3. Brittle fractures (cleavage) were found to develop at every web crack examined without any detectable fatigue crack extension or ductile tearing at the crack origin.

4. The nature of the web crack development results in a detail that is not inspectable. The small critical crack size cannot be detected.

5. Once the web fractured, it was found that the bottom flange plates of Girders E-28 and F-28 were not capable of arresting the propagating crack. Only Girder D-28 was found capable of arresting the dynamic crack at -10E F.

6. All of the flange and web steels were found to have mechanical tensile properties and Charpy V-Notch toughness that satisfied the AASHTO requirements at the time the structure was built. The Charpy V-Notch toughness was also found to satisfy current (2001) requirements for Zone II.

7. The web plates were found to have sufficient toughness to tolerate through plate thickness cracks under normal conditions without the high constraint conditions that were imposed on the girder web plate by the shelf plate welds and the intersecting transverse connection plate welds.

8. It is likely that web cracks which were detected in earlier inspections occurred at higher temperatures. This would enable the dynamic cracks to arrest at the flange-web connection. About the same level of fracture resistance existed for all of the web plates over a wide range of temperature.

9. Both the 2-1/4 in. and 3 in. flanges have sufficient toughness to tolerate through thickness cracks under normal bridge loading.

7. REFERENCES

1. Wright, W. J., Strock, T. and Hartmann, J.
   Hoan Bridge Forensic Investigation – Documentation of Condition Prior to Demolition, FHWA Research Report, March 2001.

2. Wright, W. J. and Tjiang, H.
   "Hoan Bridge Forensic Analysis – Material Property Tests,"
   FHWA Research Report, 2001 (in preparation).

3. Wright, W. J. and Xi, Z.
   "Hoan Bridge Forensic Analysis" -
   FHWA Research Report, 2001 (in preparation).

4. Miller, B. A.
   "Evaluation of Coupons from the Hoan Bridge,"
   Report to G.A.S. and Associates, Stork Technimet, Inc., Feb. 21, 2001.

5. AASHTO, "Standard Specifications for Transportation Materials and Methods of Sampling and Testing," Nineteenth Edition, 1998.

6. Barsom, J. M. and Rolfe, S. T.
   "Fracture and Fatigue Control in Structures," 3rd Edition,
   ASTM Stock Number: MNL41, ASTM
   West Conshohocken, PA, Nov. 1999.

7. Sivakumar, B. and Edberg, W.
   Hoan Bridge Failure Investigation: 3-D Modeling and Load Testing of Hoan Approach Unit S2A, Final Report
   Lichtenstein Consulting Engineers, May 17, 2001.

8. Nowak, A. S. Eom, J., Cho, T. and Laumet, P.
   Weight-in-Motion Truck Measurements on East Lincoln Avenue Viaduct, Milwaukee, WI, Report UMCEE 01-02,
   Department of Civil and Environmental Engineering, University of Michigan, April 2001.

9. Fisher, J. W., Pense, A. W., Hausammann, H. and Irwin, G. R.
   "Quinnipiac River Bridge Cracking," Journal of the Structural Division, ASCE, Vol. 106, No. ST4, April 1980.

10. Fisher, J. W., Albrecht, P. A., Yen, B. T., Klingerman, D. J. and McNamee, B. M.
    "Fatigue Strength of Steel Beams with Transverse Stiffeners and Attachments,"
    NCHRP Report 147, Transportation Research Board, 1974.

11. Fisher, J. W.
FATIGUE AND FRACTURE IN STEEL BRIDGES,
John Wiley and Sons, 1984.

12. Roberts, R., Irwin, G. R., Krishna, C. V., and Yen, B. T.
"Fracture Toughness of Bridge Steels – Phase II,"
Report, FHWA-RD-744-59, Federal Highway Administration, Washington, D.C.,
Sept. 1974.